NORTHWESTERN UNIVERSITY

Transport Measurements on (111) Oriented $(La_{0.3}Sr_{0.7})(Al_{0.65}Ta_{0.35})O_3/SrTiO_3$ Heterostructures

A DISSERTATION

SUBMITTED TO THE GRADUATE SCHOOL

IN PARTIAL FULFILLMENT OF THE REQUIREMENTS

for the degree

DOCTOR OF PHILOSOPHY

Field of Physics

By

Varada V Bal

EVANSTON, ILLINOIS

September 2018

ABSTRACT

Transport Measurements on (111) Oriented $(La_{0.3}Sr_{0.7})(Al_{0.65}Ta_{0.35})O_3/SrTiO_3$ Heterostructures

Varada V Bal

At the interface of two dissimilar entities, something novel can emerge. This idea has driven a vast amount of fruitful work on semiconductor interfaces, and given us the digital revolution. In the past decade, remarkable progress has been made in the synthesis and understanding of interfaces between oxides, opening up new avenues to explore fundamental emergent physics at the interface, as well as to provide viable candidates to augment or even surpass the performance of conventional semiconductor electronics. The two-dimensional conducting interface in the (001) $LaAlO_3/SrTiO_3$ system is the most studied example of oxide interfaces, showing a wide range of coexisting and competing phenomena such as superconductivity, superconductor-insulator transitions, magnetism, and spin-orbit interactions. The (111) oriented $LaAlO_3/SrTiO_3$ system has been recently found to have a few surprises of its own, with intriguing anisotropies in many transport properties along different in-plane crystal directions. This thesis presents the first results on a different $SrTiO_3$ based system: the conducting interface between $(La_{0.3}Sr_{0.7})(Al_{0.65}Ta_{0.35})$ and

(111) oriented $SrTiO_3$, which has a smaller strain as compared to the $LaAlO_3/SrTiO_3$ system. Electrical transport measurements at cryogenic temperatures reveal that no systematic anisotropy is seen in transport properties, unlike in the case of (111) oriented $LaAlO_3/SrTiO_3$. High-field magnetotransport shows the presence of high-mobility carriers at high electron densities, and exhibits multiband behavior, tunable *in situ* using an electrical back-gate, similar to the $LaAlO_3/SrTiO_3$ system. The data allow us to draw specific conclusions about band ordering in the system, and point to possible differences between the band ordering in (111) $(La_{0.3}Sr_{0.7})(Al_{0.65}Ta_{0.35})O_3/SrTiO_3$ and (001) as well as (111) oriented $LaAlO_3/SrTiO_3$. Low-field magnetotransport reveals that a strong spin-orbit interaction emerges in the regime of low electron density, when the high-mobility carriers are depleted from the system, a trend which is opposite to that observed in (001) oriented $LaAlO_3/SrTiO_3$. The most striking feature is that at millikelvin temperatures, in the regime of low electron densities, concomitant with the development of strong spin-orbit interaction, magnetic order emerges.

Acknowledgements

I would like to thank my advisor, Prof. Venkat Chandrasekhar for his invaluable support through my stint as a graduate student in his lab. His command over the subject, breadth of knowledge, and effectiveness as a communicator have been an inspiration during my journey as a physicist. His insistence on a deep understanding not just of the physics, but also of the details of the measurement systems from vacuum pumps to data acquisition programs has made me a more complete experimentalist. Under his guidance I have certainly "built a lot of character".

I would also like to thank my committee members, Prof. Ketterson and Prof. Koch, for always being ready to answer my questions, or help with a liquid nitrogen dewar or some other piece of equipment, and for their suggestions and feedback on my work. Pam, Bud, Agnes, Gretchen, Emily, and Vicki from the Admin and Accounting offices have helped me in navigating close to nine years of graduate school, and I am grateful for that.

Prof. Goutam Sheet and Prof. Jian Wei, earlier postdocs in the group, and Prof. Dmitrii Dikin, an earlier research professor in the group, introduced me to the ways of the lab early in my graduate career and Prof. Dikin taught me some tricks of machining and the value of being methodical in my work, and I'd like to thank them for that. I'd like to thank Dr. Ying Jia for her help with the equipment in NUFAB, and Steve Jacobson for ensuring a steady supply of liquid helium.

My time in the lab would have been infinitely more difficult if it were not for my fellow graduate students, Manan Mehta, Taewan Noh, Scott Mayle, Sumitabha Bhattacharya, Sam Davis, Aaveg Aggarwal, and Patrick Krantz. Sam and I spent the most time in lab together, and he was always there to help with experiments, discuss physics, and share the joys and sorrows of life in the lab. Manan and Taewan left the lab a bit earlier during my time there, but taught me a lot about the nittigritties of experimental work in a low-temperature lab, and also that I need a thicker skin to deal with people in life.

Manan has also been a wonderful husband, and I could not have done without his friendship and understanding during the two years of our two-body problem. I'd also like to thank Manan's parents, Toral and Mayank Mehta, for their love and support.

My parents, Meena and Vilas Bal, and my brother, Dr. Chinmaya Bal. You are my inspiration. Your positive attitude and your belief in me, when sometimes I lost it myself, gave me the strength to finish what I started. Thank you.

List of abbreviations

Term	Abbreviation
Transition metal oxide	TMO
$LaAlO_3$	LAO
$SrTiO_3$	STO
Two-dimensional conducting gas	2DCG
Spin-orbit interaction	SOI
$(La_{0.3}Sr_{0.7})(Al_{0.65}Ta_{0.35})O_3$	LSAT
Pulsed laser deposition	PLD
Atomic spin-orbit interaction	ASO
Rashba spin-orbit interaction	RSO
Density functional theory	DFT
Angle-resolved photo emission spectroscopy	ARPES
Electron-electron interactions	EEI
Shubnikov de Haas	SdH
Magnetoresistance	MR
Density of states	DOS

Term	Abbreviation
Superconducting quantum interference device	SQUID
Superconductivity	SC
Reflection high energy electron diffraction	RHEED
Atomic force microscopy	AFM
Deionized water	DI water
Isopropyl alcohol	IPA
Scanning electron microscope	SEM
Thermocouple gauge	TC gauge
Ultra high purity	UHP
Room temperature	RT
Residual resistance ratio	RRR
Power spectral density	PSD
Weak localization	WL
Weak antilocalization	WAL
Dzyaloshinskii-Moriya	DM

List of symbols

Quantity	Symbol
Temperature	T
Back gate voltage	V_g
Magnetic field perpendicular to sample	B
Magnetic field parallel to Hall bar	$B_{\|\|}$
Rashba Hamiltonian	H_R
Rashba coefficient	α
Dielectric constant	ϵ
Bare electron mass	m_e
Sheet carrier density	n
Carrier mobility	μ
Sheet resistance	R_s
Hall coefficient	R_H
Transport scattering time	τ
Effective mass	m^*
Conductivity	σ
Drude resistance	R_0
Fermi momentum	k_F
Mean free path	l
Diffusion constant	D
Fermi velocity	v_F
Contributions to resistance due to e-ph scattering	ΔR_{ph}

Quantity	Symbol
Contributions to resistance due to charged impurities	ΔR_{ion}
Activation temperature	T_A
Classical orbital contributions to resistance	ΔR_{cl}
Cyclotron frequency	ω_c
Amplitude of SdH oscillations	ΔR_{SdH}
Dingle temperature	T_D
SdH oscillation frequency	F
Spin degeneracy	N_s
Contributions to resistance due to magnetic scattering	ΔR_{mag}
Oxygen partial pressure during growth	P_{O_2}
Localization corrections to resistance	ΔR_{loc}
Phase coherence length, time, field	l_ϕ, τ_ϕ, B_ϕ
Spin-flip scattering time	τ_s
Spin-orbit scattering length, time, field	l_{so}, τ_{so}, B_{so}
Film thickness	d
Differential MR	$\delta R/R$
Contributions to resistance due to EEI	ΔR_{EEI}
Contributions to resistance due to exchange and singlet Hartree EEI	ΔR_{EEI}
Contributions to resistance due to superconducting fluctuations	ΔR_{SC}
Frequency of ac measurement current	ω
Transverse Hall resistance	R_{xy}
Differential background resistance	δR_{BG}

Table of Contents

List of Figures

CHAPTER 1

Introduction

The class of materials known as transition metal oxides (TMOs) has played a role in human history since ancient times: as beautiful pigments to decorate pottery and lodestones to make great explorations possible; to the present day where they find applications in fields at the cutting edge of technology, such as high-temperature superconductivity, electromagnetic memory materials, and catalysts for fuel cells.[**1**]

Behind the versatility and many of the fascinating properties of TMOs lies the fact that it is the correlated d-electrons of the transition metal ions that dictate their physics. These d-electron orbitals are anisotropic in nature, and consequently have a smaller overlap with the orbitals of neighboring atoms, thus leading to a smaller bandwidth, and making the effect of electron correlations relatively more important. In the presence of a crystal field the degeneracy of the d-orbitals is split, leading to a complex band structure.[**2**] Many of the transition metal ions can be multivalent, and may possess finite magnetic moments. Additionally, the crystal structure of TMOs can change, i.e., the various atomic bonds can bend and rotate to produce structural transitions depending on factors such as strain and temperature.[**3**] One can also easily dope TMOs with other cations or with oxygen vacancies without greatly undermining their crystal structure. All these factors give rise to a complex phase space with the possibility of a variety of broken symmetries.

Modern technology has allowed us to engineer heterostructures of TMOs with closely matched lattice constants. This epitaxial growth can create structures which host new

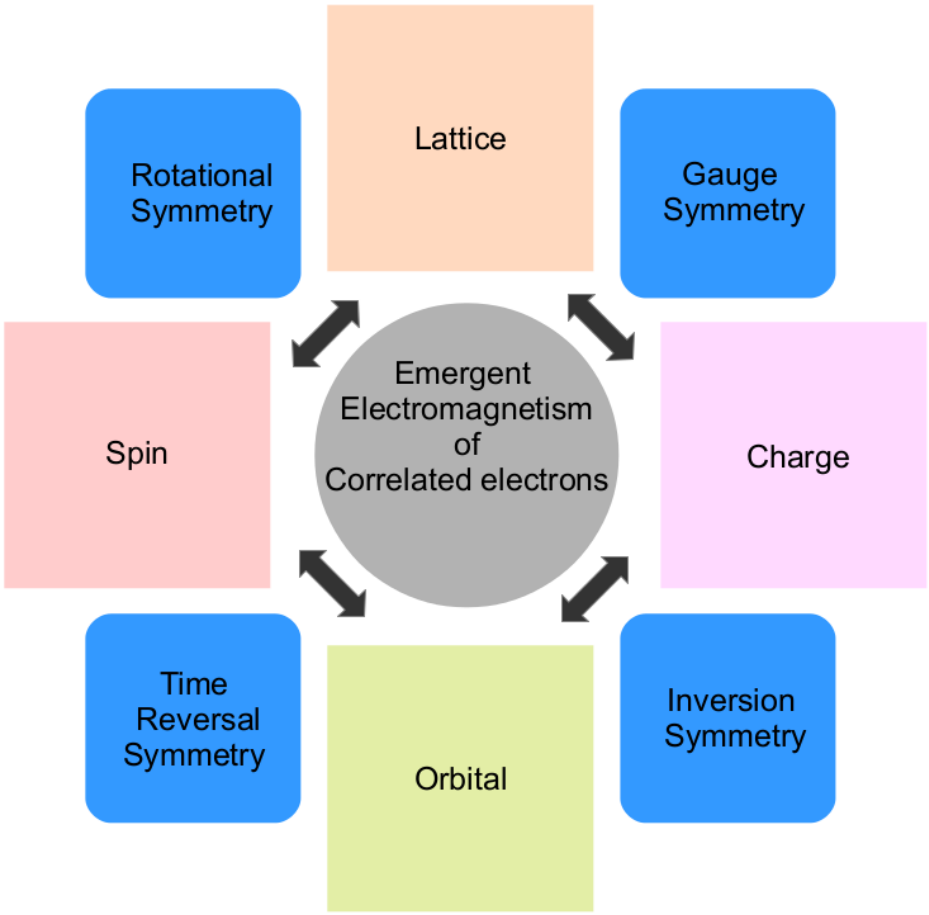

Figure 1.1. Schematic showing the interplay of various degrees of freedom in complex oxide heterostructures, along with the important broken symmetries observed in these systems.

functionalities and emergent phenomena not observed in the bulk materials. A paradigm of this direction of research is the layered perovskite material system $LaAlO_3/SrTiO_3$ (LAO/STO), in which a two dimensional carrier gas (2DCG) appears at the epitaxial interface between two insulating oxides, LAO and STO.[**4, 5**] The presence of the interface gives rise to a breaking of inversion symmetry, strain, and electronic or surface reconstructions due to the change in boundary conditions, directly affecting the band

structure of the material. A gate voltage applied to the STO substrate allows for the *in-situ* control of sample properties, since STO is an incipient ferroelectric with a very high dielectric constant.[**6, 7**] Thus we obtain a quasi-two dimensional correlated system of carriers which can host a myriad of coexisting and competing phenomena such as superconductivity,[**8, 9, 10**] magnetism,[**11, 12, 13, 14, 15, 16**] superconductor-insulator transitions,[**17**] strong spin-orbit interactions (SOI),[**18**] and charge ordering,[**19**] and which is tunable by doping,[**20, 21**] strain,[**22**] and an applied electric field.

However, the same charge, spin, lattice, and orbital degrees of freedom that make the LAO/STO system so fascinating from the point of view of fundamental physics as well as applications, also make it challenging to understand, and hence control. An important goal in this field of study is to unravel the specific dependencies of sample properties on various control parameters. One approach to do this is to study STO based 2DCGs other than the (001) oriented LAO/STO system, which has so far been the main focus of research. It was recently discovered that the (110) and (111) oriented LAO/STO interfaces can also host 2DCGs.[**5**] The 2DCG in the (111) oriented LAO/STO system has been predicted to show topological behavior, owing to the hexagonal symmetry of its band structure, similar to materials such as graphene and certain transition metal dichalcogenides.[**23, 24, 25**] While this system is similar to (001) oriented LAO/STO in some ways, it also has properties that can be starkly different from the (001) oriented interface, with intriguing anisotropies in transport properties, and an electronic nematic phase that can be tuned by an electric gate.[**10, 19, 21, 26**]

In this thesis, I describe my work on the 2DCG at the interface of (111) oriented $(La_{0.3}Sr_{0.7})(Al_{0.65}Ta_{0.35})$ (LSAT) and STO. LSAT has a 1% lattice mismatch with STO,

as compared to a 3% mismatch between LAO and STO. Unlike LAO, LSAT undergoes a structural cubic to tetragonal transition around the same temperature as STO does.[**27, 28**] These factors lead to a reduced strain in the LSAT/STO heterostructure as compared to the LAO/STO heterostructure, which can affect the material properties. The first studies of (001), (011) and (111) oriented LSAT/STO 2DCGs indeed report higher carrier mobilities as compared with LAO/STO 2DCGs grown under the same conditions, a behavior which has been attributed to the lower strain in LSAT/STO systems.[**29**] However, a detailed understanding of how this reduced strain might affect the band structure is yet to emerge. Additionally, the proximity of the Ta atoms (Z = 73) in LSAT with the 2DCG, may cause the SOI in the LSAT/STO system to differ from that in LAO/STO system, which can also influence transport properties of the system. It would be interesting to see which phenomena are shared between (111) LSAT/STO and (001) or (111) LAO/STO, and which phenomena differ, as steps towards understanding the mechanisms behind these phenomena.

I have studied transport in the (111) LSAT/STO 2DCG, as a function of temperature, electric field applied through a back gate voltage, and magnetic fields parallel and perpendicular to the sample surface, in order to shed light on some of these questions. I shall describe my findings in the remainder of the thesis, which is organized as follows:

Chapter 2 is the background on which the thesis rests. It is divided into five broad sections: The first section is a survey of what we know about the physics of bulk STO, since this material plays an active role in determining system properties. In the second section I will describe the effects of adding an interface, namely, the formation of an interfacial potential well and the ordering of orbitals. In the third section I will discuss

the effect of applying a gate voltage, V_g, on sample properties. In the fourth section I will make a connection to our experiments by describing the various contributions to the resistivity of our sample as a function of temperature, T, and magnetic field B, and review what is known so far about the various contributing phenomena occurring in (001) oriented LAO/STO and (111) oriented LAO/STO. Finally, I will summarize the work done so far on LSAT/STO heterostructures in section 5.

Chapter 3 describes the experimental techniques used to fabricate, characterize and measure the (111) LSAT/STO sample. I will first discuss the process of pulsed laser deposition (PLD) which is used to epitaxially deposit LSAT on STO, with a focus on various factors which can undermine epitaxial growth, since this can have consequences for the reliable measurement of sample transport properties. I will then briefly outline the sample cleaning and photolithography processes used to fabricate the Hall bars measured in this study. I will discuss also the process of making photomasks, and give a detailed account of the ion milling setup and process. I will finally describe the low-temperature electrical transport measurement techniques used, along with the care to be taken while measuring LSAT/STO samples in particular.

Chapter 4 contains a description of my experimental results, and is divided into the following sections: (i) Temperature dependence and gate voltage dependence data, (ii) Transverse and longitudinal magnetoresistance measurements at $T = 4.2$ K in perpendicular fields up to 10 T, which point to the type of bands and charge carriers participating in transport, (iii) Longitudinal magnetoresistance measurements in perpendicular fields at $T = 4.2$ K which show the evolution of a strong SOI in the system at low electron densities, (iv) Quantitative analysis in terms of weak localization/antilocalization, magnetic

scattering, electron-electron interaction contributions, and classical magnetoresistance, of longitudinal magnetoresistance data at millikelvin temperatures, and (v) Magnetoresistance measurements which show that concomitant with an increase in SOI, an ordered ferromagnetic state emerges in the sample at low electron densities, at sub-Kelvin temperatures.

In Chapter 5, I summarize the thesis, and discuss future directions of study. These include detailed investigations of the weak localization, electron-electron interaction, and magnetic scattering contributions using a combination of field cooling and perpendicular and parallel magnetoresistance measurements. Annealing the sample in an oxidizing as well as reducing atmosphere can illuminate the effect oxygen vacancies have on this system, and help to compare and contrast it further with LAO/STO, thus enabling us to pinpoint the essential features that give rise to particular sample properties. Low temperature scanning probe microscopy can enable the detection of spin textures that may arise from the effect of strong SOI on exchange coupled moments and/or itinerant electrons.

CHAPTER 2

Background: Theory and Experiment

Over the course of the past decade, a substantial body of theoretical and experimental work dealing with STO-based complex oxide heterointerfaces has emerged. In this chapter, I will discuss the relevant background which will help us understand my work on (111) oriented LSAT/STO, and see how it fits into the framework of this rapidly developing field.

The chapter is divided into five sections. In the first section I will briefly review the physics of bulk STO, discussing its structure and the structural transitions it undergoes at different temperatures, its electronic band structure, and dielectric properties. It is the electronic bands of STO, modified by the presence of an interface, that participate in all the interesting behavior observed in STO-based 2DCGs. In the second section I will discuss the effect that the interface has on the bulk band structure of STO, including the formation of the potential well at the interface, as well as orbital ordering depending on inversion symmetry breaking, crystal orientation, SOI, and strain. In the third section I will describe the effect that an applied electric field, or gate voltage V_g, has on the properties of the interfacial 2DCG. In the fourth section, I will present the theoretical background on the basis of which electrical transport data are analyzed. This includes the understanding of various T and B dependent contributions to sample resistivity, and their relative importance in different regimes of V_g, T, and B, in the context of STO-based 2DCGs. I will

also describe the various observed phenomena in STO-based 2DCGs, namely, conductivity, superconductivity, superconductor-insulator transitions, magnetism, the coexistence of superconductivity and magnetism, and spin-orbit interactions in the system, focusing in particular on (001) oriented LAO/STO and (111) oriented LAO/STO. The intention is to compare and contrast the behaviors of these systems that have been observed so far, and hence to motivate my V_g, T, and B dependence studies on (111) LSAT/STO. In the fifth and final section, I will discuss what is known so far about the LSAT/STO 2DCGs.

For a more detailed review of some of the topics mentioned above, I will point the reader to the theses of Manan Mehta [**30**] and Sam Davis, [**31**] previous graduates of the Northwestern Mesoscopic Physics Group.

2.1. Overview of the physics of bulk $SrTiO_3$

LAO, LSAT, and STO belong to the class of perovskite oxide materials. A representation of the general unit cell structure for these materials, which have a chemical formula ABO_3, is shown in Fig. 2.1. Here A and B are cations, A being larger in size than B. In the case of STO, the ion A is Sr^{2+} which has the electronic configuration $[Kr]5s^0$, and is formed from the Sr atom which has the electronic configuration $[Kr]5s^2$. The B ion is Ti^{4+}, which has the electronic configuration $[Ar]3d^04s^0$, and is formed from the Ti atom which has the electronic configuration $[Ar]3d^24s^2$. Along the <001> directions, the crystal is made up of alternating planes of neutral SrO and TiO_2 layers. In the ideal structure with cubic symmetry, the Ti^{4+} cations are 6-fold coordinated, surrounded by an octahedron of O^{2-} ions.

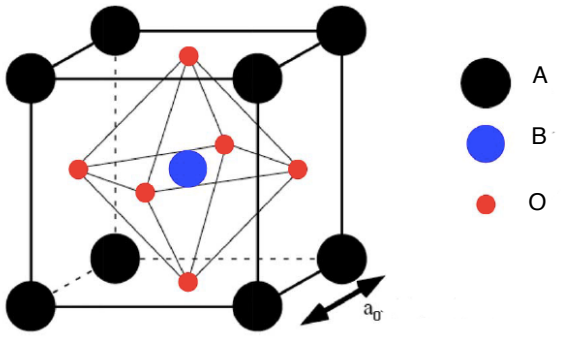

Figure 2.1. **a,** Unit cell representation of STO. The black circles denote the Sr^{2+} ions, the blue circles denote the Ti^{4+} ions, while the red circles denote the O^{2-} ions. The unit cell edges are oriented along the <100> family of crystal directions, with a cell edge of length 3.905 Å. Figure and caption adapted from Ref. [**33**].

The bonding between the Sr^{2+} ions and the O^{2-} ions is predominantly ionic. However, there is a significant degree of covalency in case of the bonding between the Ti^{4+} and O^{2-} ions, with about 85 % ionicity.[**32**] This determines the band structure of pure STO as having a filled valence band with a mainly $2p$ character, and an empty conduction band with a $3d$ character, thus making the material a band insulator with an indirect band gap of $\sim$ 3.25 eV, and the Fermi energy in the middle of the gap. Given that the Ti ions live in the octahedral crystal field of O ions, the degeneracy of the Ti $3d$ orbitals is split, with the three t_{2g} orbitals, namely, d_{xy}, d_{yz}, and d_{zx} lower in energy than the two e_g orbitals, $d_{x^2-y^2}$ and d_{z^2}, by a few eV.[**34**] Thus the conduction band structure of a perfect cubic STO crystal near the Γ point is as shown in Fig. 2.2(a), with the lowest energy conduction bands made up of the three Ti $3d$ t_{2g} orbitals, degenerate at the Γ point.[**34, 35, 36**] Along the one of the Γ-X directions in a cubic crystal, the d_{zx} orbitals have the smallest overlap, or equivalently, the smallest intra-orbital hopping term, and hence carriers in the d_{zx} band have the heaviest effective mass, while carriers in the

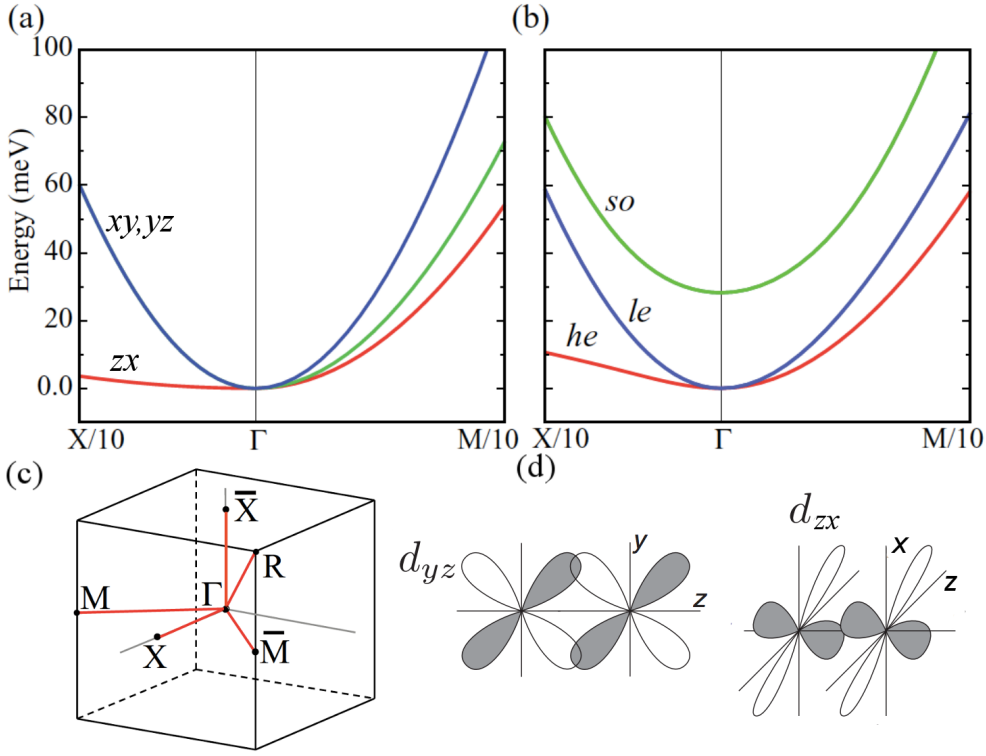

Figure 2.2. **a,** Band diagram near the Γ point of a cubic STO crystal, without including the effect of SOI. **b,** Band diagram near the Γ point of a cubic STO crystal, including the effect of atomic SOI, showing a splitting due to SOI of 28 meV. *he*, *le*, and *so* stand for the heavy-electron, light-electron, and spin-orbit split off bands, respectively. **c,** High symmetry points of the Brilluoin zone of a cubic unit cell structure. Images and captions adapted from Ref. [**34**]. **d,** Along the Γ-X direction, d_{yz} orbitals overlap more than d_{zx} orbitals. Image and caption adapted from Ref. [**37**].

degenerate d_{xy} and d_{yz} bands are lighter, as shown in the left half of Fig. 2.2(a). Along the Γ-M direction, which points along the lobes of one of the t_{2g} orbitals, the overlaps of the orbitals are different, and inter-orbital hopping terms also contribute,[**37**] hence the t_{2g} manifold along this direction is made up of three non-degenerate orbitals formed by the mixing of the d_{xy}, d_{yz}, and d_{zx} orbitals, as shown in the right half of Fig. 2.2(a).

Figure 2.2(b) shows the change in band structure when SOI effects are included. An electron moving through an electric field experiences a magnetic field in its rest frame, according to the theory of special relativity.[**38**] Since the electron has a magnetic moment owing to its spin, it experiences an energy shift due to the presence of this relativistic magnetic field, which is the SOI correction, Δ_{SOI}, to electron energy. In a solid, there are three types of SOI to be considered: inversion symmetry independent, i.e., Pauli or atomic SOI (ASO), and inversion symmetry dependent Rashba and Dresselhaus SOI.[**38**] For an electron moving in the electric field of an atom with atomic number Z, $\Delta_{SOI} \sim Z^4$, and ASO causes a mixing and splitting of the atomic energy levels depending on the quantum number J associated with the atomic orbitals. In a solid, ASO splits energy band levels by a similar mechanism. The band diagram in Fig. 2.2(b) is the result of this ASO acting on the t_{2g} bands of STO. If time reversal symmetry is present in a crystal, then we have $E_{\uparrow}(\mathbf{k}) = E_{\downarrow}(\mathbf{-k})$, where the **k**s are wave vectors, and the subscripts denote up and down spin states. If inversion symmetry is also present, like in the case of bulk STO, we also have $E_{\uparrow}(\mathbf{k}) = E_{\uparrow}(\mathbf{-k})$, giving a twofold Kramer's degeneracy of the single-particle energies, $E_{\downarrow}(\mathbf{-k}) = E_{\uparrow}(\mathbf{-k})$.[**39**] However, the breaking of inversion symmetry may lead to the removal of the spin degeneracy even in the absence of an external B field, and may give rise to two *different* energy dispersion branches, $E_{\uparrow}(\mathbf{k})$ and $E_{\downarrow}(\mathbf{k})$, so that Kramer's degeneracy is broken everywhere except at $\mathbf{k} = 0$. This happens because inversion asymmetry changes the electric field environment of the electrons, giving rise to an SOI correction to electron energies.

There are two main ways in which this can happen in a quasi 2-dimensional system: one occurs if the crystal possesses bulk inversion asymmetry, as in the case of the zinc

blende structure, and is known as the Dresselhaus effect, and the other occurs due to an inversion asymmetry of the confining potential, as in the case of interfacial 2DCGs, and is known as the Rashba SOI (RSO). The Rashba Hamiltonian is given as $H_R = \alpha(\hat{\mathbf{n}} \times \mathbf{k}) \cdot \mathbf{S}$. Here $\mathbf{S}$ are the Pauli matrices and $\hat{\mathbf{n}}$ is the unit vector perpendicular to the 2DCG plane. The Rashba coupling constant α is dependent on the magnitude of ASO, Δ_{SOI}, as well as on any potential gradient applied perpendicular to the 2DCG, and is hence tunable using electrical gating. Thus RSO leads to a k dependent splitting of energy bands.[**38**] In STO-based 2DCGs, given that the crystal structure does possess bulk inversion symmetry, ASO and RSO effects are considered to dominate, rather than the Dresselhaus effect. The effect of the inversion symmetry dependent RSO on the band structure will be discussed later. The details of how the gate voltage may affect RSO are important for understanding my results on (111) LSAT/STO, and will also be discussed later.

Slight imperfections, strain (see Fig. 2.3),[**34**] as well as reduced temperatures can lead to a departure from the highly symmetric state described above. At $\sim$ 105 K, STO is known to undergo a structural transition from a cubic to an antiferrodistortive tetragonal phase, characterized by an antiphase rotation of the TiO_6 octahedra about one of the <100> axes, as well as an expansion of the unit cell along the axis of rotation.[**27**] Under extreme conditions, such as high pressure, or replacement of some O^{16} atoms with O^{18} atoms, there is some evidence for the development of orthorhombic and rhombohedral phases.[**40**] These transitions have an effect on the band structure, and hence on sample properties. The second-order cubic to tetragonal transition leads to domain formation depending on which axis happens to be randomly chosen as the axis of rotation for the oxygen octahedra, which can be significant for transport, as we shall see later.[**41**] The

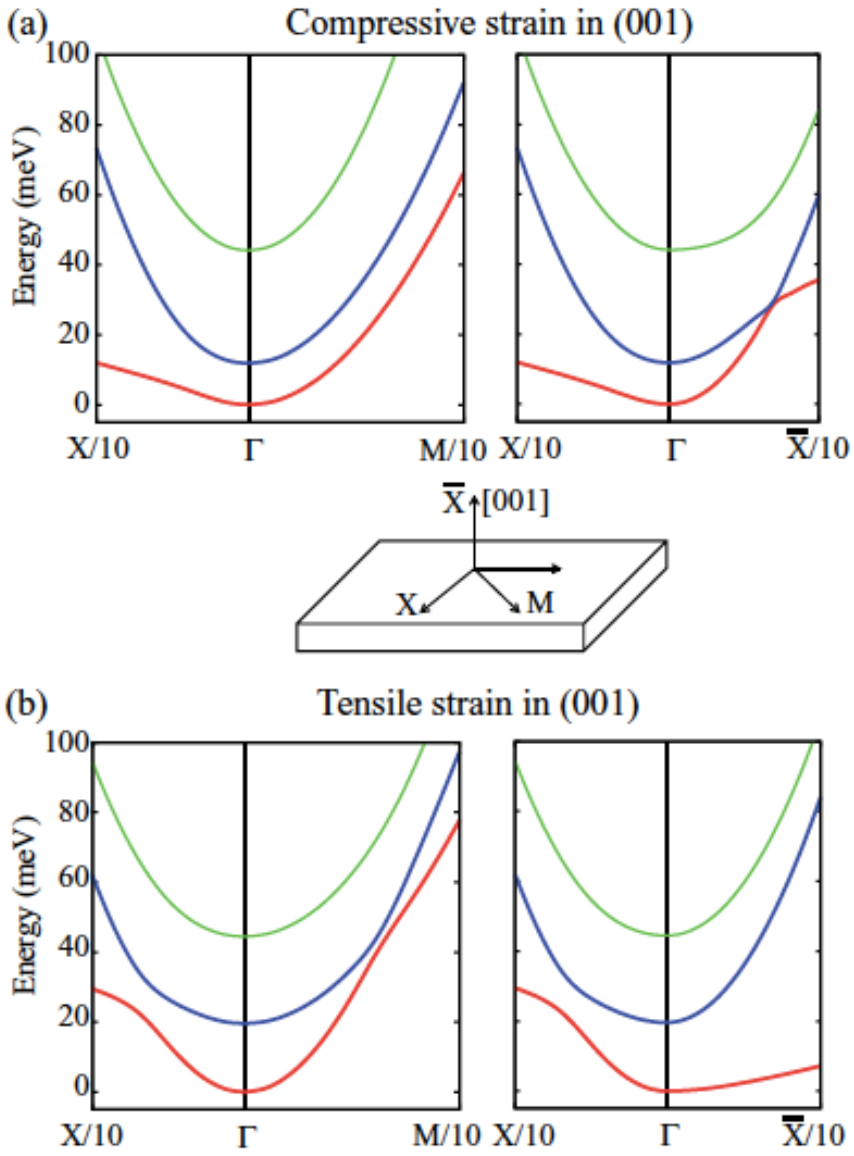

Figure 2.3. Band diagram of STO at the conduction band minimum at Γ under **a,** a -1% compressive and **b,** a +1% tensile strain, plotted along the X-Γ-M and X-Γ-$\bar{X}$ directions. Note that the X and $\bar{X}$ points are not equivalent as strain is applied in the $X - \Gamma - M$ plane. The effects of ASO are included. Image and caption taken from Ref. [**34**].

tetragonal phase is believed to be a precursor to the quantum paraelectric phase observed below about 37 K.[**6**]

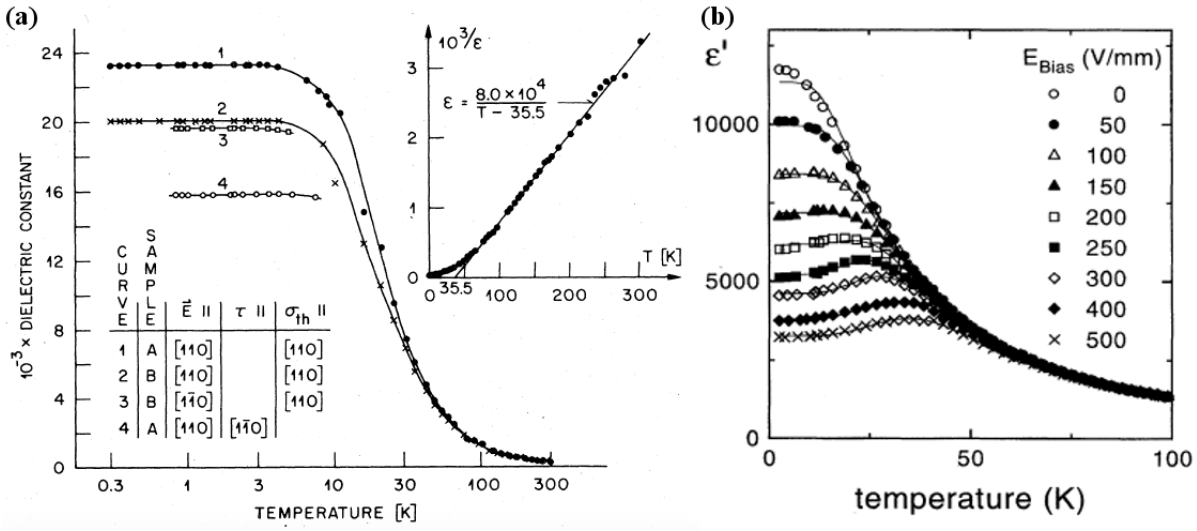

Figure 2.4. **a,** Dielectric constant of the monodomain STO samples. Inset: $10^3/\epsilon$ vs. T. Image taken from Ref. [**6**]. **b,** Temperature dependence of the dielectric constant in STO for various bias fields between 0 V/mm and 500 V/mm as described in the figure. The solid lines are fits to a mean field theory. Image taken from Ref. [**7**].

At room temperature, STO has a high dielectric constant of about 300, owing to the polar nature of its bonds, which makes it an attractive dielectric. Below about 37 K, the dielectric constant increases sharply due to incipient ferroelectricity, as shown in Fig. 2.4(a), but saturates below about 4 K, since the zero-point motion of its constituent atoms renders it a quantum para-electric.[**6**] This high dielectric constant is dependent on an applied electric field.[**7**]

STO possesses properties that make it one of the most suitable materials to be used as substrate for the epitaxial growth of other oxide films. It is closely lattice matched

with many other perovskite oxides of importance, such as the cuprate superconductors and colossal magnetoresistive manganites. The growth techniques for STO are well established[**42**] and the techniques for obtaining atomically flat STO crystals of the desired terminations are also well known, albeit not trivial to achieve perfectly.[**43, 44**] Coupled with its dielectric properties, these factors have made it the workhorse of oxide-based research.

However, STO is not simply a passive spectator to the physics that may happen in the thin films deposited on it, which can be a boon or bane depending on one's point of view. It was found that doping STO with La^{3+} substituted for Sr^{2+}, or Nb^{5+} substituted for Ti^{4+},[**45**] or annealing in a reducing atmosphere to induce oxygen vacancies,[**46**] can render STO conducting. What is more, for carrier densities around $5 \times 10^{18}/cm^3$ to $5 \times 10^{20}/cm^3$, STO becomes superconducting at temperatures below about 300 - 400 mK.[**47**] The structural transitions that STO undergoes can change the environment locally for any phenomena that may occur in the films deposited on top of STO, as well as at the interface itself. Strain can transform the quantum para-electric state of STO into a ferroelectric state near the interface,[**48**] which can also affect properties near the interface. We will next look at one of the most striking effects to be observed at the interface when another insulating perovskite, such as LAO, is deposited epitaxially on top of STO: the formation of a 2DCG.

2.2. Effect of the interface

In 2004, Ohtomo and Hwang discovered that when four or more unit cells of LAO were deposited epitaxially on top of TiO_2 terminated (001) oriented STO, the interface between

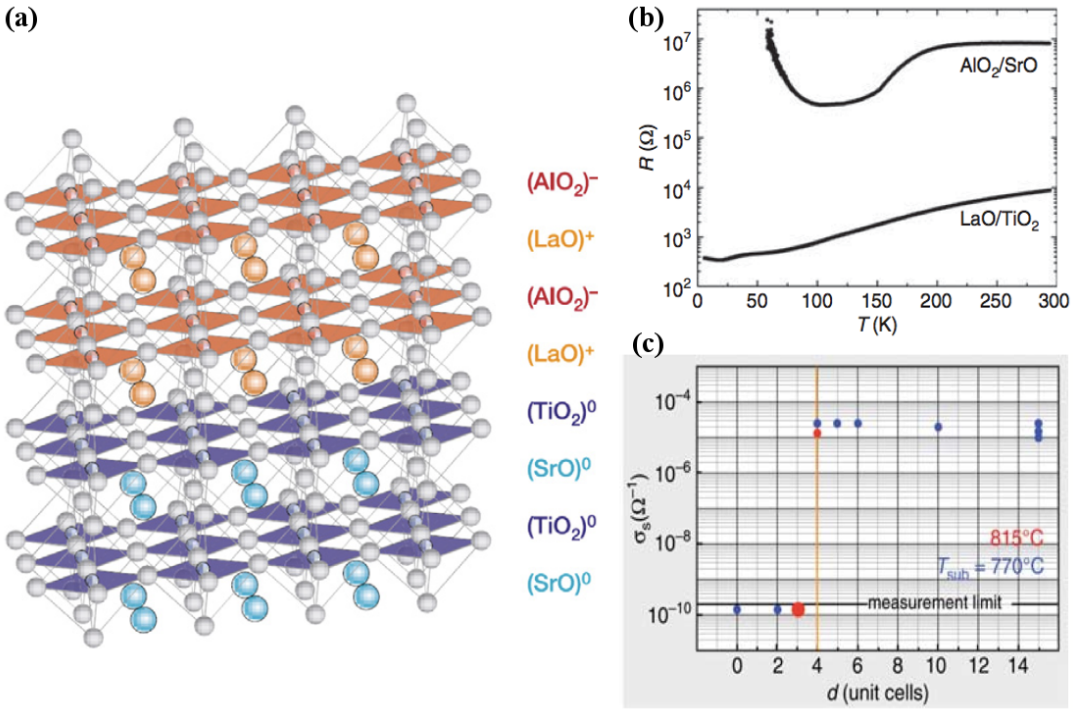

Figure 2.5. **a,** The layered LAO/STO crystal structure along the (001) direction. Image and caption adapted from Ref. [**4**]. **b,** Variation of resistance vs. temperature for SrO terminated and TiO_2 terminated (001) LAO/STO 2DCGs. **c,** Variation of conductance with the number of LAO unit cells deposited epitaxially on TiO_2 terminated (001) oriented STO. Images and captions adapted from Ref. [**49**].

these large band gap insulating oxides became conducting, whereas the corresponding SrO terminated interface was insulating.[**4**] It was rapidly discovered that this 2DCG showed a multitude of physical phenomena, and stimulated a lot of experimental and theoretical efforts to understand the mechanisms behind these effects. The existence of the 2DCG also spurred a debate regarding its origins. We will next look at the various mechanisms proposed to explain the existence of the 2DCGs.

2.2.1. Formation of the interfacial potential well

In order to understand the proposed mechanisms for the formation of the 2DCG, we must begin by describing LAO. LAO is a band insulator with a band gap of 5.6 eV.[**50**] At room temperature it has a rhombohedrally distorted perovskite structure which can be described as a pseudocubic structure with a lattice parameter of 3.791 Å.[**50**] Epitaxial deposition of LAO on STO subjects STO to a compressive strain owing to the lattice mismatch of 3 % between LAO and STO, which has a lattice constant of 3.905 Å.[**50**]

Along the <001> directions, LAO consists of alternating planes of AlO_2^- and LaO^+, as opposed to the charge neutral SrO and TiO_2 planes of STO. In the light of this polarity mismatch that occurs at the interface between these materials, one of the mechanisms proposed for the formation of the 2DCG was electronic reconstruction. To understand this, we note that due to its alternating charged layers in the (001) orientation as shown in Fig. 2.6(a), the LAO layers have a formal polarization, pointing from the LAO^+ layers to the AlO_2^- layers. This polarization is given as $P_0 = e/2S = 0.520$ C/m^2, where e is electronic charge and S is the unit-cell cross-section in the plane of the interface. On the other hand, in STO the polarization is zero since the TiO_2 and SrO layers are charge neutral. In the absence of free charge at the LAO/STO interface, the preservation of the normal component of the electric displacement field D along the STO/LAO/vacuum stack leads to the appearance of a macroscopic electric field in LAO, $E_{LAO} = P_0/\epsilon_0\epsilon_{LAO}$, which, given that $\epsilon_{LAO} = 24$, is equal to ~ 0.24 V/Å. This leads to a diverging potential build-up as the thickness of the LAO layer is increased.

One way to resolve this so-called polar catastrophe is through electronic reconstruction. In the case of a n-type TiO_2-LaO^+ interface, half an electron per unit cell must

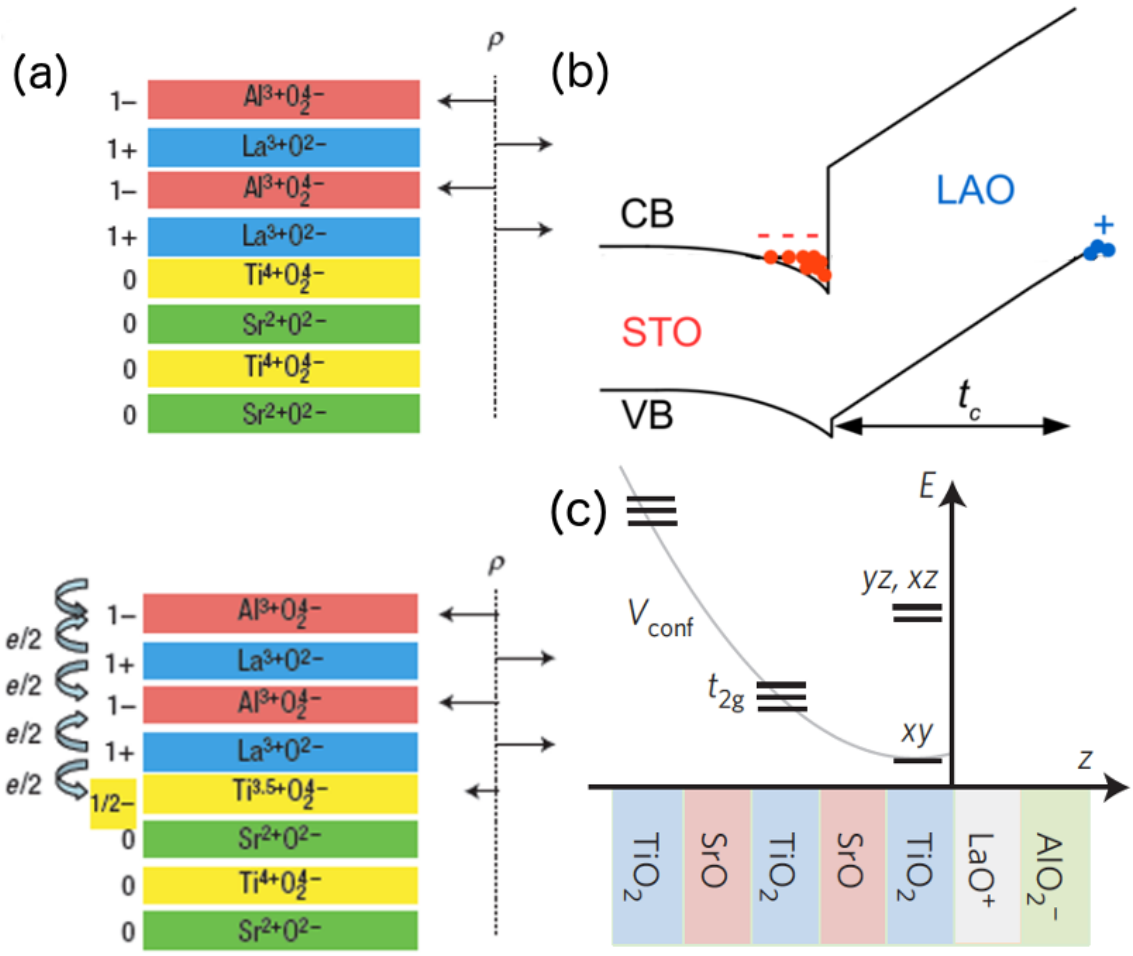

Figure 2.6. **a,** Layered LAO/STO structure. Upper panel shows a charge (ρ) imbalance at the interface, leading to a potential build-up in the LAO film. Lower panel shows the electronic reconstruction which occurs by the transfer of electrons from the LAO surface to the interface. Image and caption adapted from Ref. [**51**]. **b,** The bending of LAO bands due to the electronic reconstruction over a length scale of t_c, until the LAO valence band and STO conduction band are at the same energy, when electrons are transferred from the LAO surface to the interface. CB and VB are the conduction and valence bands of STO. **c** Schematic showing orbital ordering in the different TiO_2 layers in the interfacial potential well. Image and caption adapted from Ref. [**52**].

be transferred from the surface of LAO to the interface, as shown in Fig. 2.6(a), by the following mechanism: The electric field E_{LAO} causes the electronic bands to bend, as illustrated in Fig. 2.6(b). Since the band gap of LAO is greater than that of STO, at a thickness t_c, the valence O $2p$ bands of LAO reach the level of the STO Ti $3d$ conduction bands at the interface, which corresponds to an energy difference of $\Delta E \sim 3.3$ eV, and electrons are transferred from the surface AlO_2^- layer to the interface TiO_2 layer. This leads to a change in the charge density of the layers: instead of a stack with oppositely charged layers at the ends, we are left with a stack with similarly charged layers at the ends, thus resolving the divergence of the potential within LAO. In the TiO_2 layer at the interface, electrons transferred due to electronic reconstruction occupy the Ti $3d$ conduction bands, leading to the formation of the 2DCG. This electrostatic model predicts $t_c = \epsilon_0 \epsilon_{LAO} \Delta E / e P_0$ to be ~ 3.5 unit cells of LAO, which agrees remarkably well with experiment.[**4, 53**] The predicted transfer of half a electron per interfacial Ti atom would lead to a carrier density of about 3×10^{14} /cm^2, however, typical carrier densities observed in experiments are of the order of 10^{13}/cm^2, suggesting that many of the carriers are localized. The localized electrons would lead to the formation of some Ti^{3+} ions which have an electronic configuration of [Ar]$3d^1$, and can hence act as local magnetic moments.

In the case of a p-type TiO_2-LaO^+ interface, half a hole per unit cell must be transferred from the surface of LAO to the interface. Naively one would expect this interface to be conducting as well, with the extra holes going into the O $2p$ valence bands of STO, in contrast with experimentally observed insulating interface. Pentcheva and Pickett [**54**] found using density functional theory (DFT) that the transferred holes are localized near

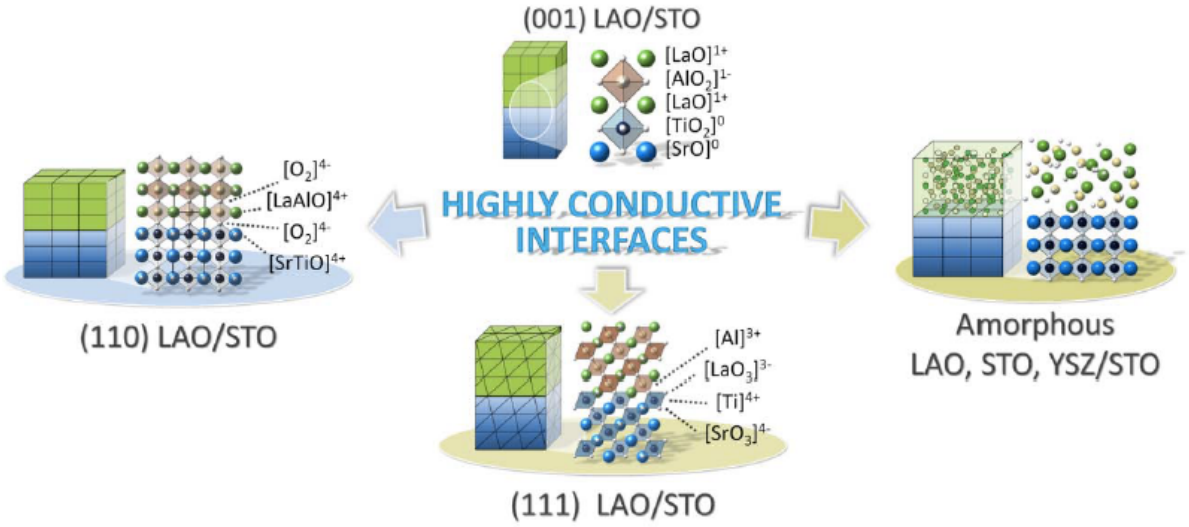

Figure 2.7. The sketches display (001)-, (110)- and (111)- oriented LAO/STO interfaces, along with oxide amorphous layers (LAO, STO, Yittria-stabilized Zirconia oxides) interfacing (110)-oriented STO, all of them exhibiting high-mobility conduction. Image and caption from Ref. [**5**].

oxygen vacancies, which can have excess electrons in their vicinity, forming a bound state with the holes, and leading to an insulating interface.

There are, however, 2DCGs formed at the interfaces between amorphous insulating Al_2O_3 and LAO films and STO, or between (110) oriented LAO and STO,[**5, 20**] which do not show the polarization discontinuity described above (see. Fig. 2.7). To explain this, it was proposed that oxygen vacancies play a crucial role in the formation of the 2DCG. These exist naturally in complex oxides, and can be created by bombardment of energetic ions,[**55, 56, 57**] UV exposure under vacuum,[**36, 58**] during growth in a low oxygen partial pressure atmosphere,[**11**] and during annealing of the heterostructures in a reducing atmosphere.[**10**] The understanding of oxygen vacancies is important given the role they may play in determining transport properties.

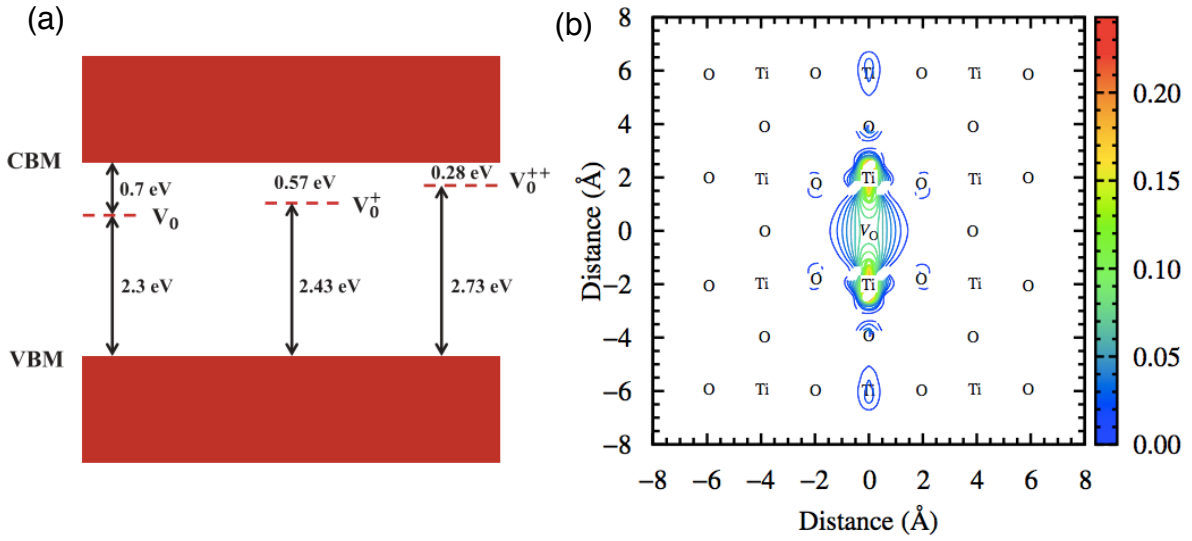

Figure 2.8. **a,** Energy levels of defect states created by isolated neutral (V_0), singly ionized (V_0^+) and doubly ionized (V_0^{++}) oxygen vacancies in bulk STO, calculated using hybrid DFT. Image and caption adapted from Ref. [**60**]. **b,** Contour plot of spin density for an isolated neutral oxygen vacancy (V_0) in a TiO_2 layer in bulk STO. The color bar shows magnitude of magnetic moment. Using the GGA + U approximation, the Ti ions neighboring the vacancy are found to carry magnetic moments of ~ 0.22 μ_B each, oriented parallel to each other. Image and caption adapted from Ref. [**61**].

Neutral oxygen atoms leave the crystal, leaving behind two trapped electrons at the vacancy site, in the fully ionic picture.[**59**] This maintains the overall charge neutrality of the unit cell, and is hence considered to be a neutral vacancy. If these electrons remain localized around the vacancy, they can change the charge state of the neighboring Ti ions from Ti^{4+} to Ti^{3+}, creating magnetic moments as shown in Fig. 2.8(b). If one or both of these electrons ionize and go into the t_{2g} conduction band, a charged vacancy can be created while making the material more conducting. For all charge states of the vacancy, donor states are created, as shown in Fig. 2.8(a), and their specific charge, orbital nature, magnetic character and energy level is determined by their environment:

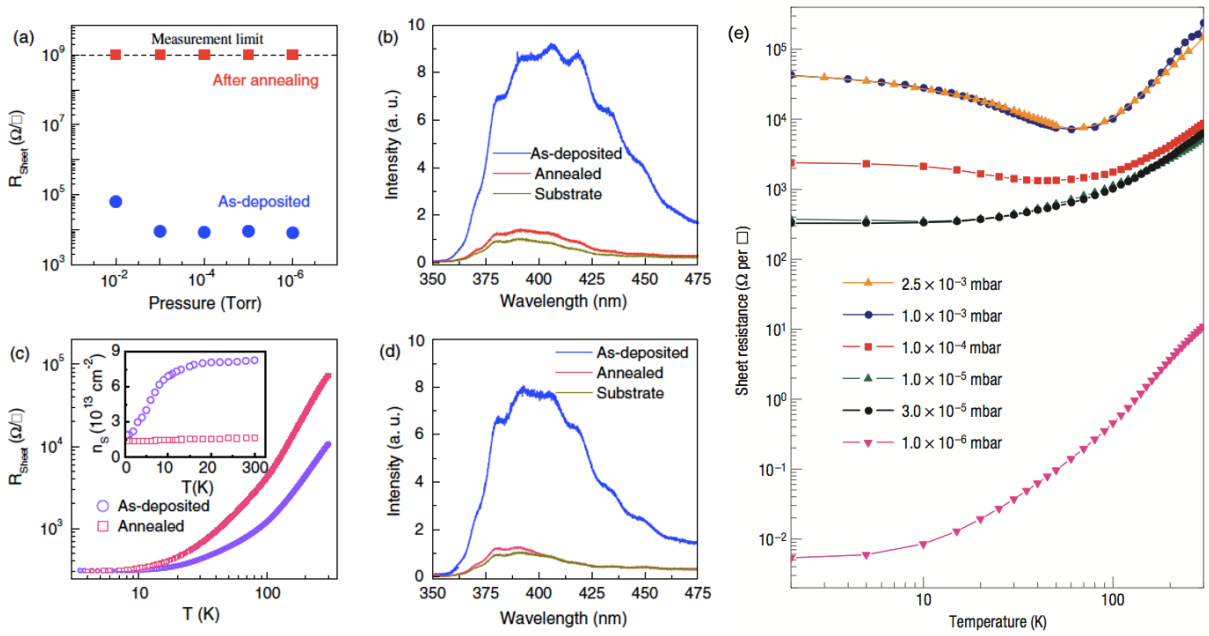

Figure 2.9. **a,** Room temperature sheet resistance of 20 nm amorphous LAO/STO heterostructures prepared at different oxygen pressures, before and after annealing in 1 bar of oxygen gas flow for 1 hr at 600 C. **b,** Photoluminescence intensity of 20 nm amorphous LAO/STO fabricated in 10^{-6} Torr, before and after oxygen annealing. **c,** Sheet resistance vs. temperature (Inset: carrier density vs. temperature) of 10 unit cell crystalline LAO/STO heterostructures grown in 10^{-3} Torr and 750 C before and after oxygen annealing. Images and caption adapted from Ref. [**20**]. **e,** Sheet resistance vs. temperature of epitaxial LAO/STO heterostructures grown at different oxygen partial pressures. Image and caption adapted from Ref. [**11**].

whether the vacancy is isolated or clustered, on the surface or in the bulk, and if the tetragonal transition has occurred, whether or not the vacancy is on the rotation axis of the oxygen octahedron.[**61, 62, 63**] Theoretically predicting the physical mobility of the vacancy, and the localization or itineracy of the two electrons left behind is difficult, since the results are sensitively dependent on the particular flavor of DFT used and the size of supercell used for computations.[**60, 61**]

Some recent theories predict that electrons on the oxygen vacancies near the surface or interface are more delocalized as compared to the electrons inside the bulk, and the donor levels are closer to the STO conduction band near the interface, as compared to in the bulk,[**63, 64, 65**], which is in line with the experimental observation that the surface of STO can more easily be rendered conducting as compared to the bulk.[**66**] Due to the low diffusion constant of these defects in STO ($\sim 10^{-10}$ cm^2/s),[**67**] and also due to favorable energetics, they tend to cluster near the interface, rather than diffuse into the bulk.[**66**] Near the interface, the electrons from the donor levels created by the oxygen vacancy can be thermally excited into the Ti conduction band, leading to the observed increased conduction at the interface, and creating positively charged vacancy sites. At lower temperatures however, electrons can fall back from the conduction band into empty donor levels, and thus become localized, decreasing the itinerant carrier density at the interface. Measurements of sheet carrier density of as-grown and oxygen-annealed (001) LAO/STO as a function of temperature have shown that the carrier density follows an activated behavior, with activation energies ranging from $\sim$ 4 meV to $\sim$ 0.5 meV.[**20**] These activation energies have been associated to the energy difference between the conduction band level and donor levels due to oxygen vacancies, and are clearly much smaller than the energy differences between the conduction band and donor levels in the bulk, as shown in Fig. 2.8(a). If electrons are localized at vacancy sites, they can impart magnetic moments to the neighboring Ti ions. These have been observed by X-ray measurements and are predicted using simulations of the X-ray spectra to have d_{xy} character near the interface.[**68**] Electrons at the interface away from the vacancy, which may come either from other oxygen vacancies which remain uncompensated, or from other

mechanisms, remain itinerant and can interact with the localized magnetic moments. This mechanism does explain the formation of the 2DCG in the above-mentioned systems, the reduction in carrier density at low temperatures caused by electrons falling back from the conduction band into the donor level, inhomogenous magnetic and transport properties caused by a random spatial distribution and clustering of vacancies as well as a spread in their associated energy levels, and also the effect of annealing in an oxygen atmosphere on sample conductivity.[**20**] However, it cannot explain either the fact that the SrO terminated (001) oriented LAO/STO interfaces and TiO2 terminated interfaces with less than 4 unit cells of LAO deposited on (001) STO, are insulating.

Another explanation stems from the fact that the STO layers near the interface are strained by the deposition of another material on top. It has been demonstrated that if instead of a uniform STO substrate, one uses an STO film grown on other perovskites such as $GdTiO_3$, LSAT, $NdGaO_3$, and $DyScO_3$, as substrates, one can control the conductivity of the LAO/STO 2DCG. If STO is under tensile strain, the interface was shown to be insulating, while increasing compressive strain also seemed to reduce conductivity.[**22**] In this picture, the 2DCG is believed to emerge as an electronic reconstruction in response to head-to-head polarization fields within layers of LAO and STO near the interface, resulting from ferroelectric instabilities, as shown in Fig. 2.10, and which may be modulated by strain.[**69**]

There is also the possibility that the conduction at the interface is due to the intermixing of the La^{3+} cations and the Ti^{4+} cations near the interface.[**70**] Given the complexity of the system, it is likely that all of these mechanisms play a role in the formation and control of the 2DCG to varying degrees, depending on growth and processing methods,

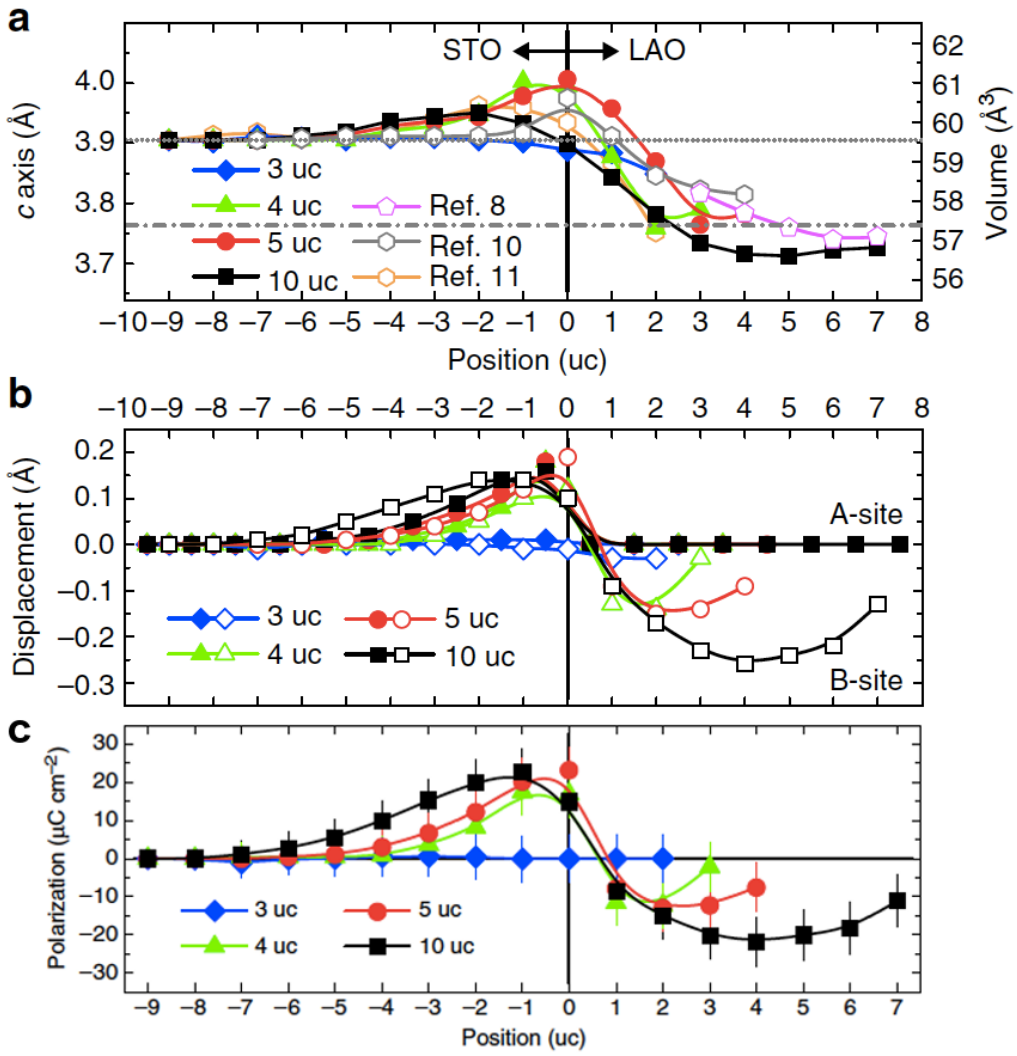

Figure 2.10. **a,** c-axis unit cell dimension and unit cell volumes near the LAO/STO interface studied by surface X-ray diffraction, for different thicknesses of the LAO layer. Dotted (dashed-dotted) grey lines are the undistorted unit cell dimensions for STO and LAO. **b,** Corresponding atomic displacements, positive sign directs towards the interface. **c,** Head to head polarizations in LAO and STO layers near the interface. Note the null result for 3 unit cells of LAO. Images and caption adapted from Ref. [**69**].

as well as the specific combination of materials used. It is clear however that the 2DCG, once formed, resides in a few TiO_2 layers near the interface.

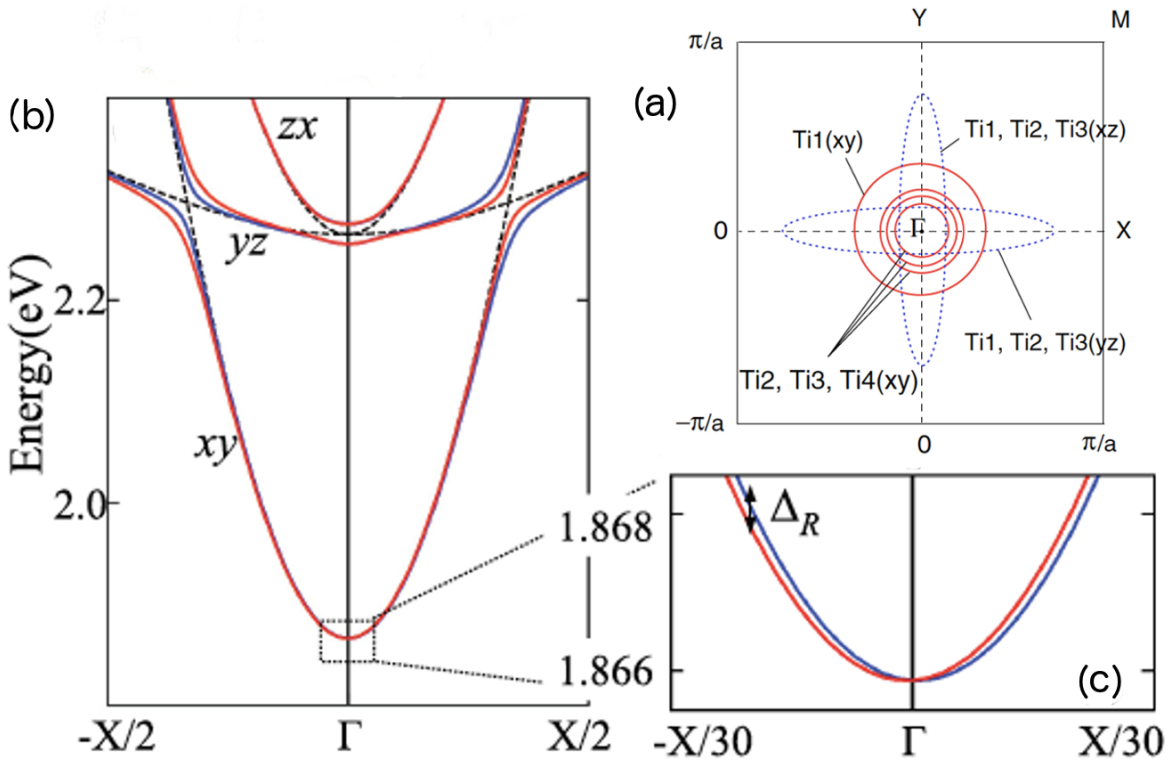

Figure 2.11. **a,** Idealized Fermi surface for the isolated (001) LAO/STO interface, showing bands in different TiO_2 layers near the interface, without considering effects of SOI. The circular Ti1, Ti2, Ti3, Ti4(xy) are the d_{xy} orbitals in the first four TiO_2 layers near the interface, with Ti1(xy) being closest to the interface. The elliptical Ti1, Ti2, Ti3(yz) and (xz) bands are the d_{yz} and d_{zx} orbitals in the first three TiO_2 layers near the interface. Image and caption adapted from Ref. [**71**]. **b,** Band dispersions calculated using a tight binding Hamiltonian near the Γ point show the orbital ordering of d_{xy} and d_{yz}, d_{zx} orbitals caused by the interface. Dotted black lines show the band structure without considering effects of SOI. Red lines show the energy splitting caused by ASO. **c,** Zooming in at the bottom of the d_{xy} band reveals the effects of Rashba SOC. Image and caption adapted from Ref. [**73**].

2.2.2. Orbital ordering

The presence of the interface breaks inversion symmetry and leads to the breaking of degeneracy among the Ti 3d t_{2g} bands in the TiO_2 layers near the interface, and the

presence of the interfacial confining potential can lead to the formation of sub-bands from these non-degenerate Ti 3d bands. The details of the orbital ordering are dependent on SOI, crystal orientation, as well as strain.

The band structure in case of 2DCGs in (001) as well as (111) oriented STO have been studied theoretically using first-principles DFT calculations. For (001) oriented interfaces, it was predicted by Popovíc *et al.* [**71**] that the in-plane d_{xy} orbitals are lower in energy than the anisotropic out-of-plane d_{yz} and d_{zx} orbitals, as shown in Fig. 2.11. The splitting between these three orbitals becomes smaller as we move away from the interface. The d_{xy} orbitals in the TiO_2 layer closest to the interface lie deepest in the interfacial potential well, and have little overlap with the d_{xy} orbitals in the adjacent TiO_2 plane. Hence they have the most 2D character, making the carriers in these orbitals susceptible to localization according to Anderson's theorem,[**72**] despite their small in-plane mass. Carriers in the d_{yz} and d_{zx} orbitals in this TiO_2 layer are also prone to localization owing to their large in-plane mass. However, orbitals in adjacent TiO_2 layers further away from the interface can overlap, and are the likely participants in transport. This general picture has been used to explain many experimental results.[**52, 74, 75**] The d_{xy} character of local magnetic moments has also been confirmed by X-ray measurements,[**68**] although it is difficult to pinpoint the exact location of these moments in the different TiO_2 layers near the interface.

Held *et al.* [**73**] and Khalsa *et al.* [**76**] included the effect of ASO as well as RSO on the t_{2g} manifold in their DFT calculations, and found that the degeneracy of the d_{yz} and d_{zx} was lifted by ASO, as shown in Fig. 2.11(a), similar to what is observed in the case of bulk STO. Note that the effect of the splitting due to ASO is most significant

at the bottom of the otherwise degenerate d_{yz}, d_{zx} bands, and near band crossings. The RSO was found to be linear in momentum for electrons in the d_{xy} bands but cubic in momentum for electrons in the d_{yz} and d_{zx} bands.

Angle Resolved Photo-Emission Spectroscopy (ARPES) and Spin-ARPES experiments on vacuum cleaved STO have more or less corroborated this orbital ordering for (001) oriented STO-based 2DCGs predicted by theory. However, the data on the effect of SOI is unclear.[**36, 77, 78**] One reason for that could be that the energy splittings may be less than the resolution of these measurements, which is typically a few tens of meV. It could also be because the details are sensitively dependent on other factors such as strain.

There have been fewer studies on the band structure of (111) oriented STO-based 2DCGs, however, the results predict the existence of interesting phases in this system.[**23, 24, 25, 58, 79**] Along the <111> directions, the crystal structure of STO is made up of sheets of Ti^{4+} ions as shown in Fig. 2.12(a) and (b). One can see that the nearest neighbour Ti ions lie not in the same plane, but in different layers, as denoted by the differently colored dots. This gives rise to a buckled hexagonal crystal with C_3 symmetry. Due to this different crystal symmetry, the three Ti $3d$ t_{2g} orbitals are equivalent and degenerate at the Γ point in this orientation. Hence, whereas the bulk Fermi surface of STO cut along the (001) plane has lobes along the mutually perpendicular crystal directions <001>, as shown in Fig. 2.12(c), in case of a cut along the (111) plane, as shown by the ARPES data in Fig. 2.12(d), it has nodes along the $[1\bar{1}0]$ direction, and lobes along the $[\bar{1}\bar{1}2]$ direction, both of which lie in the plane of the 2DCG for the (111) oriented heterostructure. This leads to the presence of two heavy bands of mass 1.8 m_e and one light band of mass 0.27 m_e in the $[1\bar{1}0]$ direction, and one heavy band of mass 8.67

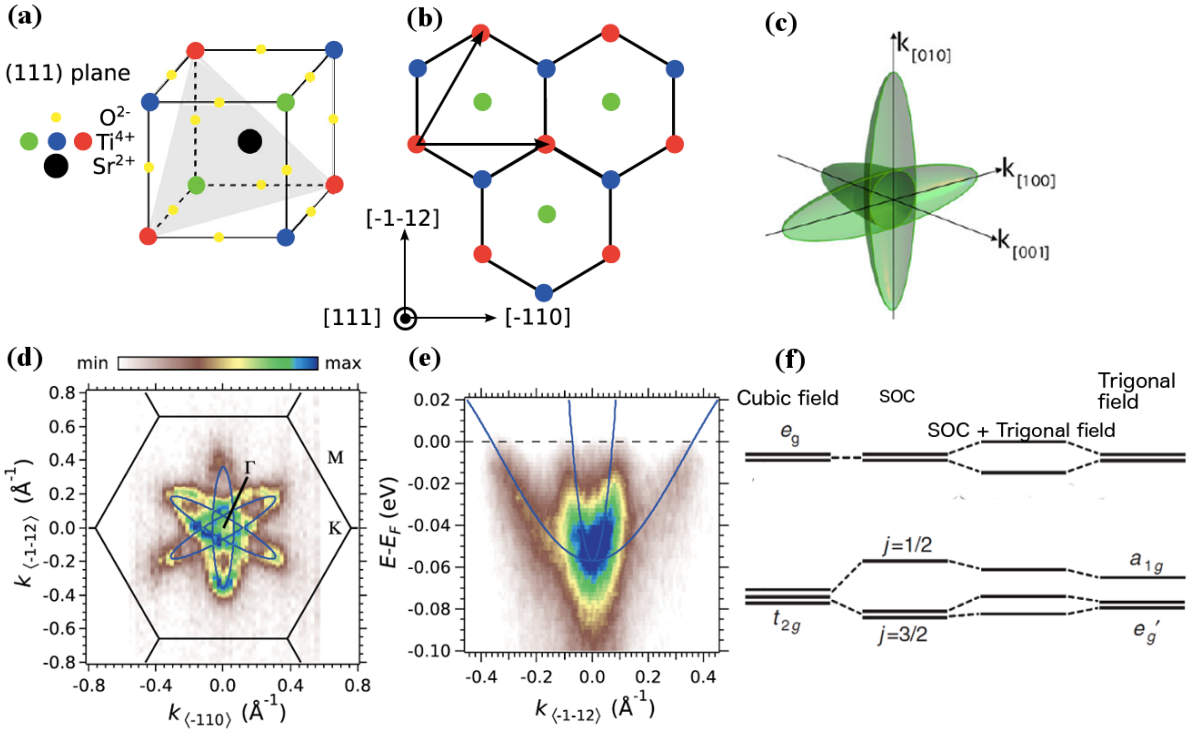

Figure 2.12. **a,** STO unit cell showing a cut in the (111) plane. **b,** A top view looking down onto the (111) plane, showing the trigonal symmetry of the Ti ions, as well as the buckled hexagonal lattice structure. The red Ti ions are in the topmost layer, blue Ti ions are in a layer below that, while the green Ti ions are in the lowest layer. Also shown is the asymmetry in the positions of Ti ions in the $[1\bar{1}0]$ and $[\bar{1}\bar{1}2]$ directions. **c,** Three dimensional bulk Fermi surface of STO showing the $3d$ orbitals. **d,** ARPES data of the 2D STO Fermi surface looking down onto the (111) plane. **e,** Energy-momentum map across the Γ point along the $<\bar{1}\bar{1}2>$ directions. The dispersions of the heavy and light bands are visible. **f,** Energy splittings of the Ti d orbitals at the Γ point, under the action of cubic and trigonal crystal fields, as well as ASO. Images and captions for Fig. **a, b, d, e** adapted from Ref. [**25**], for Fig. **c** from [**58**], and Fig. **f** from [**24**].

m_e and two light bands of mass 0.33 m_e in the $[\bar{1}\bar{1}2]$ direction, as shown by the ARPES data in Fig. 2.12(e). Here m_e is the bare electron mass.

ASO can cause the mixing and splitting of the t_{2g} manifold into $J = 1/2$ and $J = 3/2$ levels. If one only considers perturbations due to the trigonal crystal field experienced by the Ti^{4+} ions, disregarding ASO, then the Ti $3d$ t_{2g} orbitals split into a_{1g} and $e_g{}'$ orbitals as shown in Fig. 2.12(f). DFT calculations [**23**] have shown that compressive strain, such as what is expected in LAO/STO as well as LSAT/STO, can cause the e'_g doublet to be lower in energy than the a_{1g} band. If ASO and the trigonal field splitting are applied together, the e'_g doublet splits and all degeneracies except Kramer's are removed. RSO can further lift these degeneracies, and strain can change the relative ordering of these orbitals. Depending on the SOI and strain parameters, a variety of ordered states, such as ferroelectricity, ferromagnetism, and nematicity, as well as a possibility of Dirac points, have been predicted by DFT calculations for this system.[**23, 24, 79**] ARPES studies on vacuum-cleaved STO surfaces have not detected any lifting of degeneracies at the Γ point, as shown in Fig. 2.12(e),[**58, 25**] hence we can estimate the size of these splittings to be no more than a few tens of eV, limited by the resolution of the experiments. It could also be that substantial splittings only occur at STO-based interfaces and not at the STO surfaces studied in these ARPES experiments. It is clear however that some of these predicted ordered states do indeed exist in (111) oriented STO-based 2DCGs, according to transport experiments which show evidence of ferromagnetic and nematic ordered states[**31**] which we will discuss later. Interestingly, hole pockets have also been predicted to be present in the Fermi surface for systems under compressive strain, although they have not been detected by ARPES experiments.[**23**] Although the details depend on the strain in the system and the specific model of DFT used, this prediction is one of the

ways to reconcile having hole-like carriers contributing to transport, as has been verified by transport experiments which we will also discuss later.[**31**]

2.3. Effect of gate voltage

In (001) as well as (111) orientated STO-based 2DCGs, the application of an electric field through V_g affects the charge carriers which populate the complex interfacial bands in a number of ways. It can change carrier concentration by adding electrons to the interface when a positive V_g is applied, and pulling electrons out/adding hole-like carriers for negative values of V_g. It can change the shape of the potential well, its energy depth and spatial extent.[**21, 80**] At lower values of V_g, the system can develop locally carrier-depleted pockets, creating disorder.[**17**] Changing the size of the well can also change the interaction of the carriers with the interface itself, and hence change scattering due to the interface. Changing the number of carriers can change the screening of electrons from other electrons as well as charged impurities and magnetic moments such as oxygen vacancies. Finally, due to the orbital ordering near the interface, different orbitals, which may have different spatial extents and nonequivalent symmetries, for example, $d_{xy/yz/zx}$ or a_{1g} and e'_g, can fill up as carrier density is changed. Carriers in these different orbitals can interact differently with each other as well as with localized electrons of any local magnetic moments.[**75, 81**]

Changing V_g can also lead to changes in SOI by a few different mechanisms. As discussed before, ASO can mix and split bands which are otherwise degenerate. In the case of (001) STO-based 2DCGs, d_{xy} bands are known to be lower in energy, and hence as V_g is increased, the d_{xy} bands would fill first. The $d_{yz,zx}$ bands are higher, and degenerate

at the Γ point, hence more affected by ASO. Increasing V_g would eventually cause these bands to start filling, leading to an increase in SOI when the Fermi level is near the bottom of the $d_{yz,zx}$ bands. RSO depends on the strength of ASO, the momenta of electrons, as well as on the gradient of the electric field perpendicular to the 2DCG. As discussed before, ASO in (001) STO-based 2DCGs can be expected to be nonmonotonic in V_g, with a peak in magnitude when the $d_{yz,zx}$ bands just start filling. As V_g increases, Fermi energy, and hence Fermi momentum monotonically increases, giving rise to an increase in RSO. Finally, as V_g increases in magnitude, there are two different effects on the electric field seen by the 2DCG: one is that the shape of the interfacial potential well becomes broader for positive V_g, and narrower for negative V_g, as shown in Fig. 2.13. Hence the electric field perpendicular to the 2DCG is also modulated by V_g, thus making RSO stronger for higher negative values of V_g, and weaker for higher positive values of V_g. The second effect is due to the fact that the electric field increases with the magnitude of V_g. The overall observed change in SOI as a function of V_g would be determined by which of these factors dominate. In the case of (111) oriented STO-based 2DCGs, if the e'_g doublet is the lower in energy than the a_{1g} band, a larger ASO would be expected when the 2DCG is more depleted of electrons, i.e., at lower values of V_g when only the e'_g bands are filled.

Such changes in carrier concentration, disorder, interactions, and band occupation, play a starring role in the control of sample properties through V_g. In the next section, I will describe the effect of V_g on sample transport properties as a function of T and B, considering the contributions of inelastic scattering mechanisms, magnetic properties, localization, SOI, electron-electron interactions (EEI), and superconductivity of the STO-based 2DCGs.

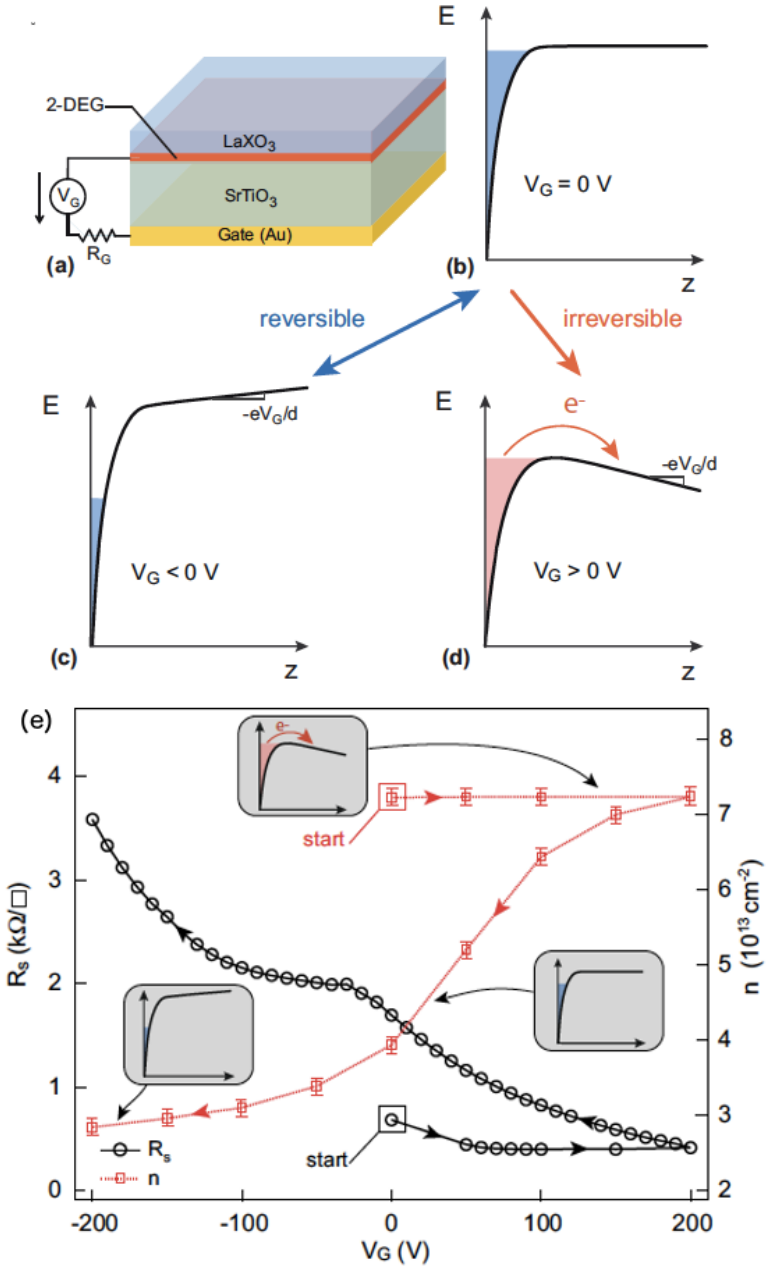

Figure 2.13. **a,** Schematic of a back gated LAO/STO system. **b,** Fermi level at the top of the interfacial potential well at $V_g = 0$ V. **c,d,** Change in Fermi level caused by the removal/addition of electrons to the interfacial potential well, as well as the change in the shape of the potential well for (c) $V_g < 0$ and (d) $V_g > 0$. **e,** Hysteretic variation of sheet resistance R_s and carrier density n on initially sweeping V_g to positive values, and then negative values. Images and captions from Ref. [**80**].

One of the first experimental observations of the effect of V_g was that the sheet resistance $R_s = 1/ne\mu$, where n is the total sheet carrier density and μ is the carrier mobility of the sample, increases as V_g is made more negative. The R_s also depends on the history of changes in V_g. When V_g is swept to negative values, R_s increases, and R_s vs. V_g retraces the same curve when V_g is swept back to 0.[**80**] However, on sweeping V_g to positive values, R_s decreases, but on sweeping V_g back to 0, R_s vs. V_g follows a different dependence, and an irreversible increase in sample resistance is seen. Biscaras *et al.* [**80**] found that they could model this behavior by an interfacial quantum well in which the Fermi level lies very close to the top of the well, as shown in Fig. 2.13(b). For $V_g > 0$, the resultant electric field causes a polarization of STO, which induces mobile electrons in the 2DCG due to screening effects, in addition to the mobile electrons present due to the mechanisms discussed earlier. This causes an initial decrease in R_s. However, the spatial extent of the well increases due to band bending as shown in Fig. 2.13(d), causing some electrons to spill over into the bulk STO crystal and get trapped by defects. This leads to a limit to the electrostatic doping of the 2DCG, and the irreversible increase in R_s observed in experiments caused by the loss of carriers into the bulk. If the V_g is restricted to negative values, electrons do not spill over into the bulk as shown in Fig. 2.13(c), and hence the variation of R_s is reversible.

Another effect of this slow escape of carriers over the well at positive values of V_g is a drift of R_s over a time-scale of several hours, which has been observed in (001) as well as (111) oriented LAO/STO.[**31, 80**] However, drift is also known to occur, and in fact be more severe, at more negative values of V_g, which is not explained by the model of Biscaras *et al.*. One way to explain the drift at more negative values of V_g is by noting that

there exist charged defects within the bulk of STO as well as at the interface.[**82**] These charged defects modify the polarization of STO as a function of V_g, which in turn modifies the effect of V_g on the 2DCG. These defects can be thought of as being in a glassy state, moving very slowly under the influence of their mutual long range Coulomb interactions and the applied electric field. The effect of the charged defects can be expected to be stronger at more negative values of V_g where the 2DCG is more depleted, and hence the charged defects near the interface are less screened. This slow drift of R_s also gives rise to hysteresis in R_s as a function of V_g, as will be shown later.

By repeatedly sweeping of V_g over the entire range of V_g used, one can in principle "form" the potential well, or relatively stabilize the carrier density obtained at any given value of V_g due to electrostatic doping. However, one still has to contend with a drift in R_s due to the glassy defects, and the only solution seems to be to wait for a long enough time so that the drift reduces below some acceptable value, before making measurements at a particular value of V_g.

2.4. Contributions to resistivity

A noteworthy feature of transport properties in STO-based 2DCGs is the presence of anisotropies along different in-plane directions. Brinks *et al.* [**83**] observed two-fold anisotropy in their longitudinal resistances in (001) LAO/STO. They attributed it to differences in the scattering of carriers at the edges of atomic terraces, which are ubiquitous features of epitaxial LAO/STO heterostructures, and form as a result of a small out of plane miscut of the STO substrate. This anisotropy was observed to persist up to 300 K, although its magnitude increased at lower temperatures, with the resistance parallel to the

terraces being 10 times smaller than the resistance measured perpendicular to the terraces at $T = 5$ K. Using polarized light microscopy along with scanning SQUID microscopy on (001) LAO/STO, Frenkel *et al.* [**84**] demonstrated that below about 105 K, tetragonal domains form as a result of the structural transition of STO, and current in LAO/STO interfaces flows along the edges of the domains. Resistance measured parallel to the domain edges was observed to be smaller than the resistance measured perpendicular to the domain edges by about a factor of 2 at $T = 4.2$ K, depending on the degree of domain formation. Ma *et al.* [**85**] showed that a particular domain pattern is formed on cooling below ~ 105 K, and persists so long as the temperature is varied below ~ 105 K, which is the tetragonal transition temperature of STO, but that the pattern changes on thermal cycling across 105 K.

An intriguing instance of anisotropic behavior was discovered by Davis *et al.* in (111) oriented samples, associated with mutually perpendicular crystalline directions. In these (111) LAO/STO samples, longitudinal and transverse resistance, capacitance, as well as superconducting properties as a function of T, V_g, and B were found to differ between the in-plane $[1\bar{1}0]$ and $[\bar{1}\bar{1}2]$ crystal directions.[**19, 21, 86**] The anisotropy was tunable; samples annealed in an oxygen environment were found to be more anisotropic than samples annealed in a reducing environment. This anisotropy was not caused due to atomic terraces, since in these samples the terraces were oriented at a 45° angle with respect to the Hall bars used to measure transport properties. The $[1\bar{1}0]$ direction was always found to be more resistive, even after cycling the samples above and below the tetragonal structural transition temperature of STO. Since tetragonal domain formation is a random process not fixed to a particular in-plane crystalline axis, this meant that

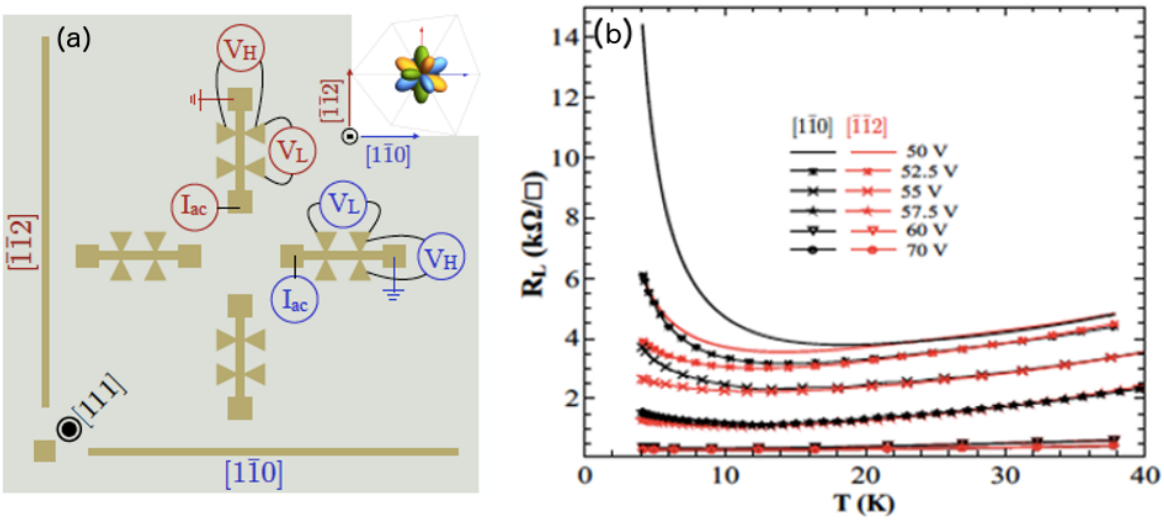

Figure 2.14. **a,** Schematic of the Hall bars used in the work of Davis *et al.* on (111) LAO/STO, showing a 4-probe configuration for the measurement of longitudinal and transverse Hall resistances. The Hall bars are oriented along the [1$\bar{1}$0] and [$\bar{1}\bar{1}$2] crystal directions, are 100 μm wide and 600 μm long. **b,** Sheet resistance vs. T for two perpendicular Hall bars for different values of V_g, showing an onset of anisotropy at $T \sim 20$ K. Images and captions adapted from Ref. [**31**].

the anisotropies were not related to domain formation either. The anisotropic behavior was found to onset strongly at about 20 K, which is below the transition to the quantum paraelectric phase of STO, and not in the vicinity of any known structural transition of STO. One explanation for the observed anisotropies was the formation of an electronic nematic phase, similar to what is seen in some pnictide superconductors and topological superconductors.[**31**] The question remains as to what in the electronic properties of (111) oriented LAO/STO leads to this surprising behavior.

For STO-based 2DCGs, typically, at low temperatures, R_s can easily increase by a factor of over 10 when V_g is changed from positive values to negative values (typically a few tens of Volts to hundreds of Volts, both positive and negative), as can be seen from

Fig. 2.13(e). In contrast, the Hall coefficient $R_H = -1/ne$, where n is the carrier density, usually changes only by less than a factor of 5.[**31, 87, 88**] Although the details of the analysis of Hall data can vary depending on the model used, as we shall discuss later, this variation in R_H suggests that the change in resistance as a function of V_g is a result of a large change in carrier mobilities, which depend on scattering time τ and effective mass m^* as $\mu = e\tau/m^*$, rather than a change in carrier densities. This trend in R_s and R_H is a common feature of STO-based 2DCGs.[**10, 15, 18**]

For STO-based 2DCGs in general, R_s is known to show a minimum at a temperature of a few Kelvin. At lower temperatures, R_s can continue to increase,[**19**] saturate,[**11, 15**] or even vanish if the sample undergoes a superconducting transition,[**9**] depending on growth conditions and the particular value of V_g. Thus, the band structure details and scattering mechanisms that lead to the aforementioned drastic changes in R_s as a function of V_g, are amplified at lower values of T. Transport measurements at these low temperatures can be used to distinguish between various scattering mechanisms and processes in the system. Hence I next explore the various potential causes of the drastic change in μ, or equivalently, in τ, by discussing the low temperature contributions to sample resistance in STO-based 2DCGs as a function of T and B. Here I note that I will be using the symbol B to stand for magnetic field perpendicular to the 2DCG.

2.4.1. Magnetic field independent contributions

2.4.1.1. Drude contribution, R_0. For metallic systems in the weak disorder limit, transport is traditionally described by the semiclassical approximation, in which the electrons are treated classically, as a distribution of particles with particular positions $\mathbf{r}$ and momenta $\mathbf{p}$ at a given time t, while scattering between electrons and randomly distributed

impurities is treated quantum mechanically.[**89**] The linearized Boltzmann equation in the presence of an electric field **E** and a magnetic field **B**, which describes the deviations of the distribution function from equilibrium, δf, is written as:[**89**]

$$\frac{\partial \delta f}{\partial t} - \frac{e}{\hbar c}\mathbf{v} \times \mathbf{B} \cdot \frac{\partial \delta f}{\partial \mathbf{k}} - \mathbf{v} \cdot e\mathbf{E}\frac{\partial f^0}{\partial E} = \mathcal{I}_{coll}. \tag{2.1}$$

Here $f^0(\mathbf{r}, \mathbf{p}, t)$ is the equilibrium particle distribution function, E is the energy, and $\mathcal{I}_{coll}$ is the collision term. In the simplest case, we can consider a zero magnetic field, a dc electric field, and use the relaxation time approximation $\mathcal{I}_{coll} = -\delta f/\tau$, where τ is the transport scattering time, in order to find δf. This can be used to calculate the current density in the direction α in the system as:

$$j^\alpha(\mathbf{r}, t) = -2e \int \frac{d^3k}{8\pi^3} \delta f v^\alpha. \tag{2.2}$$

From this, one can calculate the sample conductivity to be $\sigma = ne^2\tau/m^*$, which is known as the Drude conductivity. In 2D systems, in which conductivity is the same as conductance, the Drude resistance can be written as $R_0 = m^*/ne^2\tau$. If contributions due to other mechanisms are small compared to the sheet resistance R_s, then R_s can be approximated as R_0 for the purpose of determining τ. If these other contributions are also independent of each other, they can be considered additive for the purpose of analysis. However, in a real system where other contributions are substantial and difficult to pry apart, it is unclear that the measurement of R_s at any given temperature gives us the value of R_0. In the case of STO-based 2DCGs, this is especially a problem in case of

measurements at lower values of V_g, for which resistance changes rapidly as a function of T at the low temperatures of interest (see Fig. 2.14(b)), and the Drude contribution may not apply.

The effective carrier mass m^* is typically obtained from ARPES measurements. ARPES studies on vacuum cleaved (111) STO have revealed highly anisotropic effective masses of electrons from the Ti $3d$ t_{2g} orbitals of interest, as discussed before.[**25**] An estimate for m^* can also be obtained from an analysis of Shubnikov-de Haas (SdH) data,[**91**] to be discussed later. The sheet carrier density n is estimated using Hall data. Hall data in STO-based interfaces are electron-like, and show nonlinear behavior, especially at higher values of V_g.[**91, 74**] This has been interpreted as evidence of multicarrier transport, which complicates the determination of n and hence, of τ. This in turn introduces uncertainty in the straightforward estimation of other transport parameters, namely, the Fermi wavenumber $k_F = \sqrt{2\pi n}$, Fermi velocity $v_F = \hbar k_F/m^*$, mean free path l, and the diffusion constant $D = v_F l/2$ for two dimensional systems. It is also possible to use SdH data to estimate n, however, experiments in STO-based 2DCGs have consistently shown the estimated n from SdH data to be smaller than the n estimated from Hall data by a factor of five to ten.[**91, 93**] This discrepancy will be discussed later, here I only note that getting a reliable estimate of n in these systems has been elusive.

2.4.1.2. Contributions due to phonon scattering, $\Delta R_{ph}(T)$. For a more complete picture of the scattering processes, one can go beyond the relaxation time approximation, and estimate $\mathcal{I}_{coll}$ and equivalently, the scattering time for the scattering of Bloch wave functions off quasiparticles such as phonons. In this case, one typically finds the scattering time increases with temperature according to the relation $\tau_p \propto T^{-p}$, where p depends

on the particular scattering mechanism.[**94**] The contribution to sample resistance due to these inelastic scattering processes then increases as $\Delta R_{ph} \propto T^p$. The electron-phonon contribution is proportional to T^5 in the clean limit in the case of simple isotropic metals, which is known as the Bloch-Grüneisen law.[**89**] It is proportional to T^3 if Umklapp scattering is dominant,[**95**] which happens either at higher temperatures or when the Fermi surface intersects the Brillouin zone. Other powers are also possible for scattering off other kinds of quasiparticles, such as magnons and polarons.[**96**] In STO-based systems, many experiments have identified a T^2 dependence of R_s,[**97, 98, 99**] attributed to phonon-mediated electron-electron scattering, or electron-electron scattering in the presence of multiple bands. Here I note that these contributions are not expected to play a role in the sub-liquid Helium temperature range under study in this thesis, since these scattering mechanisms are frozen out to a large extent at very low temperatures.

2.4.1.3. Contributions due to charged impurities, $\Delta R_{ion}(T)$. Charged impurities such as oxygen vacancies are a common defect in STO as discussed earlier. These occur due to the removal of neutral oxygen atoms from the crystal, leaving behind two electrons in the crystal. Near the interface, these oxygen vacancies form donor levels just below the conduction band of the system. The electrons initially associated with the O ions can be excited into the conduction band if the temperature is high enough, and participate in transport. However, as T is reduced, electrons can drop back into the donor level, in effect being trapped by the oxygen vacancy sites. As discussed in the previous section, these charge traps near the interface are known to have activation temperatures T_A ranging from a few Kelvin to a few tens of Kelvins.[**20**] The concentration of the trapped charges decreases exponentially with increasing temperature on the scale of T_A. Also, the screening

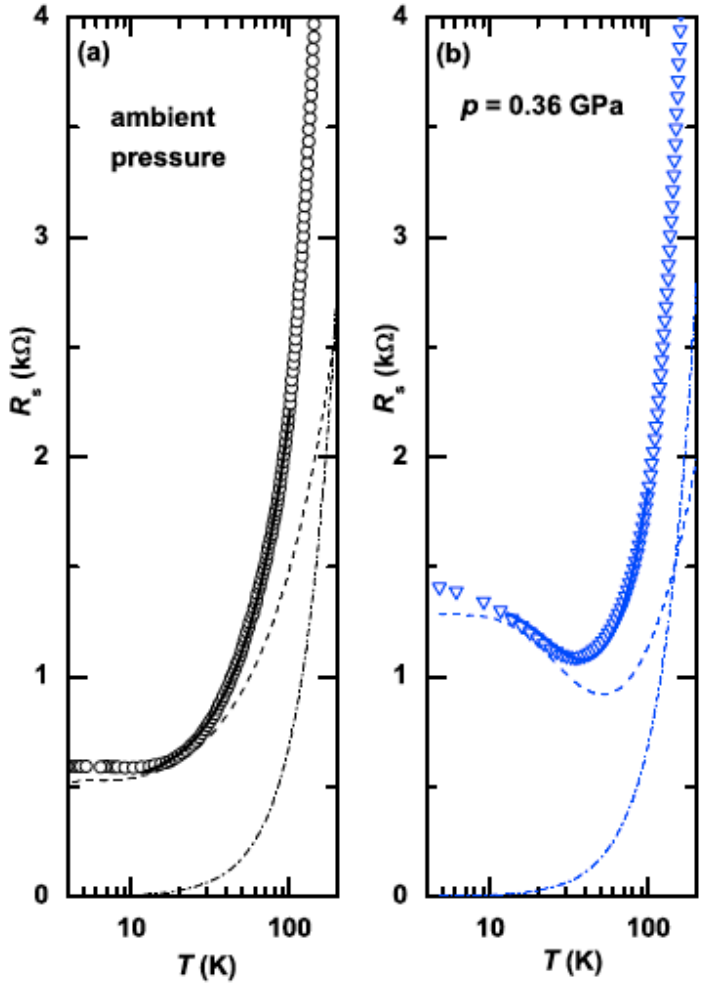

Figure 2.15. R_s vs. T for a (001) LAO/STO sample at **a,**ambient pressure, **b,** at a pressure of 0.36 GPa. The dashed-dotted lines are a contribution due to phonon mediated electron-electron inelastic scattering, $\Delta R_{in} \propto T^2$, and the dashed lines are a contribution due to ΔR_{ion}. The solid lines are a fit which takes into account both these contributions. Image from Ref. [**97**].

of these defects decreases with increasing temperature, since the dielectric permittivity of STO, which is also a function of V_g, decreases with increasing temperature.[**100**] Scattering of electrons off these partially screened charged impurities leads to the contribution $\Delta R_{ion}(T)$, which when combined with the change in resistivity caused by the inelastic

mechanisms described in the previous paragraph, can lead to the resistance minimum at intermediate temperatures, with low temperature saturation, that is commonly observed in STO-based 2DCGs.[**97**] This mechanism may be present in combination with magnetic scattering at Kondo impurities, which is typically used in order to describe the observed resistance minimum in these systems,[**11, 101**] and which will be discussed later.

2.4.2. Magnetic field dependent contributions

2.4.2.1. Classical orbital contributions, $\Delta R_{cl}(T, B)$. One effect of the magnetic field is to cause carrier paths to curve perpendicular to the direction of the field, which leads to a transverse electric field and the observation of Hall resistance, and may also lead to a positive longitudinal MR. The size of these effects depends on the direction and magnitude of B, the types of carriers present, as well as the band structure and sample inhomogeneities.

For a single type of carrier with a spherical Fermi surface involved in transport, the Hall resistance as a function of B is linear with a slope independent of B, given by $R_H = -1/ne$.[**89**] R_H is negative or positive depending on whether the carriers are holes or electrons. The longitudinal MR contribution $\Delta R_{cl}(B)$ for this simple system turns out to be zero, as the effect of B in causing carrier paths to curve is exactly canceled out by the effect of the transverse electric field caused by B. However, in real metals which may have a distribution of scattering times or an anisotropic Fermi surface, $\Delta R_{cl}(B)$ is non-zero, albeit small, and for small fields ($\omega_c\tau < 1$, where $\omega_c = eB/m^*$) is proportional to $(\mu B)^2$, or $(\omega_c\tau)^2$. In large fields ($\omega_c\tau > 1$), the ability of the field to increase the

number of scattering events saturates, and hence $\Delta R_{cl}(B)$ also saturates in the limit of large fields, in case of closed orbits. In case of open orbits it can grow without limits.[**89**]

In STO-based 2DCGs, the Fermi level can cross multiple bands, as we have seen in the earlier discussion. Magnetotransport in these systems is typically analyzed on the basis of a two-band model for simplicity.[**91, 74**] This is a good approximation in the case of (001) systems since some of the the carriers involved in transport come from the low energy d_{xy} band, while some come from the $d_{yz,zx}$ bands, which are degenerate if one ignores ASO. In the (111) case also this is valid since some carriers come from a_{1g} band while others come from the e'_g doublet. In this model, which assumes no interband scattering, and carrier mobilities independent of field, R_H and the classical contributions to longitudinal MR ($R_{cl}(B)$) are given by the following expressions: [**89**]

$$R_H = \frac{R_1\rho_2^2 + R_2\rho_1^2 + R_1R_2(R_1+R_2)B^2}{(\rho_1+\rho_2)^2 + (R_1+R_2)^2B^2} \tag{2.3}$$

$$R_{cl}(B) = \frac{\rho_1\rho_2(\rho_1+\rho_2) + (\rho_1R_2^2 + \rho_2R_1^2)B^2}{(\rho_1+\rho_2)^2 + (R_1+R_2)^2B^2} \tag{2.4}$$

Here $R_{1,2} = -1/n_{1,2}e$ are the Hall coefficients, while $\rho_{1,2} = 1/n_{1,2}e\mu_{1,2}$ are the resistivities for carriers with densities n_1 and n_2 and mobilities μ_1 and μ_2. Then $\Delta R_{cl}(T,B) = R_{cl}(T,B) - R_{cl}(T,0)$. We see that in the two-band model R_H acquires a field dependence. The zero field value of R_H depends on both carrier densities and mobilities, and is dominated by the density of the high mobility carriers if one type of carrier has a

much higher mobility than the other. The value at high fields, i.e., $B \to \infty$, depends only on the total carrier density as $R_H = -1/(n_1 + n_2)e$. The MR increases at small fields as B^2, similar to the single-band case, except that the values of the MR can be quite large depending on the carrier densities and mobilities. For large fields, in case of conductors with closed Fermi surfaces and only electron-like or only hole-like carriers, the MR saturates. The presence of open orbits, or the simultaneous presence of electron and hole-like carriers,[**89**] or a broad distribution of carrier mobilities in disordered samples [**90**] can lead to a non-saturating, quasilinear variation of MR, as is often observed in STO-based 2DCGs.[**91, 74**] In some topological materials such as WTe_2, strong SOI has been speculated to cause anomalously large MR, by protecting against backscatterings in the absence of external field. Applying a B field removes this protection due to strong SOI against backscattering, which leads to a large MR.[**92**]

Many experiments have shown a transition from a linear Hall response to a non-linear Hall response, along with a simultaneous increase in the longitudinal MR signal, as V_g is increased, or equivalently, as electron-like carriers are added to the 2DCG.[**91, 74**] As shown in Fig. 2.16(a), for their (001) LAO/STO samples, Joshua *et al.* [**74**] saw a nonlinear Hall signal and a large, positive, almost quadratic MR for $V_g > 40$ V, and a linear Hall signal along with a very small, negative longitudinal MR signal for $V_g < 40$ V. They interpreted this change in behavior as a change from single band transport below 40 V, to multi-band transport above 40 V, on the basis of the discussion presented above. In their picture, in the single band regime, only the high mobility, low energy d_{xy} band was occupied, R_H was independent of B, and the magnitude of $R_H = -1/ne$ increased with increasing V_g as expected. Above $V_g = 40$ V, the d_{yz} and d_{zx} bands began to be

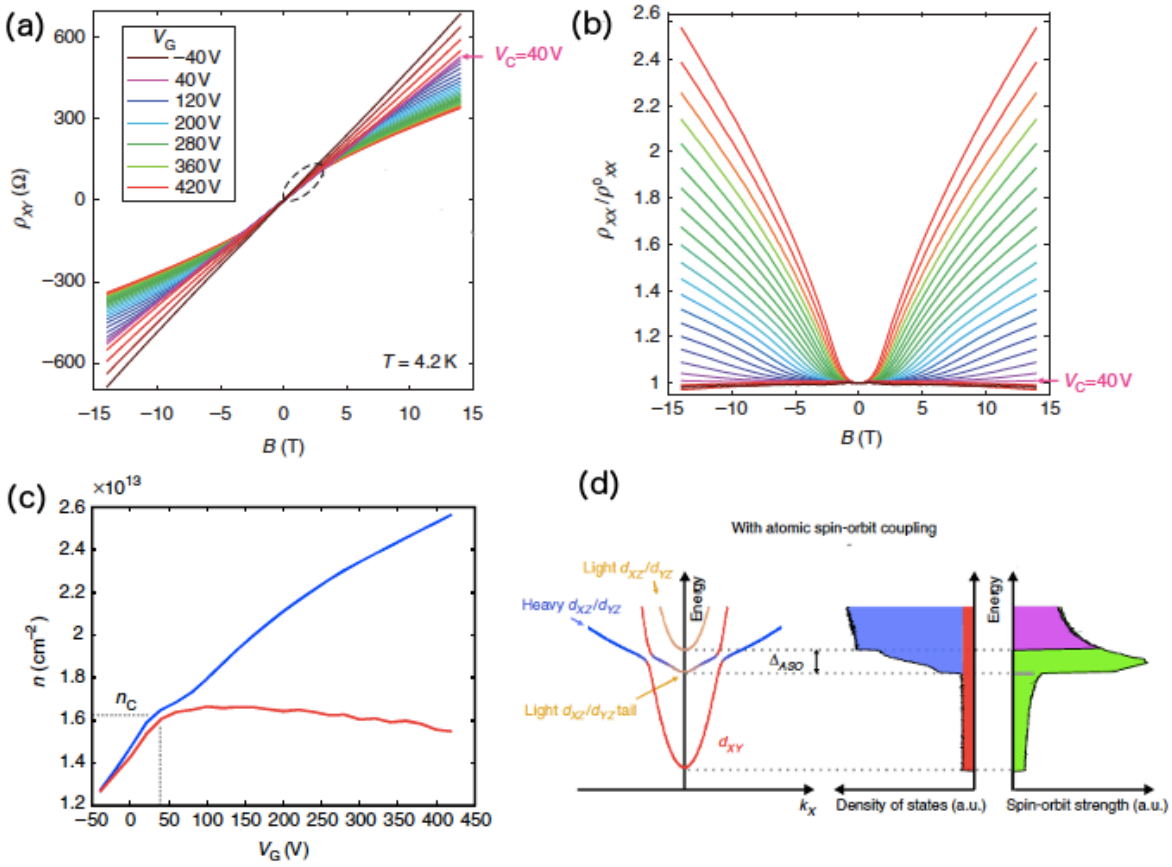

Figure 2.16. **a,** Hall resistance of a (001) LAO/STO sample as a function of B for different values of V_g, at $T = 4.2$ K, showing nonlinear behavior for $V_g > 40$ V and linear behavior for $V_g < 40$ V. **b,** Longitudinal resistance, normalized to its zero field value, decreases as as V_g is reduced, and becomes very small below $V_g = 40$ V, signifying a transition from multicarrier to single carrier transport. **c,** Density of high mobility carriers (red trace) as a function of V_g, calculated from the zero field slope of the Hall data in Fig. 2.16(a). Above $V_g = 40$ V, the Lifshitz transition occurs and electrons are preferentially added to the low mobility $d_{yz,zx}$ bands, hence the density of the high mobility d_{xy} carrier (n_{hi}) saturates and the total density of carriers (n_t) continues to grow, so that the density of the low mobility carriers is given as $n_t - n_{hi}$. The fall-off in n_{hi} at higher values of V_g occurs because the model of Joshua *et al.* is only valid near the Lifshitz transition. **d,** Band diagram near the Γ point of the (001) LAO/STO 2DCG, showing the effect of ASO on the otherwise degenerate d_{yz} and d_{zx} bands. The model predicts a sharp increase in SOI at the Lifshitz transition. Also shown is the DOS and strength of SOI as a function of energy, or equivalently, band filling or V_g. Images and captions adapted from Ref. [**74**].

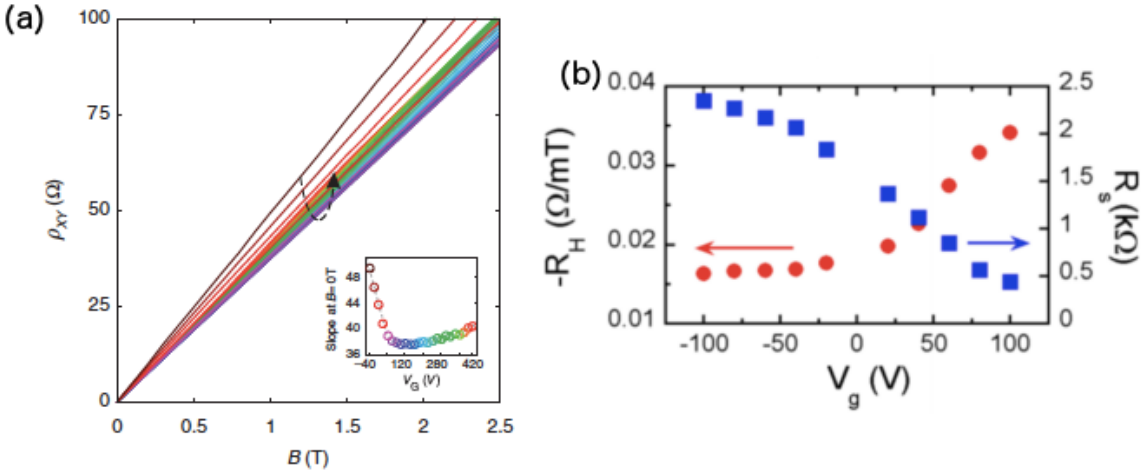

Figure 2.17. **a,** Same Hall data as in Fig. 2.15(a), at fields < 2.5 T (Inset: Variation of the zero-field Hall slope as a function of V_g. Images and captions adapted from Ref. [**74**]. **b,** Variation of zero-field Hall slope and R_s as a function of V_g in a different (001) LAO/STO sample. Images and captions adapted from Ref. [**15**]. Note that the values of R_H in Fig. 2.16(a) first decrease and then slightly increase as V_g is increased, while the values of R_H in Fig. 2.16(b) increase throughout the range of increasing V_g.

preferentially occupied since they have a larger density of states (DOS) owing to a larger in-plane effective mass (see Fig. 2.16(d)), and hence the density of the high mobility d_{xy} carriers saturated. This was described as the so-called Lifshitz transition.[**102**] The density of high-mobility carriers was obtained from the zero-field values of R_H, which is a valid assumption if the mobility of d_{xy} carriers is much greater than the mobility of the d_{yz} and d_{zx} carriers as discussed earlier, whereas the high-field values of R_H gave the total density of carriers, as shown in Fig. 2.16(c). Their model predicted a non-monotonic variation in the SOI with V_g owing to the effects of ASO being strongest near the bottom of the d_{yz} and d_{zx} bands, as shown in Fig. 2.16(d).

Although this picture appears to be quite comprehensive, there are certain problems. The slight increase in the magnitude of the zero-field R_H seen above $V_g = 40$ V (Fig.

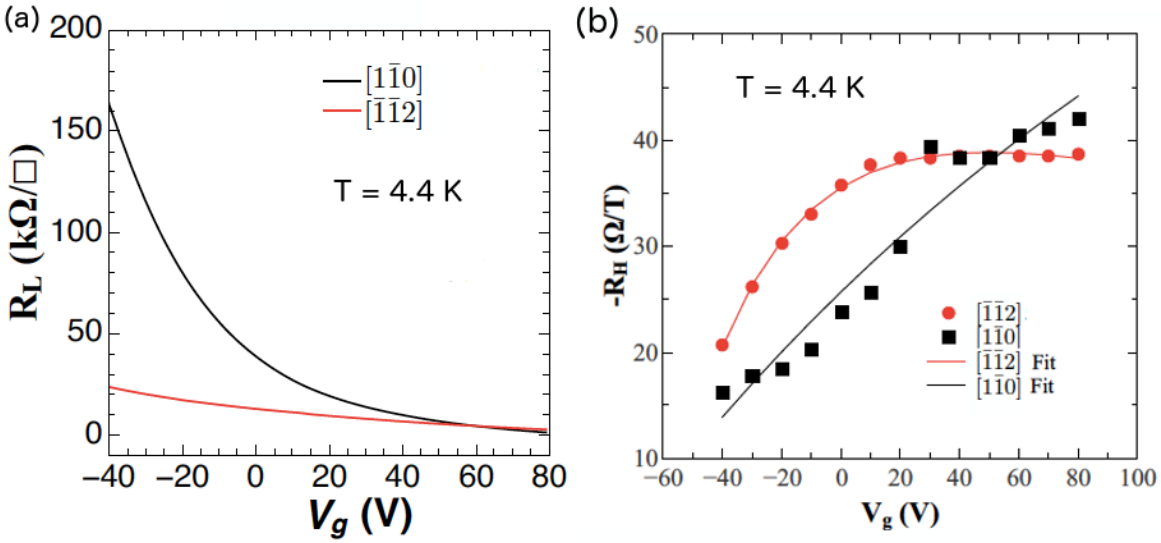

Figure 2.18. **a,** Sheet resistance averaged over forward and reverse sweeps of V_g for two Hall bars oriented along mutually perpendicular in-plane directions of (111) oriented LAO/STO, showing anisotropic behavior. **b,** Variation of zero-field Hall slope as a function of V_g for a (111) oriented LAO/STO sample. Note the sharp decrease in R_H for the (111)-oriented sample below $V_g \simeq 20$ V, as well as the anisotropy associated with the in-plane crystal directions. Images and captions adapted from Ref. [**31**].

2.17(a)) seems to indicate that the concentration of the high mobility electrons *decreases* with increasing V_g, which is unphysical. This was not explained by this model. Interestingly, most (001) LAO/STO samples reported in the literature, for example, see Fig. 2.17(b), seem to lie within the regime where the zero-field Hall coefficients show an increase in magnitude with V_g, which according to the model of Joshua *et al.* means multiple bands are occupied, even at the lowest values of V_g investigated. Nevertheless, SOI strength is observed to increase with V_g,[**18**] according to analyses based on weak anti-localization (to be discussed later), as opposed to the nonlinear trend in SOI predicted by Joshua *et al.*'s model.

The unexpected increase in the magnitude of R_H with increasing V_g is even more startling in (111) oriented LAO/STO, as shown in Fig. 2.18. The magnitude of R_H *decreases*, or n increases, as V_g is decreased, even in the regime of negative V_g, where R_s sharply increases. Davis *et al.* [**31**] showed that this variation cannot be reconciled by a purely electron-like carrier transport model, and implies the presence of hole-like carriers is important, especially at lower values of V_g. Note that their Hall data also reflected the anisotropy seen in their sheet resistance data for Hall bars oriented in the mutually perpendicular in-plane crystal directions.

2.4.2.2. Effect of Landau quantization, $\Delta R_{SdH}(T, B)$. As the field is increased, the 2DCG evolves from the classical regime described above into the quantum regime. At high enough fields ($\omega_c\tau = \mu B > 1$, where μ is the carrier mobility) and low enough temperatures, quantization of the circular motion of carriers under the action of the field becomes important. The uniform density of states of the 2DCG splits into Landau levels, which start to play a role in transport when their energy spacing becomes comparable to the temperature ($\hbar\omega_c > k_B T$). As the field is increased, the Fermi energy moves across individual Landau levels, causing increased scattering and hence jumps in the MR. The jumps or oscillations are periodic in $1/B$, with a frequency inversely proportional to extremal areas of the Fermi surface perpendicular to B, and hence to the carrier density due to that particular Fermi surface.[**89**] Thus multiple frequencies in the oscillations are indicative of either multiple pockets of the Fermi surface, nested or separated in k-space, or of anisotropic Fermi surfaces which have multiple extremal areas. The amplitude of these SdH oscillations increases with increasing field, and also depends on the effective masses of carriers and their scattering times. These dependencies for a single Fermi surface with

a single extremal area are captured in the Lifshitz-Kosevich formula for the oscillation amplitude $\Delta R_{SdH}(T,B)$:[**103**]

$$\Delta R_{SdH}(T,B) = 4R_0 \times \exp\Big(-\frac{2\pi^2 k_B m^* T_D}{\hbar e B}\Big)\frac{\frac{2\pi^2 k_B m^* T}{\hbar e B}}{\sinh(\frac{2\pi^2 k_B m^* T}{\hbar e B})}\sin\Big[2\pi\Big(\frac{F}{B}-\frac{1}{2}\Big)+\phi\Big] \tag{2.5}$$

Here R_0 is the non-oscillating part of the resistance, $T_D = k_B\hbar/2\pi\tau_D$ is the Dingle temperature, with τ_D being the Dingle scattering time. The Dingle temperature captures the effect of the broadening of Landau levels due to scattering. The oscillation frequency F was determined by Onsager to be inversely proportional to an extremal area of the Fermi surface, which is proportional to $k_F^2 \sim n$, where k_F is the Fermi wave number and n is the areal carrier density. F is given as $hn/N_s e$ where N_s the spin degeneracy.[**103**]

SdH oscillations have been observed in (001) LAO/STO for samples grown under a variety of conditions, and depending on carrier mobilities, they set in at fields of a few Tesla. It is possible to get a vast amount of information from SdH oscillations, and in samples with high carrier mobilities and a large enough available field scale, they have been analyzed in terms of multiple bands, as well as single bands split by Rashba SOI.[**91, 104**] However, the analysis can be complicated by the presence of a large positive quadratic or quasilinear background contribution for high mobility samples, especially in the regime of high V_g, as is often observed in STO-based 2DCGs. SdH oscillations have not so far been observed in (111) oriented STO-based 2DCGs. The carrier densities obtained using SdH data in STO-based 2DCGs have been consistently found to be smaller than those estimated using Hall data by a factor of five to ten. This is usually attributed to not

accounting for different band degeneracies correctly, or the oscillations associated with low mobility carriers not being sufficiently resolved at the available field scales.

2.4.2.3. Contributions due to magnetic scattering $\Delta R_{mag}(T, B)$. In many STO-based 2DCGs, going from higher to lower values of V_g, the size of $\Delta R_{cl}(B)$ is observed to reduce considerably, and in some cases a negative MR emerges at the lowest values of V_g.[**74**] This MR is seen to remain negative even at the highest values of B studied. One of the causes of negative MR is the presence of magnetic scattering in the system.

Evidence of magnetism in (001) LAO/STO was first observed by Brinkman *et al.* in 2007.[**11**] For LAO/STO grown at an oxygen partial pressure (P_{O_2}) of 10^{-3} Torr, they observed a minimum in the resistance vs. T curve which they attributed to the Kondo effect. They also saw a negative magnetoresistance, and hysteretic behavior indicative of ferromagnetism at $T = 300$ mK. This was a surprising finding since neither of the constituent materials show magnetic behavior. Since then, experimental probes have shown a variety of magnetic phenomena in LAO/STO. Many experiments revealed the presence of a negative MR and Kondo minimum similar to Brinkman's findings.[**101**] SQUID magnetometry measurements by Ariando *et al.* [**16**] on a sample grown at $P_{O_2} = 10^{-2}$ Torr showed electronic phase separation into a ferromagnetic phase, which persisted above room temperature, and a diamagnetic/paramagnetic phase, which appeared below 60 K, at the LAO/STO interface. Scanning SQUID magnetometry measurements by Bert *et al.* [**14**] revealed patches of ferromagnetic order, a few microns in size, in LAO/STO samples which were grown at a lower P_{O_2}, but were annealed post growth in 0.4 bars of oxygen. Patches smaller in size could have been obscured by the 3 μm size of their

SQUID loop. They found that the magnetism was in-plane, and also observed it in SrO-terminated LAO/STO heterostructures, but not in LAO/STO heterostructures with less than 4 unit cells of LAO. The inhomogenous magnetism was found to persist up to 4.2 K, which was the limit of their measurement setup. Cantilever based torque magnetometry measurements by Li *et al.* [**13**] found evidence of in-plane magnetism which persisted up to 200 K, in LAO/STO samples which were grown and post-growth annealed in similar conditions as Bert's samples. X-ray magnetic circular dichroism and x-ray absorption spectroscopy at $T = 10$ K on similar samples showed that ferromagnetism was in-plane, in accordance with earlier measurements. Simulations of the spectra showed that magnetism originated mainly from the d_{xy} bands of Ti^{3+} ions, which were shown to be present at the interface.[**68**] Scanning force microscopy measurements by Bi *et al.* [**12**] found that LAO/STO samples which were tuned to be highly depleted of carriers using V_g showed inhomogenous ferromagnetic patches that could be tuned by V_g, and persisted up to room temperature. All these experiments were done on samples which were either grown in comparatively higher oxygen partial pressures, or were depleted of carriers using V_g.

Hysteretic MR, which can indicate ferromagnetic order in conductors, has also been observed in (001) oriented LAO/STO heterostructures, as shown in Fig. 2.19(a). This hysteretic MR was found to persist over a large range of V_g, occurred at millikelvin temperatures, and in certain cases was found to co-exist with superconductivity.[**15, 105**]

A few groups have observed anisotropy in resistance as a function of the angle between current and in-plane field.[**106, 107**] In these studies, the anisotropy was observed to become stronger at more positive values of V_g, leading to the conjecture that the electrons in the d_{yz}, and d_{zx} bands participate in this behavior in case of (001) STO-based 2DCGs.

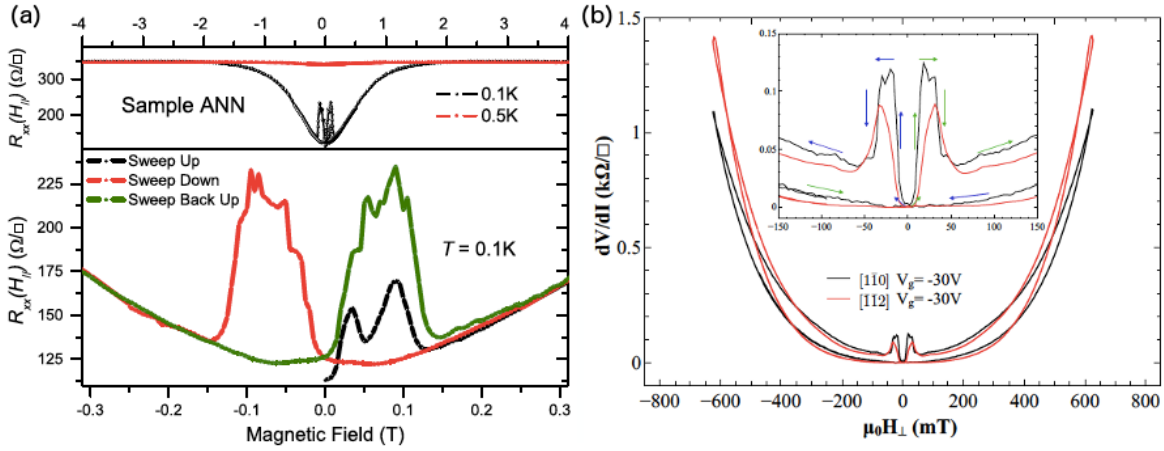

Figure 2.19. **a,** Hysteretic MR in (001) LAO/STO. Image from Ref. [**105**].**b,** MR in (111) LAO/STO in a Hall bar oriented along the $[\bar{1}\bar{1}2]$ direction, for different values of V_g. The sweep direction is from negative to positive fields. Image from Ref. [**10**].

However, there is some confusion whether the observed anisotropy is due to the standard anisotropic magnetoresistance (AMR) found in ferromagnetic materials, since they did not find any evidence of hysteresis in their measurements. Recently, Pai *et al.* [**108**] have theorized that these anisotropies can be attributed to the combination of band structure effects, SOI and EEI, and not to ferromagnetic interactions.

The limited amount of data available on (111) LAO/STO has revealed hysteretic MR at millikelvin temperatures, coexisting with superconductivity, that persists when V_g is used to tune the system into a non-superconducting state,[**10**], as shown in Fig. 2.19(b). Six-fold anisotropy in MR similar to that described above has also been observed, and related to the hexagonal crystal symmetry of the (111) system.[**26**]

Ruhman *et al.* [**75**] put forward an explanation for the variety of observed magnetic phases in (001) LAO/STO-based on the different interactions between itinerant d_{xy}, d_{yz}, and d_{zx} electrons and the localized moments, which were also assumed to be of d_{xy}

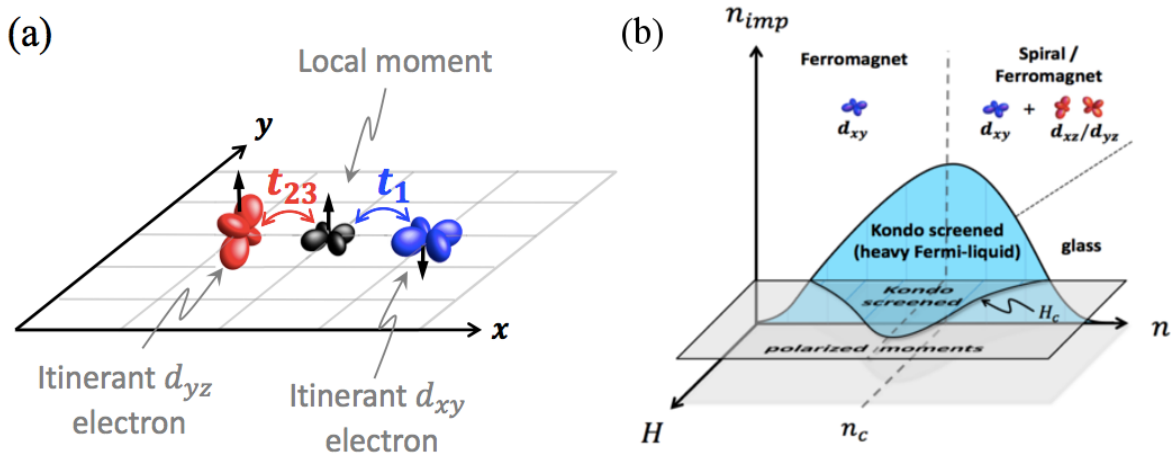

Figure 2.20. **a,** Schematic representation of the virtual hopping processes between localized and itinerant electronic states. The local moments (black) are taken to be of d_{xy} symmetry and the itinerant electrons can be of either d_{xy} (blue) or d_{xz}/d_{yz} (red) symmetry. Hopping between the d_{xy} itinerant electron and a d_{xy} localized state with amplitudet_1 and hopping between the itinerant d_{xz}/d_{yz} electron and the unoccupied d_{xz}/d_{yz} state on the moment site with amplitude t_{23}. Note that the local-moment electron can also hop out of the impurity site to the d_{xy} conduction band with amplitude t_1. **b,** Schematic phase diagram of the magnetic phases in the LAO/STO interface in the space of itinerant electron density n, local magnetic moment density n_{imp}, and magnetic field H. The dashed linemarks the critical density n_c above which $d_{xz/dyz}$ itinerant electrons are present in the system. Image and caption from Ref. [**75**]

character. According to their theory, magnetic behavior of the system, ranging from ferromagnetic to Kondo-like to spin-glass-like, depends on the relative as well as absolute concentrations of localized moments and itinerant electrons, and has been summarized in Fig. 2.20. Some theories predict that the observed ferromagnetism can be explained within the Stoner model applied to the d orbitals of Ti ions in regions rich in oxygen vacancies, which may cause the two neighboring Ti ions to acquire parallel magnetic moments, as discussed earlier.[**109**] Banerjee *et al.* [**52**] predicted that exchange interactions between the d_{xy} moments mediated by itinerant electrons in the presence of strong SOI

would give rise to a Dzyaloshinskii-Moriya interaction and a spiral magnetic order. However, there is no theoretical explanation yet about the origins of magnetic behavior in (111) oriented STO-based 2DCGs.

Thus we see that STO-based 2DCGs are known to show a wide range of magnetic phenomena, ranging from Kondo-like behavior caused by dilute magnetic scatterers in the system, to spin glasses, to a full ferromagnetic phase at the highest concentration of magnetic scatterers.[**75**] What is more, these three regimes may coexist in the 2DCG owing to a disordered distribution of magnetic scatterers. For all these regimes, however, a negative isotropic MR has been predicted and observed in many systems including STO-based 2DCGs.[**110, 111, 11**] This negative contribution to the MR, $\Delta R_{mag}(T, B)$, which can be large, is proportional to B^2 for smaller fields, and saturates at higher fields greater than those required to saturate the magnetic moments. If the magnetization of the system is hysteretic, as it is in ferromagnetic systems and can be in spin-glass systems, then the hysteresis is also reflected in the MR of the system.

The temperature dependence of resistivity due to the presence of magnetic scatterers depends on the whether the magnetic moments are in the dilute Kondo limit, in the spin glass regime, or in the ferromagnetic regime. In both situations the resistivity increases logarithmically as temperature is decreased, as conduction electrons scatter off partially screened magnetic moments. If the temperature is lowered below the characteristic Kondo temperature of the system, the moments are fully screened, and a saturation in resistance is observed. If, however, the concentration of magnetic moments is high, and if the temperature is low enough that the thermal energy is smaller than the strength of

interaction between individual magnetic moments, the moments start to freeze out, leading to a spin-glass phase, wherein the sample resistance can even decrease as temperature is lowered.[**112**] Depending on the relative numbers of itinerant carriers and magnetic impurities, as well as the couplings between them, this freeze-out of moments can occur before or after the moments are fully screened. Thus the presence of magnetic moments in STO-based 2DCGs can be invoked to explain some of the observed T and B dependencies in this system.

It was discussed earlier that scattering of conduction electrons off ionic impurities can give a similar temperature dependence as the scattering of conduction electrons off magnetic moments.[**97**] In principle, it should be possible to tell these two mechanisms apart by measuring the temperature dependence of resistance while applying a magnetic field. $\Delta R_{ion}(T)$ should remain unaffected by B, while in the case of $\Delta R_{mag}(T, B)$, the resistance minimum and low temperature saturation should progressively disappear for higher values of B. However, the presence of localization corrections and EEI corrections (to be discussed later) also can give rise to a difference in the temperature dependence of resistivity for different values of B. Another way would be to look for a peak in specific heat of the sample near the estimated Kondo temperature, however, to my knowledge, this technique has not been used so far in the case of STO-based 2DCGs.

2.4.2.4. Single-particle localization contributions, $\Delta R_{loc}(T, B)$. We discussed earlier that in the clean limit the effect of crystal defects on transport are captured by the Boltzmann equation. The situation is different if disorder is strong, i.e., $k_F l < 1$ or equivalently, $R > R_Q = 25.812$ k$\Omega/\square$, which is the quantum of resistance. In this case, the diffusive approximation does not work, as electron wave functions can no longer be

considered as plane waves, but as wave packets decaying exponentially in space. In two dimensions in the presence of disorder, and in the absence of SOI, Anderson predicted that all electronic states are localized at zero temperature.[**72**] For strong disorder, $\Delta R_{loc}(T, B)$ increases exponentially as T decreases.[**94**]

In the regime of intermediate disorder, the predictions of the weak localization theory, which assumes a diffusive system and employs perturbative techniques to derive single-particle corrections to the conductivity resulting from the constructive interference of coherently back-scattered carriers, are valid.[**113**] Corrections to the conductivity such as the one denoted by the Langer-Neal graph,[**114**] are calculated using the Kubo formalism. This graph, shown in Fig. 2.21(a), denotes a particle in an initial state **k** scattering into a final state **-k**, via two complementary series of states. The real space representation is shown in Fig. 2.21(b), where a carrier returns to its original position after a series of random scattering events. Another particle traveling the time reversed path without any stochastic scattering, would collect the same phase, and interfere constructively with it, leading to an increased probability of back-scattering, as shown in Fig. 2.21(c). In two dimensions, weak localization leads to an increase in resistance as T is reduced as given by Eqn. 2.6:[**94**]

$$\Delta R_{loc}(T, 0) = -\frac{R_0^2}{2\pi^2\hbar/e^2}\, p \ln\frac{T}{T_0} \tag{2.6}$$

where $T_0 = \hbar/k_B\tau$. The effect is caused by an increase in the phase coherence time τ_ϕ or equivalently, phase coherence length l_ϕ with decreasing temperature, which typically goes as T^{-p},[**94**] where p depends on the mechanism of decoherence. An applied magnetic field

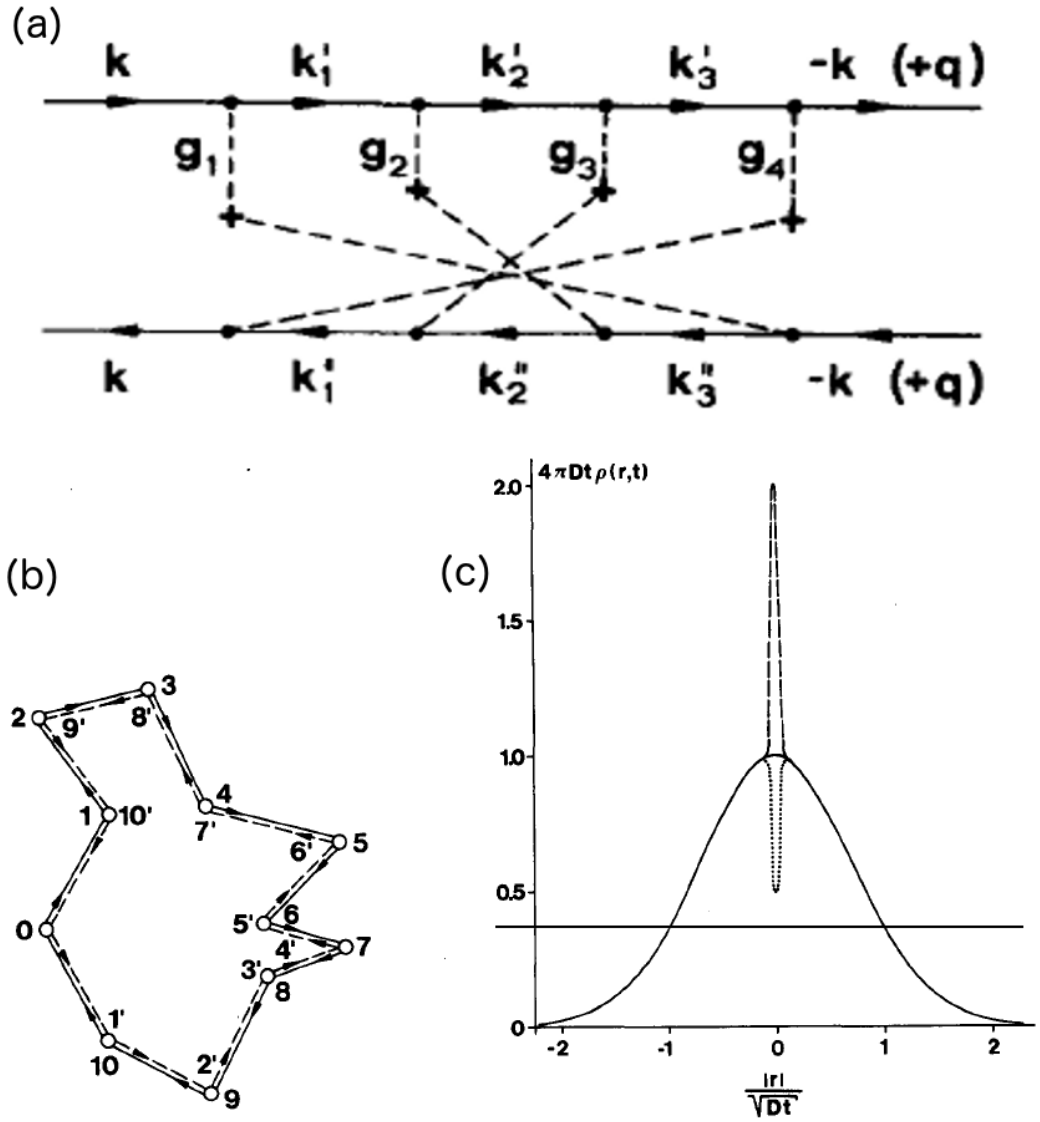

Figure 2.21. **a,** Langer-Neal diagram, showing the scattering of state **k** into state **-k** by two complementary paths: k'_1, k'_2, k'_3 and k''_1, k''_2, k''_3. **b,** Diffusion paths traversed corresponding to Fig. 2.21(a). **c,** Probability distribution of a diffusing electron which starts at $r = 0$ at time $t = 0$. The probability of returning to the origin is twice as great in the case of quantum diffusion without strong SOI (dashed line), as in the case of classical diffusion (solid line). In case SOI is present, the probability in the case of quantum diffusion is halved (dotted curve). Image from Ref. [**113**].

perpendicular to the 2DCG also impedes the coherent interference of the backscattered electron waves, and leads to a MR. This effect can be understood as follows: In a 2D system, in the absence of a B field, time reversed paths such as the ones shown in Fig. 2.21(b), interfere constructively to give rise to a weak localization correction. On applying a B field, magnetic flux threads the loop formed by time reversed paths, thus introducing a phase difference between the time reversed paths, so that the interference may no longer be constructive. If only a single pair of time reversed paths were to be participating in this process, the variation of B would cause the resistance to oscillate, as the interference alternated between being constructive and destructive. However, in a 2D system, many different pairs of time reversed paths exist, and contribute to coherent backscattering in the absence of B. The length of the time reversed paths is limited by l_ϕ, longer the l_ϕ, bigger is the size of largest possible path of an electron which scatters coherently back to its initial position. As the phase difference introduced is different depending on the length of the loop formed by the time reversed paths, different time reversed paths give a different magnitude of interference corrections, leading to a net reduction of constructive interference, and therefore of the resistance of the sample itself. If l_ϕ is large in a sample, the range of areas of the loops formed by phase coherent paths is wider. Hence an applied B field is much more effective at reducing the net constructive interference, and giving rise to a negative MR.

The magnitude of this MR depends on not just τ_ϕ, but also on τ_s, which is the spin-flip scattering time, related to the presence of magnetic impurities in the system, which can cause decoherence in the system. The sign and magnitude of the MR is also dependent on τ_{so}, the spin-orbit scattering time of the system, which is dependent on the

mechanism of spin scattering or dephasing in the system, and is small for strong SOI. If τ_{so} is smaller than τ_{ϕ}, the interference becomes destructive, since the time reversed final wavefunctions are out of phase with each other, owing to the fact that rotation of the spin by 2π reverses the spin-state of spin-1/2 particles. The equation describing this weak localization/antilocalization MR is dependent on the type of SOI present in the system, i.e., whether it has a cubic or a linear dependence on momentum.[**115, 116**] In particular, in traditionally studied semiconductor heterostructures in which valence bands originating from p orbitals play a role in transport, Rashba SOI has a linear dependence on momentum, whereas Dresselhaus SOI has a linear as well as cubic dependence on momentum. Iordanskii, Lyanda-Geller, and Pikus[**117**] worked out the form of conductivity corrections due to a combination of these effects, considering spin relaxation due to the Dyakonov-Perel mechanism.[**118**] In (001) oriented STO-based 2DCGs, the orbital ordering of the t_{2g} bands was considered by Kim *et al.* [**116**], who calculated conductivity corrections based on a linear-in k Rashha SOI in the d_{xy} bands and a cubic-in k Rashba SOI in the $d_{yz,zx}$ bands.[**73**] If SOI is substantial, then Zeeman effects can play a role as well, with the electron g factor of the 2DCG as an additional parameter. [**119**] Finally, the exact form of the T and B dependencies are dictated by the dimensionality of the system with respect to weak localization, i.e., if the associated length scale for decoherence, $l_{\phi} = \sqrt{D\tau_{\phi}}$ is greater than the film thickness d, then the film is in the two-dimensional limit for weak localization. In STO-based systems, estimates of l_{ϕ} obtained so far indicate that the system is 2D for weak localization.

Despite the complexity of the various theories, it is clear that an applied B, which causes decoherence, leads to a negative MR in the absence of strong SOI, and a positive

MR in the presence of a strong SOI. The corrections due to localization behavior decrease with increasing B, and completely die out at $B \sim \hbar/el^2$. The changes in conductivity due to weak localization/antilocalization are of the order of $\sigma_0 = 2e^2/h$, while the field scales of the effects, B_α, depend on D and the relevant scattering time τ_α as $B_\alpha = \hbar/4eD\tau_\alpha$. Estimates of B_α can be obtained by fitting to the Eqn. 2.7 describing $\Delta R_{loc}(T, B)$ in two dimensions, derived by Hikami *et al.*, [**120**] considering the Elliot-Yafet spin relaxation mechanism. This equation ignores Zeeman contributions.

$$\frac{\Delta R_{loc}(T,B)}{R_s} = \frac{R_s}{2\pi^2\hbar/e^2}\Big[-\frac{3}{2}\Psi\Big(\frac{1}{2}+\frac{B_2}{B}\Big)+\frac{1}{2}\Psi\Big(\frac{1}{2}+\frac{B_1}{B}\Big)+\ln\frac{B_0}{B}\Big]. \tag{2.7}$$

Here $B_1 = B_\phi + 2B_s$, $B_2 = B_\phi + (4/3)B_{so} + (2/3)B_s$, and B_0 is the field associated with the elastic scattering time τ. When analyzing the differential MR due to localization corrections at a fixed temperature, we need to evaluate the following:

$$\frac{\delta R_{loc}(T,B)}{R_s} = \frac{\Delta R_{loc}(T,B) - \Delta R_{loc}(T,B=0)}{R_s}. \tag{2.8}$$

Noting that the asymptotic form for $\Psi(1/2+B_\alpha/B)$ as $B \to 0$ is $\ln(B_\alpha/B)$, one arrives at the following form for the differential localization correction:[**95**]

$$\frac{\delta R_{loc}(T,B)}{R_s} = -\frac{3}{2}f(B,B_2)+\frac{1}{2}f(B,B_1). \tag{2.9}$$

Here the first term is the triplet Cooperon contribution while the second term is the singlet Cooperon contribution, and the function f is given as:

$$f(B, B_\alpha) = \frac{R_s}{2\pi^2\hbar/e^2}\Big[\Psi\Big(\frac{1}{2}+\frac{B_\alpha}{B}\Big) - \ln\Big(\frac{B_\alpha}{B}\Big)\Big]. \tag{2.10}$$

In the context of STO-based 2DCGs, it is difficult to obtain reliable estimates of the diffusion constant D of the system as discussed earlier, hence we describe $\delta R_{loc}(T, B)$ in terms of characteristic length scales l_α instead of τ_α, with $l_\alpha^2 = \hbar/4eB_\alpha$. We see that B_0 drops out of the equation for $\delta R_{loc}(T, B)$, which is useful, given the difficulties in estimating τ.

As discussed earlier, the variation of SOI with V_g in (001) LAO/STO is dependent on a variety of factors. Many MR measurements have shown the presence of weak localization/antilocalization corrections in (001) LAO/STO.[**18, 88**] For large positive values of V_g, negative magnetoconductance is observed at low fields, and as V_g is decreased, magnetoconductance is found to become positive at low fields, indicating that SOI is stronger at positive gate voltages where $d_{yz,zx}$ bands also participate in transport. Some recent experiments have also shown a non-monotonic dependence of SOI on V_g,[**121**] considering a combination of cubic and linear k dependent contributions to SOI coming from different t_{2g} bands, as predicted by theory for (001) oriented STO-based 2DCGs.[**73, 76**] To my knowledge, there has been one experimental study examining weak localization/antilocalization in (111) LAO/STO,[**122**] which found that SOI has a non-monotonic dependence on V_g. So far, no theoretical predictions have been made for the t_{2g} bands in (111) oriented STO-based 2DCGs, with regards to the specific k-dependence of SOI. In the absence of

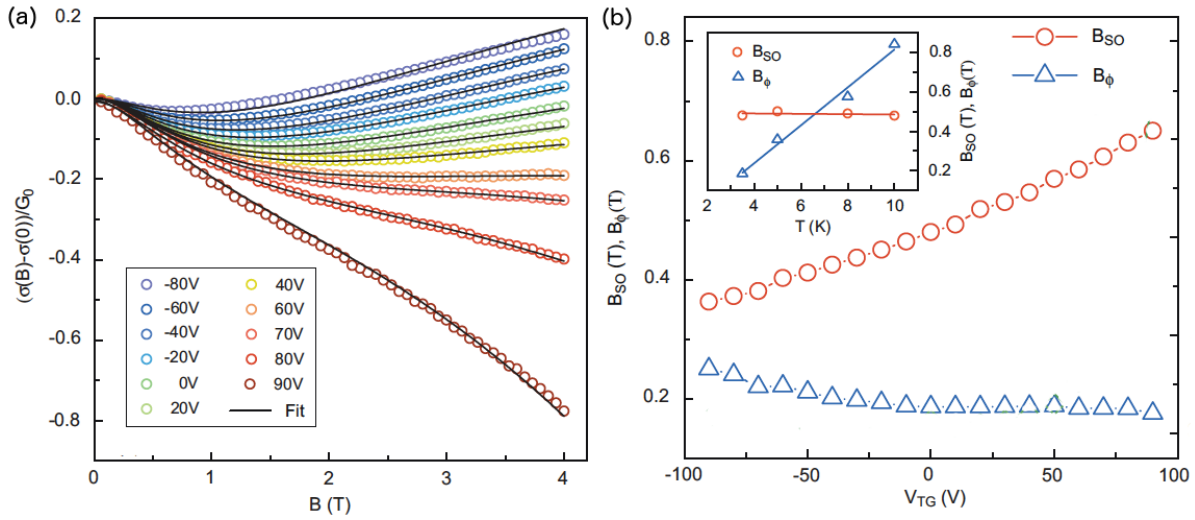

Figure 2.22. **a,** Magnetoconductance for a (001) LAO/STO sample for different values of V_g, showing a transition from weak antilocalization at positive V_g to weak localization at negative V_g, at $T = 3.5$ K. The fits are to Eqn. 2.6, plus a quadratic background term to account for classical orbital MR. **b,** Characteristic fields for phase decoherence, B_ϕ, and spin-orbit scattering, B_{so}, as a function of top gate voltage V_{TG} for data in Fig. 2.21(a). Inset: B_ϕ and B_{so} as a function of T for $V_{TG} = 0$ V. Images and captions adapted from Ref. [**88**].

such theoretical predictions, I have based my analysis of the MR due to weak localization/antilocalization in my (111) LSAT/STO sample, which I will present in Chapter 4, on the theory of Hikami *et al.*, i .e., using Eqns. 2.7-2.10.

2.4.2.5. Contributions due to EEI in the diffusive limit, $\Delta R_{EEI}(T, B)$. EEI effects contribute to the sample resistance in a number of ways. Large angle inelastic collisions in the ballistic limit contribute to the T^2 dependence of resistance discussed earlier. Small as well as large angle collisions cause decoherence of electron wavefunctions, thus affecting τ_ϕ which in turn affects the localization corrections. On the other hand, many-body EEI effects in the diffusive limit can cause a change in the density of states of the 2DCG,[**123**] and lead to the following corrections to the conductivity:

(2.11)

$$\Delta\sigma_{EEI}(T,B) = \frac{e^2}{\hbar}\frac{1}{4\pi^2}\Big(2-\frac{3F}{2}\Big)\ln\Big(\frac{k_BT\tau}{\hbar}\Big)-\frac{e^2}{\hbar}\frac{1}{4\pi^2}Fg_2\Big(\frac{g\mu_BB}{k_BT}\Big)-\frac{e^2}{\hbar}\frac{1}{4\pi^2}g_1(T)\Phi_2\Big(\frac{2DeB}{\pi k_BT}\Big)$$

Here the first term is the field-independent exchange and singlet Hartree contribution of the particle-hole channel, the second term is the triplet Hartree contribution, while the third term is the orbital contribution due to the particle-particle channel.[**94**] F and $g_1(T)$ are both related to the screened Coulomb potential. Since typically $|g_1(T)| << 1$, this term is usually ignored. F is of the order of unity and hence the first two terms of the equation must be considered in our analysis.

The second term gives a negative correction to the conductivity, and hence a positive $\Delta R_{EEI}(T,B)$. $g_2(T,B)$ has a functional form, $\sim 0.084(g\mu_BB/k_BT)^2$ for $g\mu_BB/k_BT << 1$ and $\sim \ln(g\mu_BB/k_BT)/1.3$ for $g\mu_BB/k_BT >> 1$. For $T = 100$ mK and assuming $g = 2$, this field scale is $B \sim 75$ mT.

The first correction to the conductivity, although independent of B, leads to a negative contribution to the resistivity, which we can obtain by inverting the conductivity tensor, and noting that EEI corrections also lead to a contribution in the Hall coefficient, which are twice the corrections to the resistivity due to EEI effects. These corrections, calculated by Houghton [**124**], are given as

(2.12)

$$\Delta R^{ex}_{EEI}(T,B) = \frac{-m^*}{4\pi^2\hbar n\tau}\Big(2-\frac{3F}{2}\Big)[1-(\omega_c\tau)^2]\ln\Big(\frac{k_BT\tau}{\hbar}\Big)$$

As we noted earlier, $\omega_c\tau$ in high mobility samples, especially at large positive values of V_g, can be substantial even at small values of B. This discussion makes it clear that for analyzing low field data, we must consider the effect of EEI along with localization. Usually, the procedure is to isolate the EEI contributions by considering large fields, at which localization corrections are negligible. However, for the high mobility STO-based 2DCGs, the classical contribution rapidly increases with increasing field, making the resolution of EEI contributions in this manner impossible. Another way to isolate EEI is by measuring MR in fields parallel to the 2DCG, since this would eliminate the large positive background of $\Delta R_{cl}(B)$. However, in the case of STO-based 2DCGs, this runs into difficulties as one still has to contend with a negative quadratic background from magnetic scattering, not to mention weak localization. It is also possible in principle to isolate the EEI contribution using R vs T data, in cases where the $\Delta R^{ex}_{EEI}(T,B)$ is negligible due to $\omega_c\tau$ being very small. Since EEI leads to a logarithmic increase in R as temperature is lowered, similar to weak localization effects, this is usually done by measuring R_s vs. T in the presence of a magnetic field larger than that required to suppress localization effects. However, the application of a magnetic field would also affect the $\Delta R_{mag}(T,B)$ contribution in STO-based 2DCGs, making the isolation of EEI effects difficult. We do expect EEI effects in STO-based 2DCGs to be substantial especially at the low temperatures of study, given that the carriers originate from the narrow $3d$ t_{2g} orbitals of Ti.

2.4.2.6. Contributions due to superconducting fluctuations, $\Delta R_{SC}(T,B)$. Finally, we discuss the contribution due to superconducting fluctuations. (001) [**9, 13, 15**] as well as (111) LAO/STO[**10, 122, 125**] interfaces under certain growth conditions were

observed to undergo a superconducting (SC) transition below about 300 mK, similar to bulk electron-doped STO.[**9, 47**] Although at first glance the SC state in LAO/STO may seem to be very similar to the one in bulk STO, there are some interesting differences. SC in LAO/STO heterostructures is two dimensional, as the SC coherence length has generally been found to be larger than the thickness of the 2DCG.[**15**] A 2D SC system can undergo a superconductor-insulator transition (SIT), which is a topic of great theoretical interest. Such SITs have indeed been observed in LAO/STO systems, which can be tuned into a weakly insulating state by the application of B,[**9, 127**] as well as the application of V_g,[**15, 31, 88**] as shown in Fig. 2.23(a) for (001) oriented LAO/STO. It is interesting to note that in the insulating state the resistance either saturates or increases very slowly. A classic SIT in which the resistance in the insulating state diverges at the lowest temperatures, as shown in Fig. 2.23(b) for a granular Pb film,[**126**] is not observed, for reasons that have not yet been explored in detail. The superconducting transition temperature as well as the critical current was found to vary non-monotonically with V_g. Maniv *et al.* attributed this nonmonotonicity in SC transition temperatures to a non-monotonic population of the conduction bands participating in transport, caused by electron-electron interactions (EEI).[**128**] SC in the LAO/STO system has in some cases been found to coexist with ferromagnetism, using various probes such as a Scanning Superconducting Quantum Interference Device (SQUID),[**14**] torque magnetometry,[**13**] and electrical transport measurements[**15**] raising the possibility of exotic states such as the Fulde-Ferrel-Larkin-Ovchinnikov state, or an anisotropic SC order parameter.[**129**] For a detailed discussion of the superconducting state in (001) and (111) orineted LAO/STO, I point the reader to the theses of Manan Mehta and Sam Davis, respectively.[**30, 31**]

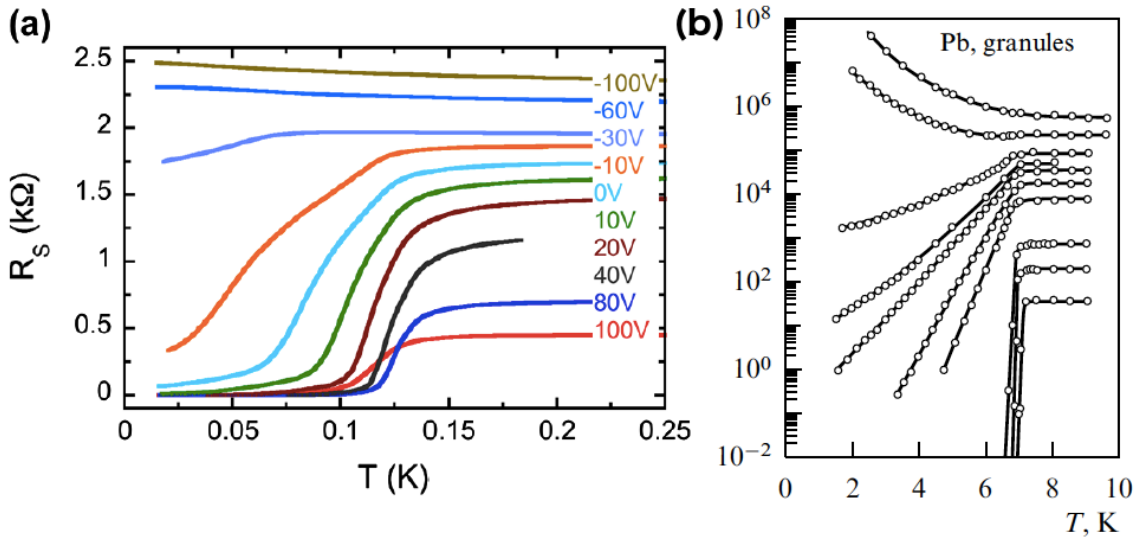

Figure 2.23. **a,** Variation of R_s with T for different values of V_g for a (001) LAO/STO sample, showing a V_g-tuned SIT. Image and caption adapted from Ref. [**15**]. **b,** SIT in granular Pb films. Different curves are for different film thicknesses. Image taken from Ref. [**126**].

In the vicinity of a superconducting transition, Aslamazov-Larkin[**130**] corrections to the conductivity, which are caused by fluctuating Cooper pairs, and Maki-Thompson[**131**] corrections which are caused by the coherent scattering of carriers off the fluctuating Cooper pairs, can be important, depending on sample cleanliness and measurement temperature.[**132**] Due to the absence of a full superconducting transition in the sample discussed in this thesis, we ignore this effect in our analysis, however, we note that it must be taken into consideration in samples which do show a superconducting transition.

2.5. Review of experiments on LSAT/STO

LSAT, a commonly used substrate material, is a perovskite in which the A sites are La^{3+} or Sr^{3+} ions, and the B sites are Al^{3+} or Ta^{5+} ions. The band gap is $\sim$ 4.9 eV, the

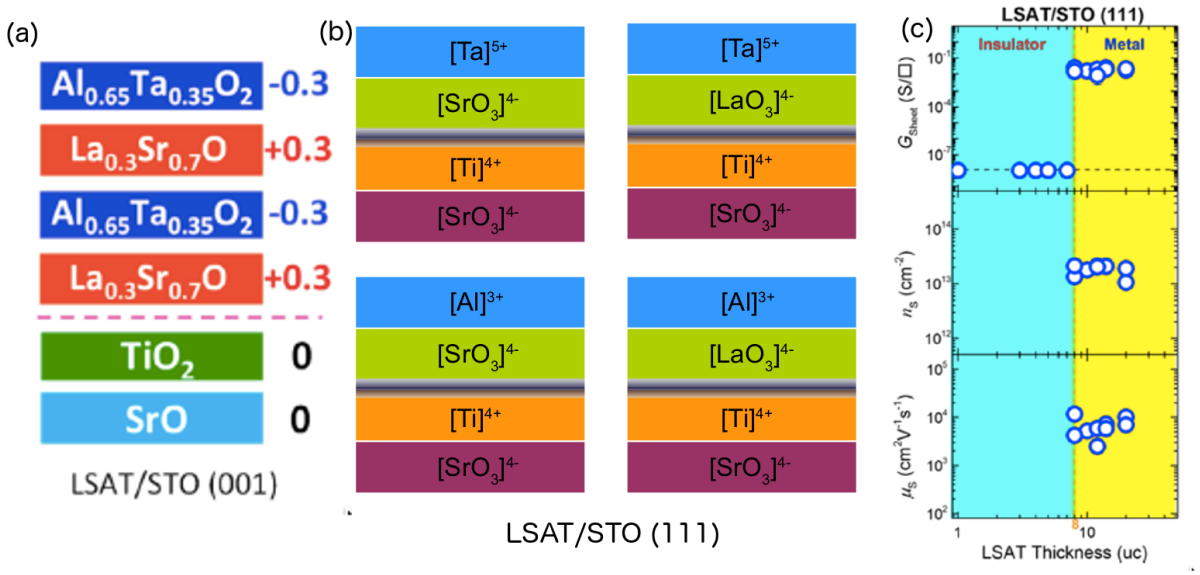

Figure 2.24. **a,** Layered structure of LSAT/STO in the (001) orientation, showing the polar discontinuity. **b,** Four possibilities for the layered structure in (111) oriented LSAT/STO. **c,** Conductance, sheet carrier density, and mobility calculated using a single band model for LSAT/STO, as a function of the number of unit cells of LSAT. Image taken from Ref. [**29**].

dielectric constant is 22, and the lattice constant is 3.868 Å, which gives it a 1% lattice mismatch with STO. It has a cubic structure at ambient temperature, and undergoes a structural transition to a tetragonal phase, similar to STO, below about 150 K.[**28**] This implies that the interfacial layers in LSAT/STO are less strained as compared to the interfacial layers in LAO/STO. Biaxial strain is known to affect carrier mobility by causing slight changes to the bond angles and lengths of STO, hence changing the band structure. [**22**]

In 2016, Huang *et al.* found that the epitaxial deposition of more than 5 unit cells of LSAT on (001) oriented TiO_2 terminated STO, created a 2DCG at the interface, similar to the LAO/STO systems.[**29**] In the (001) orientation, the system is made up of planes of alternating charges, as shown in Fig. 2.24(a). These LSAT/STO 2DCGs were found

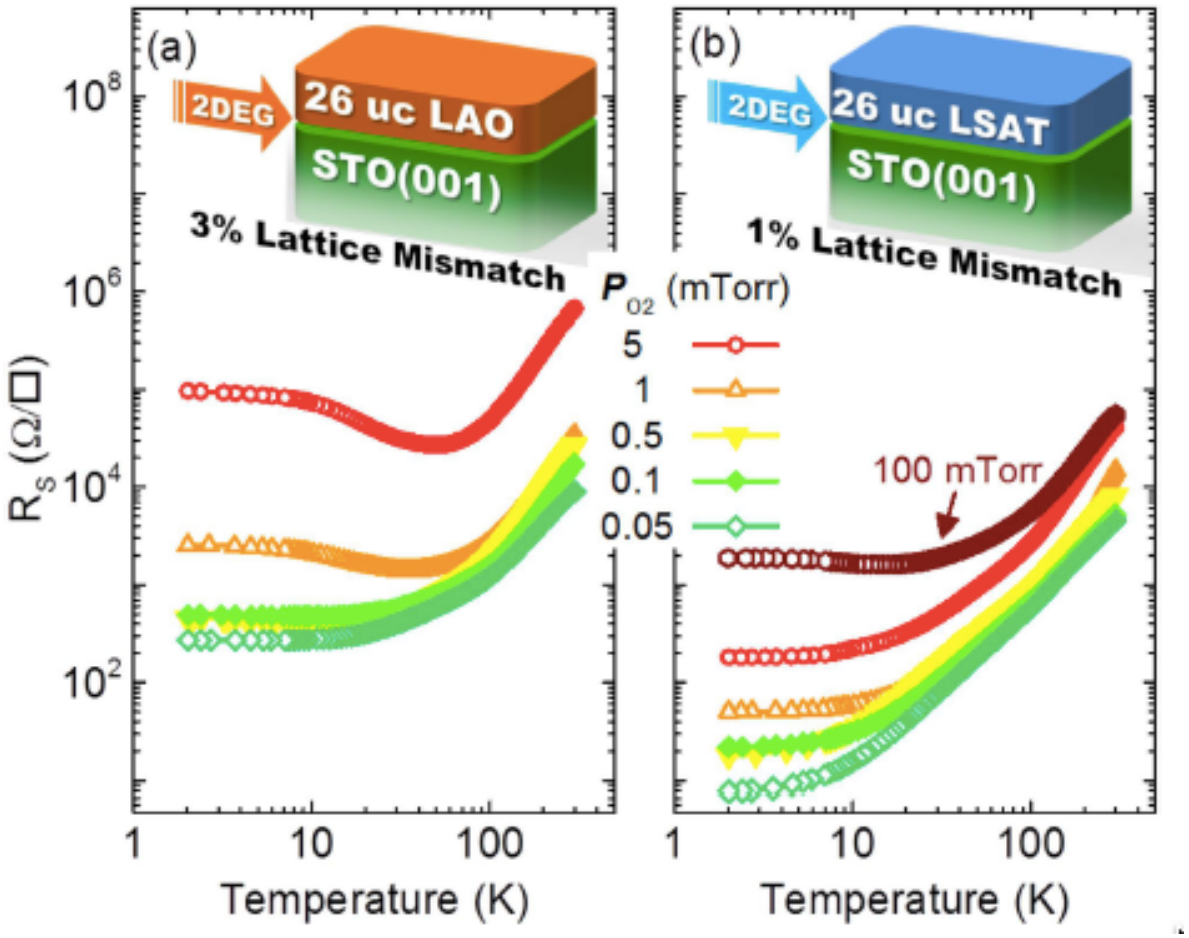

Figure 2.25. Variation of R_s with T for different values of oxygen partial pressure P_{O_2} for **a,** (001) LAO/STO samples, and **b,** (001) LSAT/STO samples. Image taken from Ref. [**29**].

to have a more metallic character as compared to LAO/STO 2DCGs grown in identical conditions. Fig. 2.25 shows that the LSAT/STO system shows a larger residual resistance ratio (RRR), and has a lower resistance at $T = 2$ K, than the equivalent LAO/STO sample. The (001) LSAT/STO samples also showed other indications of the presence of multiband transport and high mobility carriers, such as nonlinear Hall effect at high positive values of V_g, and SdH oscillations, as shown in Fig. 2.26. They analyzed their data in terms of

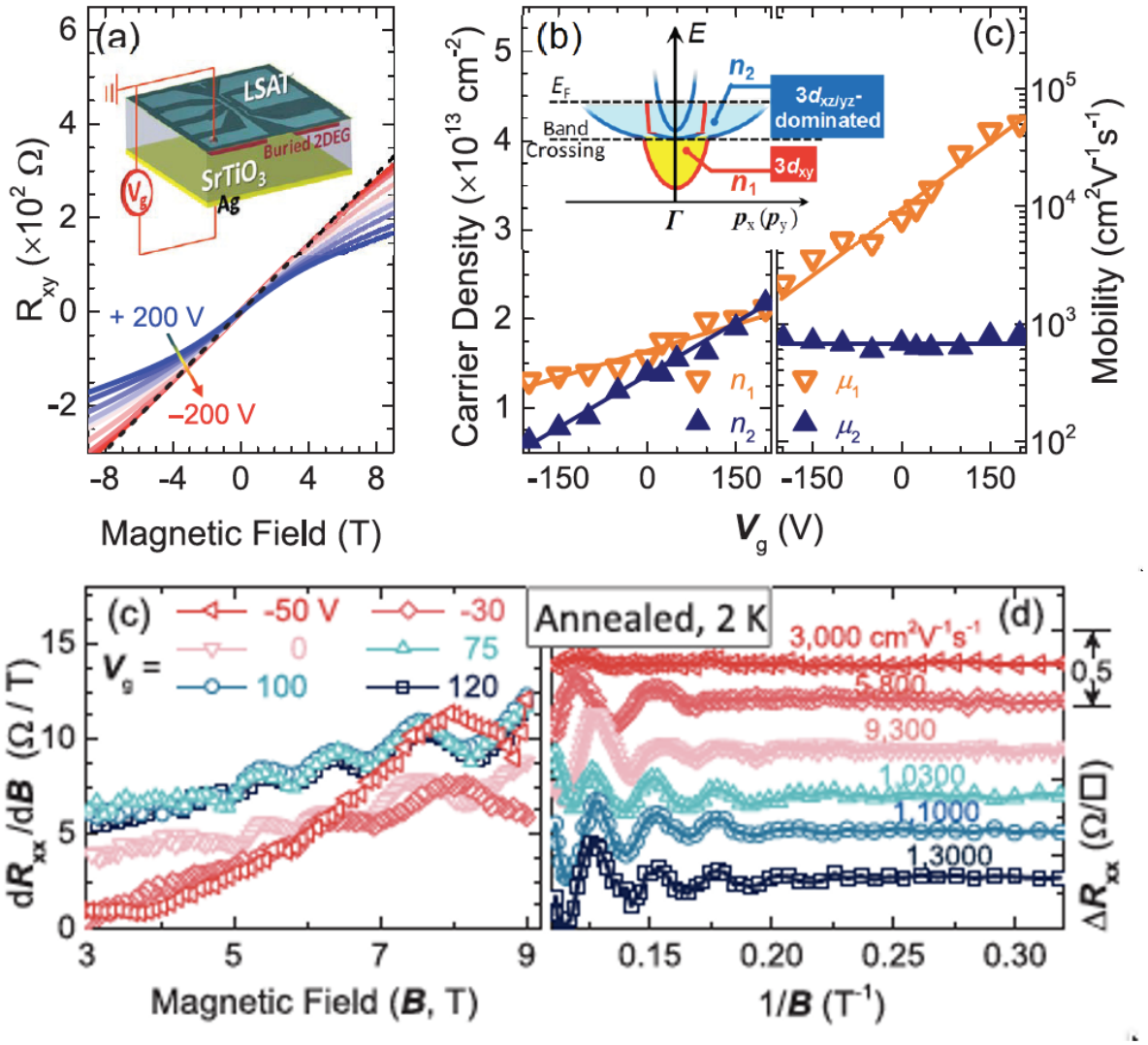

Figure 2.26. **a,** Hall resistance as a function of B for different values of V_g for a (001) LSAT/STO sample, at $T = 2$ K. **b,c** Carrier density and mobility calculated using a two-band model, according to Joshua *et al.*'s analysis.[**74**] Inset shows a cartoon of the band structure of (001) STO-based 2DCGs. **d,** Derivative of the longitudinal resistance as a function of B, for different values of V_g. **e,** Amplitude of SdH oscillations as a function of $1/B$ for different values of V_g. Image taken from Ref. [**133**].

a two band model, in which electrons first fill the d_{xy} orbitals and at higher V_g, start to preferentially fill the $d_{yz,zx}$ orbitals.[**133**] Some of their samples also showed the resistance

minimum at a temperature of few Kelvins, as well as a negative MR in fields parallel to the 2DCG, which was taken to be a signature of magnetic scattering.[**134**]

In the (111) orientation, LSAT/STO is made up of alternating charged planes as shown in Fig. 2.24(b). The interface becomes conducting when at least 8 unit cells of LSAT are grown on Ti terminated STO. In the rest of this thesis, I explore how this relatively less strained system behaves in the (111) orientation.

CHAPTER 3

Experimental Methods

In this chapter, I will describe the various experimental techniques used in order to fabricate, characterize, and measure the LSAT/STO sample discussed in this thesis. In chronological order, the steps to fabricate the sample are: PLD of an LSAT film on the STO substrate, sample cleaning, photolithography to define the Hall bar pattern, Ar ion milling to define Hall bars, photolithography to define contact pads, e-beam evaporation to deposit contact pads, and finally, wire bonding. Characterization methods used are reflection high-energy electron diffraction (RHEED), atomic force microscopy (AFM), and Laue diffraction. The thesis mainly describes MR measurements in perpendicular (B) and parallel ($B_{||}$) fields, along with electrical-gate voltage (V_g) and temperature (T) dependence measurements, in order to glean information about the sample.

Many of these techniques have been discussed in detail in reference to LAO/STO in earlier theses from the Northwestern Mesoscopic Physics Group, so I will only discuss those briefly, and point the reader to the relevant earlier thesis for reference. Here I will elaborate on the aspects that are different in the case of LSAT/STO. I will also focus on the fabrication of the photomask used to make the Hall bar devices, and on the construction of the Ar ion mill, both of which are of the author's design.

3.1. Sample fabrication and characterization

The results described in this thesis were obtained from four Hall bars, with a width of 100 μm and a length of 600 μm, fabricated on a chip of (111) LSAT/STO, with two Hall bars aligned along the $[1\bar{1}0]$ direction, and the other two along the $[\bar{1}\bar{1}2]$ direction. In this section I will describe the fabrication and structural characterization processes.

3.1.1. Pulsed laser deposition

The existence and properties of the two dimensional carrier gas (2DCG) at the (111) oriented interface of LSAT and STO depend on a stoichiometric, uniform, and epitaxial deposition of LSAT on top of STO, over the whole area of the STO substrate to be used for device fabrication. T. Venkatesan's group in the National University of Singapore (NUS) specializes in this process, using the technique of PLD. This technique, the theory of which has been described in detail in the thesis of Manan Mehta,[**30**] has played a crucial role in the field of complex oxide materials, by enabling the growth of multi-element compounds and heterostructures with high yield.[**135**] Here I will specify the process parameters used in the synthesis of the (111) LSAT/STO heterostructure studied in this thesis.

The PLD synthesis of the sample was performed in T. Venkatesan's group by Zhen Huang. A double-side polished (111) oriented STO substrate of size 5 mm $\times$ 5 mm, thickness 500 μm, and miscut angle < 0.5 degrees was obtained from Crystec GmbH.[1] The STO surface was treated with two rounds of a 10:1 buffered oxide etch, which is an aqueous solution of HF and NH_4F, for 30 s, followed by a deionized (DI) water rinse of 90 s. Finally the substrate was annealed at 900 C in air for 1.5 hours, in order to ensure a

[1] http://www.crystec.de/crystec-d.html

smooth Ti terminated STO surface, free of SrO islands. The STO substrate was attached to the sample holder in the PLD chamber using conducting silver paste. A single crystal LSAT target was used for the PLD process, carried out at an oxygen partial pressure of 10^{-4} Torr and a temperature of 800 C. A KrF excimer laser of wavelength 248 nm and energy density 1.5 - 1.8 J/cm^2 was used to ablate the target, at the rate of 10 pulses per (111) unit cell. The film growth was monitored using *in situ* RHEED. The periodic variation in intensity of the RHEED pattern, shown in Fig. 3.1, indicates cyclic changes in coverage of the growing film. When the intensity of consecutive maxima is about equal to the starting intensity, as seen in Fig. 3.1 for times greater than 60 s, it indicates perfect layer-by-layer, epitaxial growth, with the maximum in intensity occurring at full unit cell coverage, and the minimum occurring at half coverage. A decay in amplitude of oscillations however indicates some degree of 3-D island like growth, rather than layer-by-layer growth, and is a common observation during PLD synthesis.[**135**] This was corrected by increasing laser intensity at 30 s and 60 s of growth. 12 unit cell layers of LSAT were grown on top of (111) STO, giving an LSAT film of thickness 2.6 nm. As discussed in section 2.5 of the previous chapter, for (111) LSAT/STO the 2DCG forms at the interface for over 8 unit cells of LSAT deposited on STO.[**29**]

A perfectly deposited film shows the presence of atomic steps over the entire surface. However, the morphology of the steps is sensitively dependent on various parameters, as I will now describe. This can be important, as some experiments have shown that current in the 2DCGs in STO-based heterostructures flows along step edges.[**83**] Also, there might be a connection between the quality of steps and the nature of the 2DCG, as described by Sam Davis in his thesis.[**31**] One reason for poor quality steps can be the

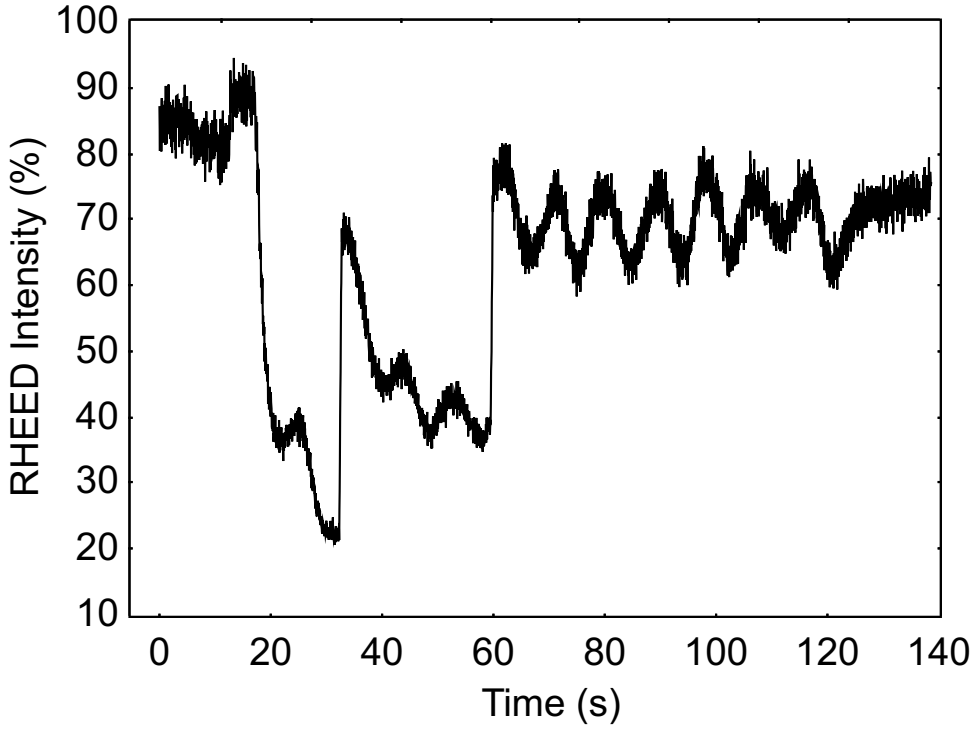

Figure 3.1. Oscillations in the intensity of a RHEED spot as a function of time during PLD synthesis. The abrupt changes in intensity at 30 s and 60 s indicate times at which the laser intensity was increased. (Data courtesy of Dr. Z. Huang from NUS)

presence of SrO islands still left over on the STO substrate before the PLD deposition. Another reason might be a large miscut angle, which can lead to the bunching of atomic steps in order to relieve strain.[**136**] This can be especially important in the case of (111) LAO/STO, since the carrier density of the 2DCG varies non-monotonically with the number of layers of LAO on top of STO,[**5**] but should not present a problem in the case of (111) LSAT/STO, where carrier density and mobility stay constant for more than 8 unit cells of LSAT deposited on STO.[**29**] The step width also depends on the miscut angle, and is given by $na/\tan\theta$, where n is the number of bunched steps, a, is the unit cell

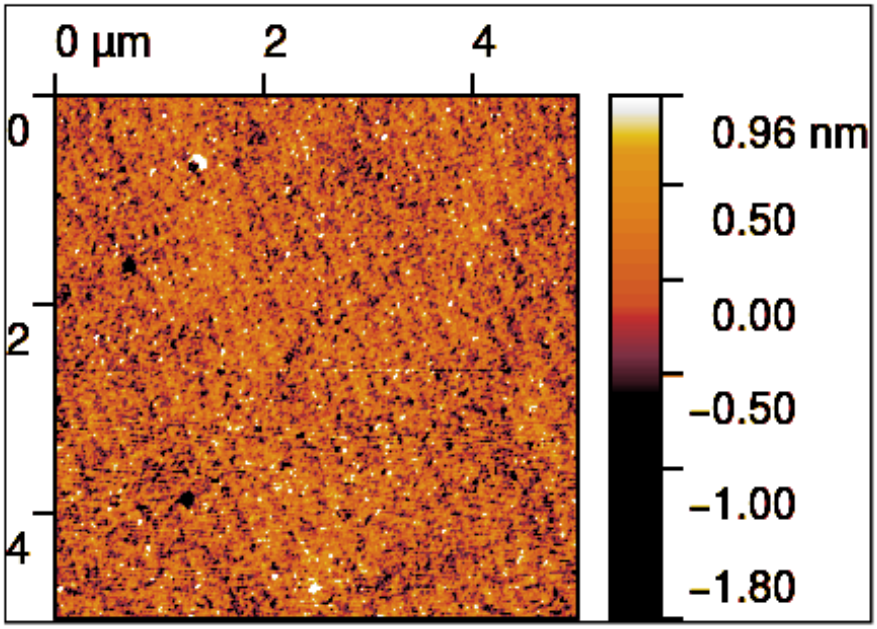

Figure 3.2. AFM scan of the sample, showing evidence of atomic terraces.

height, and θ is the miscut angle. Even for a miscut angle varying between 0.1 degrees and 0.5 degrees and assuming no bunching of steps, the step width can vary between 24 nm and 110 nm, given a unit cell height along the (111) direction of 2.2 Å.[**137**] Finally, if the miscut is along an in-plane crystal direction, then we get very smooth, uniform steps, while a difference in the in-plane crystal direction and the miscut direction can lead to wavy or jagged steps.[**136**] Figure 3.2 shows a 5 μm $\times$ 5 μm AFM scan of the sample studied in this thesis, which does show atomic steps. However, the quality of the atomic steps is not as good as has been observed on either (001) [**121**] or (111) oriented LAO/STO,[**31**] or (001) oriented LSAT/STO samples [**29**] discussed in the literature. As discussed in the thesis of Sam Davis, the step quality can have a profound effect on the transport properties of the sample. In particular, it can limit the range of V_g over which

reliable Ohmic contacts can be made with the interfacial conducting gas. For the sample described in this thesis, the range of V_g was restricted to be greater than -40 V, which will be discussed further in the next section.

3.1.2. Fabrication of Hall bars

The next step was to fabricate Hall bars on the sample to enable 4-probe electrical transport measurements. For error-free and reproducible lithography, sample cleanliness is a key requirement. The following is the general procedure to clean the sample:

(1) The as-received sample has the residue of silver paint on the back of the sample as a result of the PLD process. This residue is first gently scraped off using a razor blade.

(2) The sample is sprayed with acetone for a minute, immediately followed by IPA, in order to remove any leftover silver paint residue. Zero grade nitrogen (N_2) gas at a pressure of 2 to 3 psi is used to dry the sample off. The direction of the gas stream should be close to parallel to the sample surface. It is important to not let silver paint residue dry on the sample surface as it can be almost impossible to remove once dry.

(3) Next a stream of 2 MΩ DI water is run over the sample for a minute, which removes any ionic impurities that may be present on the sample surface. The sample is immediately sprayed with IPA to dissolve the water, and then blow dried with N_2 gas.

(4) Finally, the sample is sonicated for 2 minutes in acetone to remove remaining organic impurities, followed by sonication for 2 minutes in IPA to remove residue left behind by the acetone, before finally blow drying with N_2 gas. It is necessary to ensure that the IPA film recedes uniformly off the sample, which is a sign that the sample is likely to be clean.

This cleaning protocol also removes any adsorbed water from the sample surface, which improves the adhesion between the sample surface and the photoresist. Once cleaned, the sample is spin coated with resist immediately to minimize readsorbtion of water/ contamination.

After cleaning the sample, photolithography using S1813 photoresist [2] was used to make the Hall bar pattern. The S1813 photoresist thickness is ~ 1.2 μm with the spin process we use.[**30, 31**] The usual process employed when depositing materials into a photolithographically defined pattern, calls for the use of a layer of another resist such as LOR 7B underneath the S1813, in order to create an undercut in the resist and ensure a clean liftoff. However, a LOR 7B underlayer was not used in this first step of photolithography since the resist was to be used as an etch mask for the ion milling process, and in this case, having an undercut would be detrimental to obtaining sharply defined edges on the Hall bar. Due to the small size of the sample, the resists show a tendency to bead at the corners of the sample during spinning. This problem can be mitigated by sticking the sample using a little bit of resist onto a larger carrier wafer, for example, a piece of cover glass or silicon, before spinning the resist on the sample, although this was not done for the sample studied in this thesis.

The SUSS MA/BA6[3] mask aligner in the NUFAB cleanroom[4] was used to expose the photoresist, in order to ensure a proper alignment of Hall bars along the in-plane crystalline axes, which are along the sample edges. The alignment is within a few degrees, limited by the fact that the sample usually does not have perfectly right angled corners,

[2]Microposit series S1800 photoresists from Microchem Corp., http://www.microchem.com/
[3]SUSS MicroTec AG, Garching, Germany, https://www.suss.com/en
[4]http://www.nufab.northwestern.edu/

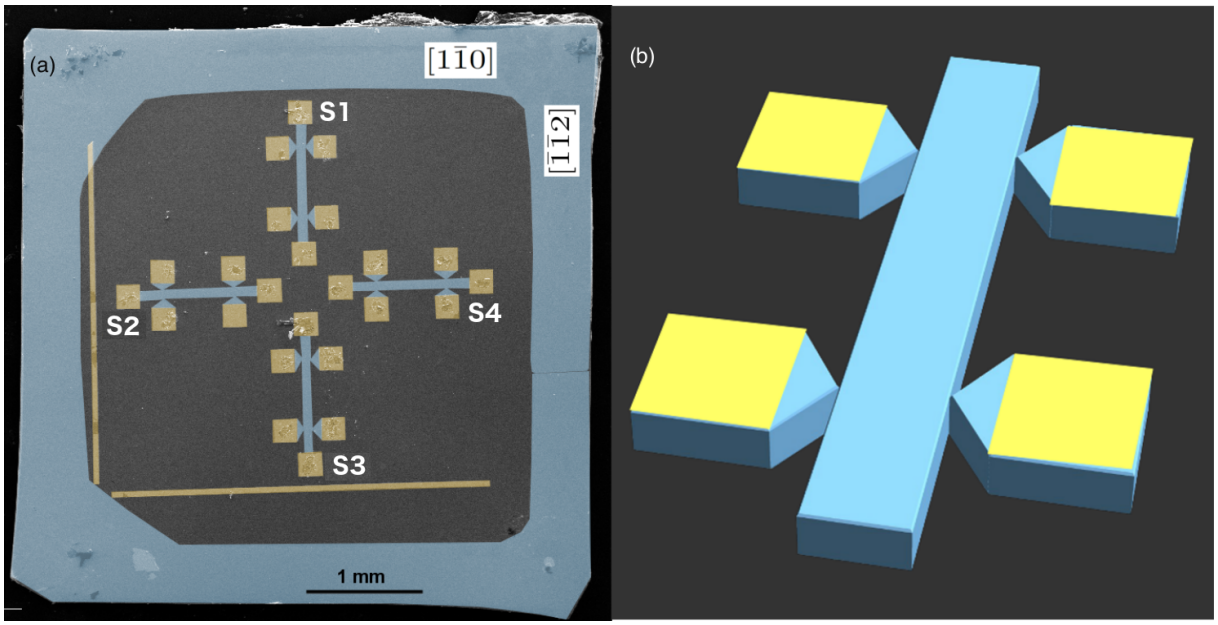

Figure 3.3. **a**, Colorized SEM image of the sample. Scale bar is 1 mm. Areas in blue denote regions of the sample with LSAT still present. Areas in grey denote regions where bare STO is present. Areas in yellow denote regions where Ti/Au has been deposited. Note that LSAT is present underneath the contact pads as well. Residue from wire bonds is visible on some of the contact pads. The Hall bars named S1 and S3 have their lengths along the [$\bar{1}\bar{1}$2] direction, while the Hall bars S2 and S4 have their lengths aligned along the [1$\bar{1}$0] direction. I will refer to these hall bars in the next chapter. **b**, Schematic of a Hall bar. The color scheme is the same as in Fig. 3.3(a). The 2DCG is present in a few nanometers of STO underneath the regions still covered in LSAT. (Image not to scale)

as can be seen from Fig. 3.3(a). For sample exposure on the SUSS aligner, the sample must be stuck using double sided tape onto a silicon carrier wafer of an appropriate diameter, which is held onto the wafer plate of the aligner using house vacuum. The hard contact mode was used along with the top-surface alignment (TSA) mode, which allows the alignment of the mask to structures on the top surface of the sample. In this configuration the alignment is possible to within $\sim$ 1 μm. The power of the 365 nm wavelength Hg arc lamp on the mask aligner was 12 mW/cm^2 at the time of exposure,

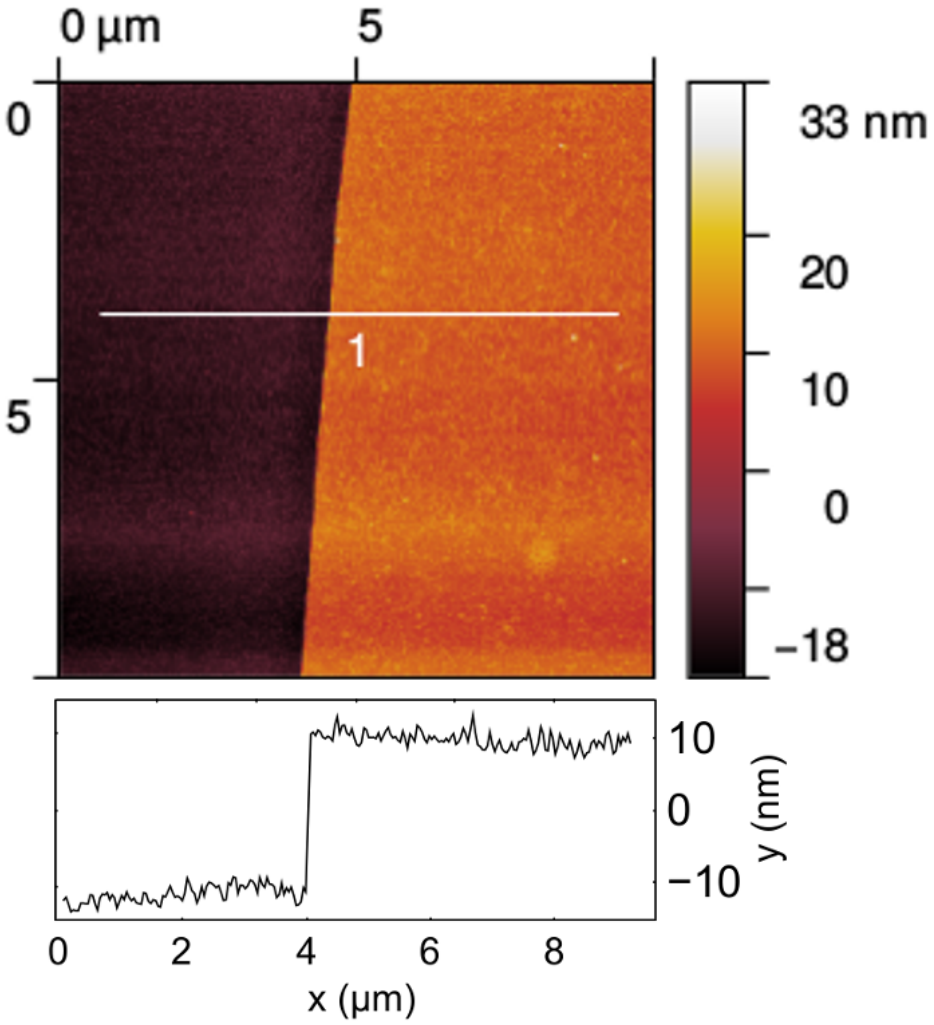

Figure 3.4. Top panel shows a 10 μm $\times$ 10 μm AFM image of the sample, obtained by scanning across an edge of a Hall bar. The sample was ion milled for 2 minutes using the parameters shown on page 109 to obtain a step of $\sim$ 20 nm, as shown in the bottom panel by the profile of line 1 marked on the scan. As noted earlier, the height of the LSAT layer is 2.6 nm.

while the exposure time was 12 s. Note that the power can change over time, and the duration of exposure must be adjusted accordingly. The sample was then ion milled for 2 minutes to remove LSAT and some STO from regions of the sample which were not

covered with resist, and were to be insulating. The details of the ion-milling process will be discussed later. Figure 3.4 is an AFM image of an edge of a Hall bar, showing an ion milling depth of ~ 20 nm.

Another step of photolithography, this time using LOR7B[5] as well as S1813 resists, was used to make the contact pad pattern, again using the SUSS MA/BA6 aligner. The contact pads were deposited with Ti/Au in the Joetek e-beam evaporation system in our group cleanroom. The specifics of the processes of spin-coating, baking, and development of LOR7B and S1813 photoresists, as well as the evaporation of metal contacts, are described in the thesis of Sam Davis, and I will not describe them here.

For making electrical transport measurements with control over the back gate voltage, V_g, the sample was mounted on top of the oxygen free Cu base of the sample puck using conducting silver paste[6]. Care must be taken to ensure that the silver paste does not climb up the sides of the sample, in order to have the applied electric back gate field directed perpendicular to the sample and not along the sample surface.

Finally, electrical contacts were made to the sample with Al-Si wires of diameter 0.001", using a wedge wire bonder, in our case the Kulicke and Soffa model 4123[7]. Especially when making wire bonds to delicate structures on insulating substrates such as STO, one must make the bond on the gold contact pin on the sample puck first, and the bond on the sample contact pad second. This will not only minimize the chances of blowing up the sample, but also prevent any little tails of the wire sticking up on the sample surface. Care must be taken to place the wire bond so that it penetrates the

[5]Microchem Corp., Westborough, MA, http://www.microchem.com/
[6]Millipore Sigma, https://www.sigmaaldrich.com
[7]www.kns.com

LSAT/STO interface in order to contact the 2DCG, since the 2DCG is buried underneath the LSAT. Figure 3.3(a) shows an SEM (scanning electron microscope) image of the sample, while Fig. 3.3(b) shows a schematic of the Hall bar. Using Laue diffraction, discussed in detail in the thesis of Sam Davis, the orientation of the Hall bars was confirmed to be along the mutually perpendicular crystalline axes, with the sample edge having the two beveled corners oriented along the $[1\bar{1}0]$ direction, and the other edge oriented along $[\bar{1}\bar{1}2]$ direction.

3.1.3. Preparation of the photomask

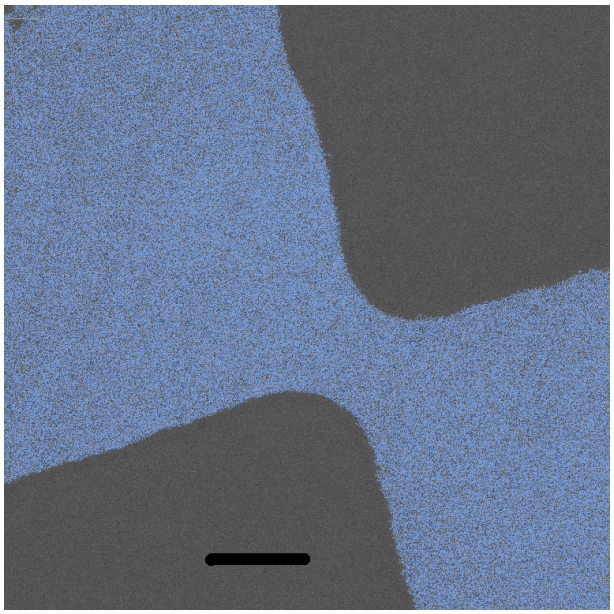

Figure 3.5. SEM image of an STO sample after photolithography using the home-made mask and the MABA6 aligner, and ion milling, for a different pattern. The size bar is 5 μm. The blue region is the unetched region. The size of the constriction according to the photomask design was 4 μm.

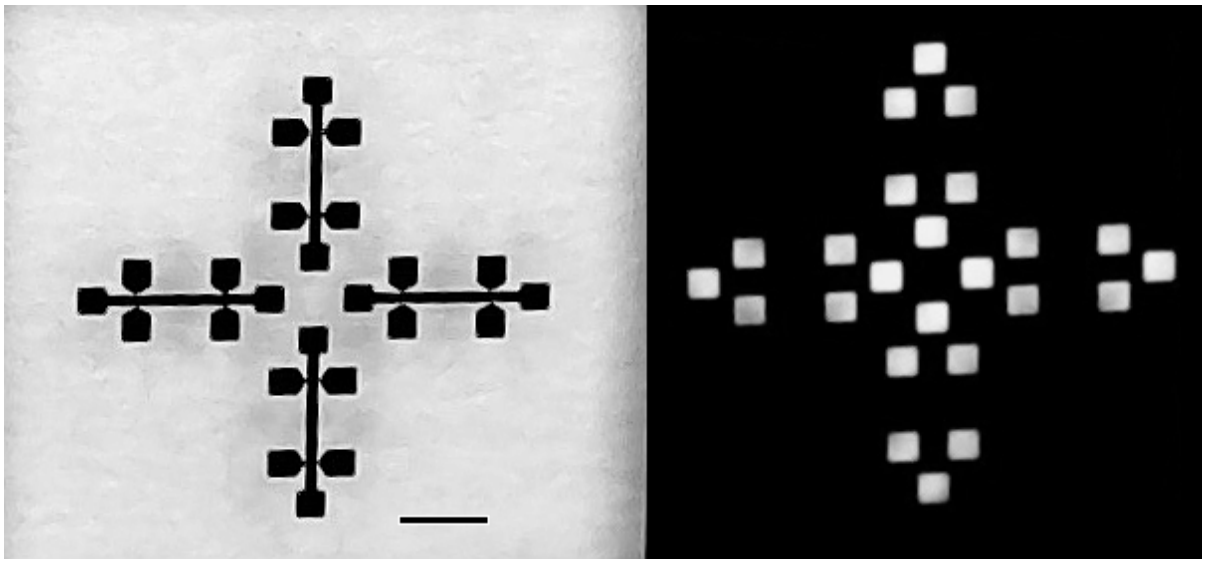

Figure 3.6. Optical microscope images of the photomask patterns used to define the Hall bar (on the left) and the contact pads (on the right). The dark portions are protected by the crome layer while the white portions are transparent. The size bar is 600 μm.

The photomask used in the steps described above was made by the author in the NUFAB cleanroom using the Heidelberg μPG 501 Maskless Aligner [8]. The blank used to make the mask was a 5" $\times$ 5" soda-lime plate of thickness 2 mm, coated with 100 nm of chromium metal and 530 nm of AZ 1518 [9] positive photoresist, and was available for purchase from NUFAB. The Heidelberg Aligner uses a 390 nm LED light source which rasters across the mask to expose custom layout patterns, which can be created in the dxf format, onto the mask surface. Exposure tests were performed to determine the exposure time and the defocus parameters. The exposure time determines the light power dosage, and was set to 12 ms. Ideally, the optics must be set to focus at half the height of the resist layer to ensure steep resist sidewalls after development. The defocus parameter on

[8]Heidelberg Instruments GmbH, Germany, https://www.himt.de/index.php/maskless-write-lasers.html
[9]Microchemicals GmbH, 1500 series developers, https://www.microchemicals.com

the Heidelberg Aligner in NUFAB can be varied in steps of 1 between -10 and 10, with a difference of 1 implying a difference of 10 μm in the position of the focus. However, the zero of the defocus parameter can change due to the detuning of the aligner optics, for example due to crashes. The defocus was determined to be -3 after exposure tests, while values of -2 and -4 both led to overexposed patterns. Once the pattern was written, the blank mask was dipped in the developer AZ400K 1:4 from Microchemicals for 60 s, at a temperature of $\sim$ 22 C, after which it was rinsed in flowing DI water for 3 minutes, and blow dried with N_2 gas. A chrome etchant was used to remove metallic chromium from parts of the mask from which the resist had been stripped. The recommended etching time is 2 minutes, however, since this is an isotropic etching process, it washed out the chrome from the smallest features on the mask, which were 2 μm in size. After a few trials, the optimal etching time for these patterns was found to be 1 minute 20 s. After treatment with the chrome etchant, the mask was rinsed thoroughly with DI water. Finally, it was sonicated in acetone and IPA, as well as exposed to UV light (LightTech G36T5VH)[10] to remove any photoresist residue.

3.1.4. Ar ion milling

I shall now describe the Ar ion milling process. This etching process uses thermionically generated electrons to create a plasma of Ar ions, which are accelerated towards the sample, leading to the removal of sample material when the Ar ions impinge on the sample. This process has the advantages of directionality and reduced contamination as compared to wet chemical etching processes. It also allows for the removal of material

[10]https://www.light-sources.com/

for which no chemical etch process is known. The plasma is remotely generated,[**138**] which implies that the sample or sample stage does not form an active electrode for plasma generation or acceleration, unlike in the case of parallel plate etchers. The process also has the advantage of a degree of independent control over the beam current and beam voltage. Figure 3.7 shows an a CAD drawing of the actual ion mill setup in the Northwestern Mesoscopic Physics Group cleanroom, whereas Fig. 3.8 shows a schematic of the ion gun itself.

The ion source is a KDC40 dc gridded ion gun[11], capable of supplying a beam voltage of up to 1200 V and a beam current of > 120 mA. Graphite grids at the outlet of the ion source collimate the ion beam, giving a beam current distribution as shown in Fig. 3.9(a). The KSC1202 power supply/controller[12] is used to control the milling parameters. The body of the mill is made of 304 stainless steel, in order to minimize sputtering damage to the chamber walls and contamination of the sample. The sample stage is a 304 stainless steel disk, attached by a rod made of oxygen free copper to a detachable KF40 blank. The sample is positioned 6" away from the outlet of the ion source. The ion mill is roughed through the turbo pump by a Welch 1402 pump[13] which has a coaxial foreline oil trap at its inlet to minimize backflow of oil and chamber contamination. The Welch pump backs the Agilent[14] TurboV-301, which is used to pump the chamber down to 10^{-7} Torr. The pumping speed of the turbo pump is 280 l/s for nitrogen. A bellows valve enables the isolation of the turbo pump and Welch pump. A TC gauge and a cold cathode gauge (or

[11]Kaufman and Robinson, fort Collins, Colorado, http://ionsources.com/products/kdc-40/
[12]Kaufman and Robinson, fort Collins, Colorado, http://ionsources.com/products/ksc-1202/
[13]Welch Vacuum - Gardner Denver, https://welchvacuum.com
[14]Agilent does not sell these anymore, but Ideal Vacuum (http://www.idealvac.com) does have some refurbished pumps available

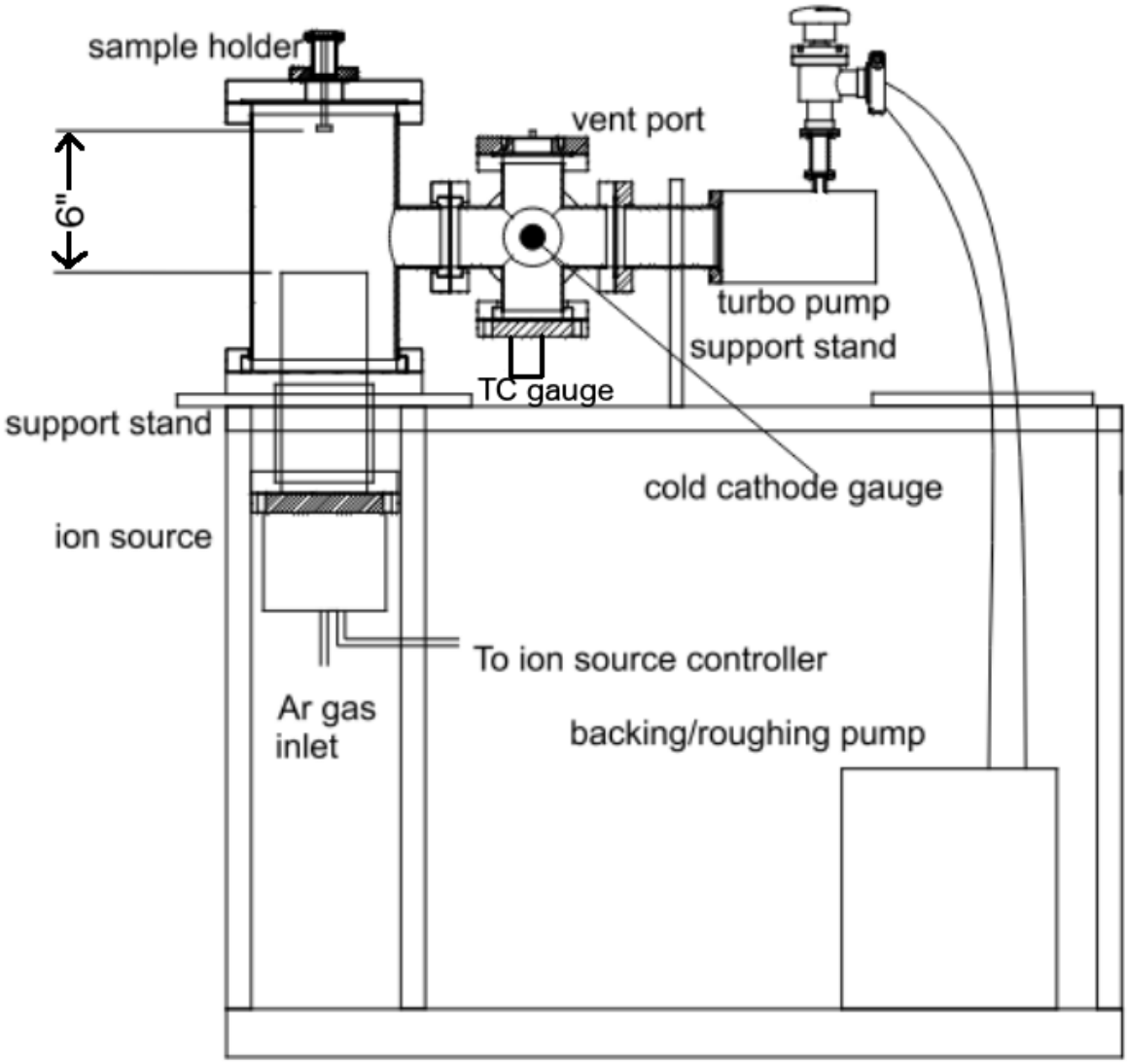

Figure 3.7. CAD drawing of the ion mill in the Northwestern Mesoscopic Physics Group cleanroom.

an ion gauge) are used for pressure measurement and monitoring of Ar gas flow. Ultra high purity Ar gas can be introduced from the back of the ion source using a needle valve. Clean N2 gas is used for venting the chamber through the vent port after use.

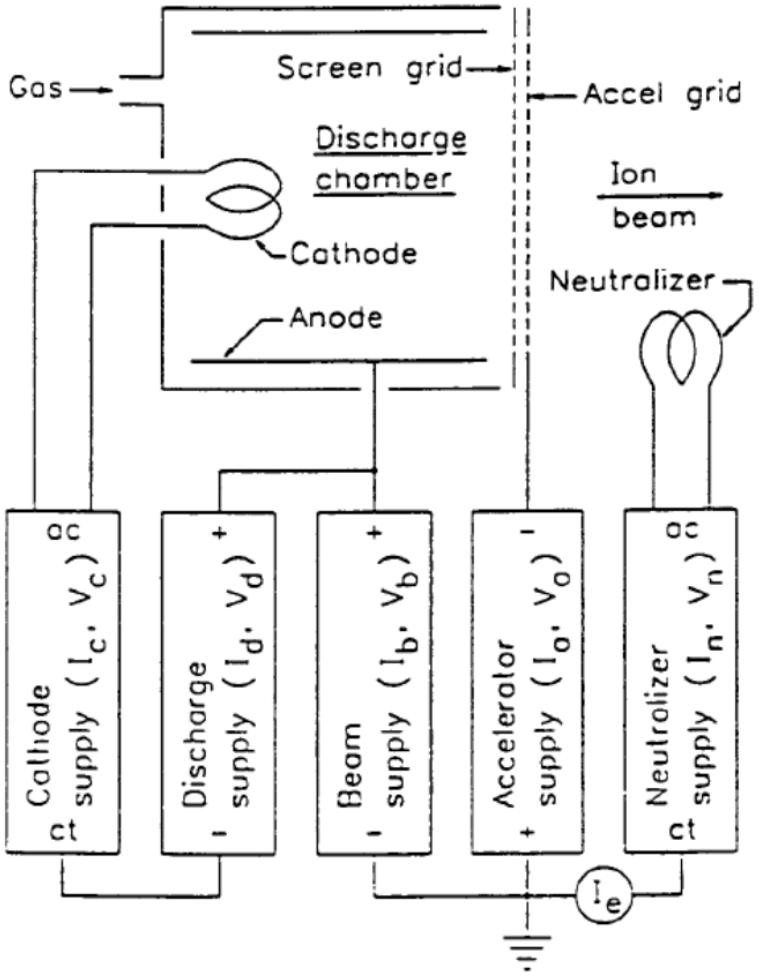

Figure 3.8. Schematic of the dc gridded ion gun. Image taken from Ref. [**138**].

Figure 3.8 shows a schematic of the ion source. An ac current through the cathode filament heats the filament to thermionically generate electrons. These electrons impinge on the Ar atoms introduced though the gas inlet of the system, ionizing them. The plasma beam is made up of these Ar ions and electrons, as I describe further. The cathode current should be able to generate enough electrons to ionize the Ar atoms and supply the required beam current. The positive discharge voltage determines the energy

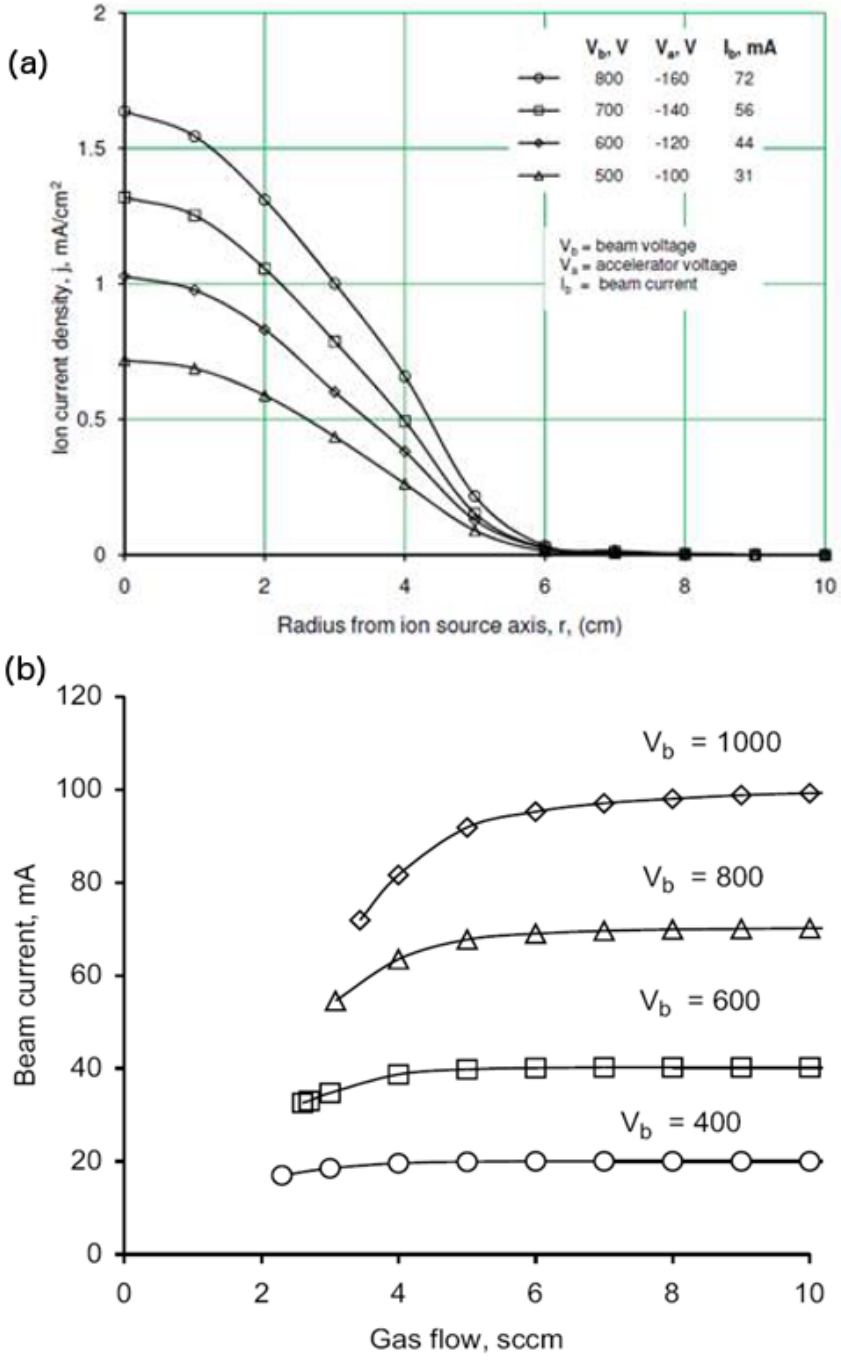

Figure 3.9. **a,** Beam current density as a function of distance from the beam axis, at a distance of 6" from the source outlet. **b,** Beam current as a function of Ar gas flow rate, for different values of beam voltage. Images from Ref. [**139**].

of the electrons emitted by the cathode and hence their ability to ionize Ar atoms, as well as the approximate potential at which singly charged Ar ions are generated in the discharge chamber. It is set to no more than 40 V, in order to minimize the occurrence of doubly charged Ar ions, since the energy of doubly charged ions would be twice the discharge potential, leading to a rapid erosion of any surfaces within the chamber which are near cathode potential. A permanent magnet helps contain the electrons and maximize probability of ionization of Ar atoms. A positive beam voltage is applied between the anode and the screen grid (which is at ground potential), which along with the negative accelerator voltage, collimates and accelerates the Ar ions out of the discharge chamber towards the sample. The beam current and the beam voltage are determined to give a reasonable etch rate while minimizing sample and resist damage, which for our LSAT/STO sample, means that the STO substrate should remain insulating, and the resist mask material should not be too difficult to strip. The neutralizer filament, heated by an ac current, emits electrons to ensure that the plasma impinging on the sample remains approximately neutral, thus avoiding sample charging and excessive beam divergence. The neutralizer current should be set equal to the beam current. The negative accelerator voltage also prevents back-streaming of electrons emitted by the neutralizer filament, but should be set to no more than 1/5th the beam voltage in order to prevent damage to the accelerator grid by Ar ions. The parameters discussed above, namely, cathode filament current, discharge voltage, beam voltage, beam current, accelerator voltage, and neutralizer emission current, can be preset according to process requirements using dials on the KSC1202 power supply/controller. On turning the discharge and beam supplies on, the other parameters are determined by a feedback system to maintain the required

preset parameters discussed above.[**138**] For the graphite gridded ion source used in our ion mill, the ion beam divergence and beam uniformity at a distance of 6" from the grids is as shown in fig. 3.9(a). For a beam voltage of 600 V, the beam is relatively uniform over a diameter of $\sim$ 2 cm. By placing the 5 mm $\times$ 5 mm sample to be milled at the center of the sample state, a uniform milling can be achieved.

Following were the specific steps in the ion milling process used:

(1) The sample, with S1813 resist protecting the areas which must remain conducting, was affixed using double sided copper tape to the stainless steel plate which is attached to the sample holder. Care must be taken to have the sample flat against the stainless steel plate, to use as small a piece of copper tape as possible, and ensure that the copper tape is not exposed to the incoming ion beam, in order to ensure uniform milling and reduce pumping time as well as contamination.

(2) The chamber was roughed while flushing the Ar gas lines with clean UHP Ar gas [15] for 10 minutes. However, in hindsight it would be more efficient to flush the Ar lines and the chamber by first filling the chamber with Ar gas and subsequently pumping it out, and repeating this a few times, rather than continuously pumping on the open Ar lines. Next the Ar flow is stopped and the system is roughed until the pressure falls below 100 mTorr. Then the turbopump is turned on, and the pressure is allowed to drop to about 10^{-7} Torr, which can take up to 3 - 6 hours, depending on atmospheric humidity.

(3) Ar gas was introduced from the back of the ion gun, as shown in Fig. 3.7, at 4 sccm. This flow rate is set by a capillary tube inserted in the Ar supply line. A pressure

[15]Ultra high purity Ar, Airgas, http://www.airgas.com

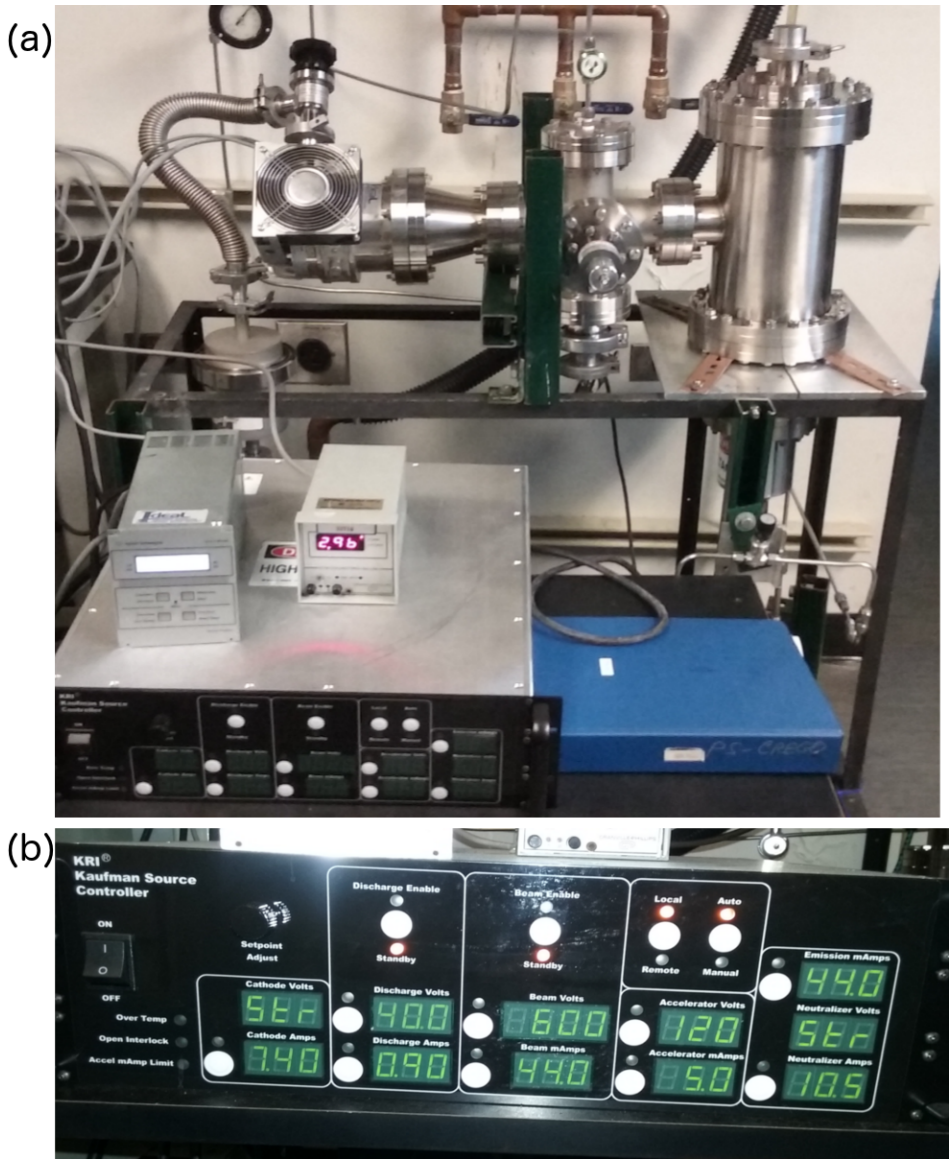

Figure 3.10. **a** Image of the ion mill setup. **b** Image of the power supply before the discharge and beam are turned on, showing the preset parameters for the process.

gauge monitors the inlet pressure of the capillary and should be set to 3 psi. A flow rate of 4 sccm is sufficient to provide enough Ar atoms for the required beam current of 44 mA, as can be seen from Fig. 3.9(b). A larger flow rate would also work, but given

the relatively small pumping power of the system, would lead to unacceptably large chamber pressures. The flow rate of 4 sccm leads to a chamber pressure of $\sim 9 \times 10^{-4}$ Torr, considering the pumping speed of the turbopump and the pumping efficiency losses due to the system geometry. This pressure should be monitored during the milling process. The following parameters were used while milling my sample:

- Cathode filament current : 7.4 A
- Discharge voltage : 40 V
- Beam voltage : 600 V
- Beam current : 44 mA
- Accelerator voltage : 120 V
- Emission current : 44 mA

As discussed in section 2.2, ion milling under certain conditions can lead to a conducting STO substrate, which would be fatal for transport experiments on STO-based 2DCGs. Hence the beam voltage and current parameters were optimized by Dr. Dmitri Dikin, a former Research Professor in our group, to ensure insulating STO. Although a beam voltage of 600 V can lead to higher energies of sputtered material which can coat the ion source surfaces, in particular, the grids and the anode, adding to down-time for maintenance, it is preferable to using lower beam voltages, which have been shown to create conducting STO substrates. For more information on the STO substrate conductivity and ion milling parameters, please refer to the work by Reagor *et al.*[**55**] and the thesis of Sam Davis.[**31**] As discussed in Chapter 2, any contamination of STO with Nb and La can also render STO conducting, hence utmost care must be taken to ensure the cleanliness of the ion milling chamber.

(4) Once the Ar pressure was stable, the power supply for the KDC40 dc gridded ion gun [16] was turned on. At this stage, one can adjust any process parameters as per one's requirements.

(5) Once the milling is done, the power supply is switched off, the Ar gas flow is stopped, and then turbopump is shut off, while the roughing valve is simultaneously closed in order to prevent back-streaming of pump oil into the system. The system should be vented with N_2 gas through the vent port only after the blades of the turbopump have stopped completely.

For the milling parameters used in this study, the etch rates for LSAT/STO and S1813 photoresist were calibrated on different trial samples of (111) STO and S1813 spun on silicon substrates, and were found to be $\sim$ 10 nm/minute, and $\sim$ 45 nm/minute, respectively. By milling for 2 minutes we ensure that LSAT and some STO is removed from areas of the sample not protected by the 1.2 $\sim$ μm thick S1813 resist. The STO substrate was insulating, overloading on a scale of 100 MΩ.

After hooking the sample up on the cryostat cold finger and before proceeding to detailed transport measurements, the resistance between the Hall bars and the back gate, the resistance between Hall bars themselves, and between any of the sample pins and the ground must be checked for any shorts. For our LSAT/STO sample, all these two-probe resistances were greater than 100 MΩ, measured using the HP34401 digital multimeter.

3.2. Measurement techniques

The properties of a conductor depend on its band structure and the scattering processes involved. Electrical transport measurements which study the differential sample

[16]Kaufman and Robinson, fort Collins, Colorado, http://ionsources.com/products/kdc-40/

resistance, $\mathrm{d}V/\mathrm{d}I$, as a function of temperature, electric gate, and magnetic field, can often help us glean important information about these material properties.

The measurements were performed at low temperatures, ranging from 4.2 K to 40 mK, since some interesting physical phenomena are revealed at these reduced energy scales. The standard four probe ac measurement technique was employed to measure longitudinal as well as transverse (Hall) resistances, using a lock-in amplifier (either PAR124 [17] or SR124[18]), and either a home-built high output impedance current source [**112**], or a modified Adler-Jackson bridge.[**112**] The total resistance of the Hall bars on the LSAT/STO sample studied in this thesis typically varied between $\sim 300\ \Omega$ and $\sim 1.8\ \mathrm{M}\Omega$ as a function of the gate voltage, and dictated the choice of the instrument used.

Home-built instrumentation amplifiers with either an AD624 op-amp,[19] which has an input impedance of $\sim 10^9\ \Omega$, or an INA110 op-amp,[20] which has an input impedance of $\sim 10^{12}\ \Omega$, were used to amplify the voltage drop across the sample. Most of the data presented in this thesis use instrumentation amplifiers with an INA110, since they are more appropriate for measuring the high impedances typical of STO-based 2DCGs, especially in the regime of negative gate voltages.

Frequency of the ac signal was typically ~ 3 Hz. The reason for choosing this frequency is discussed in the next section. The magnitude of the ac current used varied from ~ 50 nA to ~ 200 nA. The current magnitude must be chosen to get a good signal-to-noise ratio while avoiding sample heating. A Keithley 2400 source meter, which can source ± 200 V,

[17]Ametec Princeton Applied Research, http://www.ameteksi.com/
[18]Stanford Research Systems, http://www.thinksrs.com/products/SR124.htm
[19]http://www.analog.com/media/en/technical-documentation/data-sheets/AD624.pdf
[20]Texas Instruments, http://pdf.datasheetcatalog.com/datasheets

or a Keithley 230 programmable voltage source[21] which can source ±100 V were used to apply the back gate voltage. Measurements were performed on two different dilution refrigerators, an Oxford Kelvinox MX100[22] and an Oxford Kelvinox 300 [23], both of which have a base temperature of 15 mK. The MX100 allows for the application of perpendicular magnetic fields up to 3 T and parallel fields up to 1 T, while the older Kelvinox 300 allows us to go up to a perpendicular field of 12 T at liquid He temperatures. A Kepco BOP 20-50[24] power supply was used to supply current for the superconducting magnets on the MX100 dilution fridge, while a Lakeshore 622 magnet power supply[25] was used to supply larger currents up to 100 Amps for the superconducting magnet on the Kelvinox 300. HP 34401 digital multimeters were used to measure voltage drops across the sample after amplification using the home-built instrumentation amplifiers, while an HP 3458 digital multimeter[26] was used to measure voltage across the magnet sense resistor, since it has a better resolution (8½ digits) than the HP 34401 multimeter (6½ digits), thus allowing a more precise measurement of the magnetic field. Electrical noise levels were measured using an SR760 spectrum analyzer[27].

The procedure to cool the sample down on both the refrigerators, as well as the measurement technique used, has been employed by many previous generations of graduate students, and discussed in detail in past theses.[**112, 140, 141, 142, 143, 144, 30, 31**]

[21]Kiethley Instruments, https://www.tek.com/keithley
[22]Oxford Instruments, Concord, MA, https://www.oxford-instruments.com
[23]see Footnote 18
[24]Kepko, Inc., Flushing, NY, http://www.kepkopower.com
[25]Lakeshore Cryotronics, Inc., Westerville, OH, http://www.Lakeshore.com
[26]Keysight Technologies, https://www.keysight.com
[27]see Footnote 18

Here I only review aspects that require special attention in the case of LSAT/STO samples.

3.2.1. Determination of gate voltage range

As has been discussed in the previous section, the morphology of atomic terraces affects the ease of making reliable Ohmic contacts to the sample. The ac technique we use allows us to measure the components of the sample impedance Z which are in-phase as well as out-of-phase with the applied ac current. Figure 3.11(a) shows the in-phase signal, and Fig. 3.11(b) shows the out-of-phase signal as a function of V_g, at temperature $T = 40$ mK, and $f \sim 3$ Hz. One observes that especially at higher ac tickling frequencies and lower temperatures, a large out-of-phase signal develops as V_g is reduced. One must ensure that in this case, the measured in-phase signal is indeed the sample resistance.

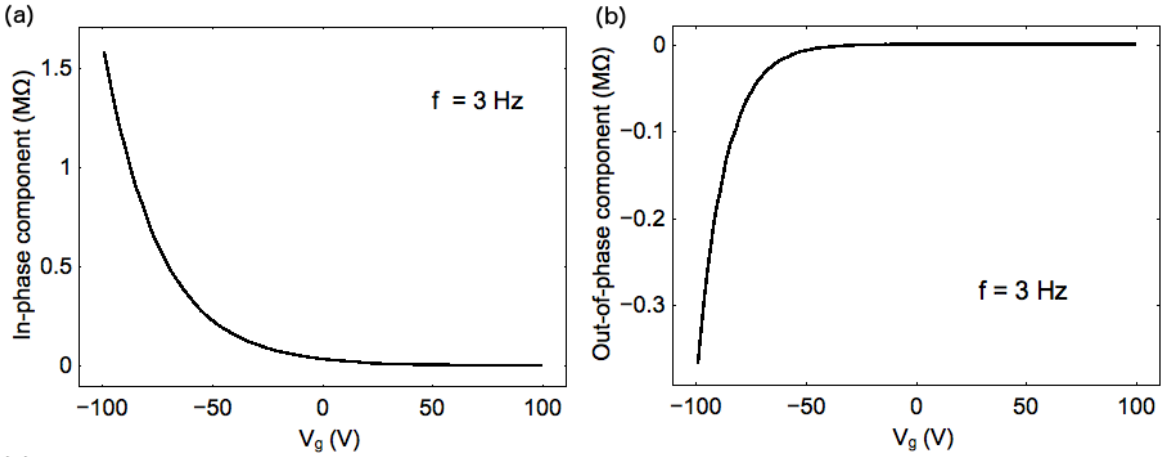

Figure 3.11. **a**, In-phase and **b,** out-of-phase components of the impedance of the Hall bar S1 aligned along the $[\bar{1}\bar{1}2]$ crystal axis as a function of V_g, at $T = 40$ mK, for an ac tickling frequency of 3 Hz.

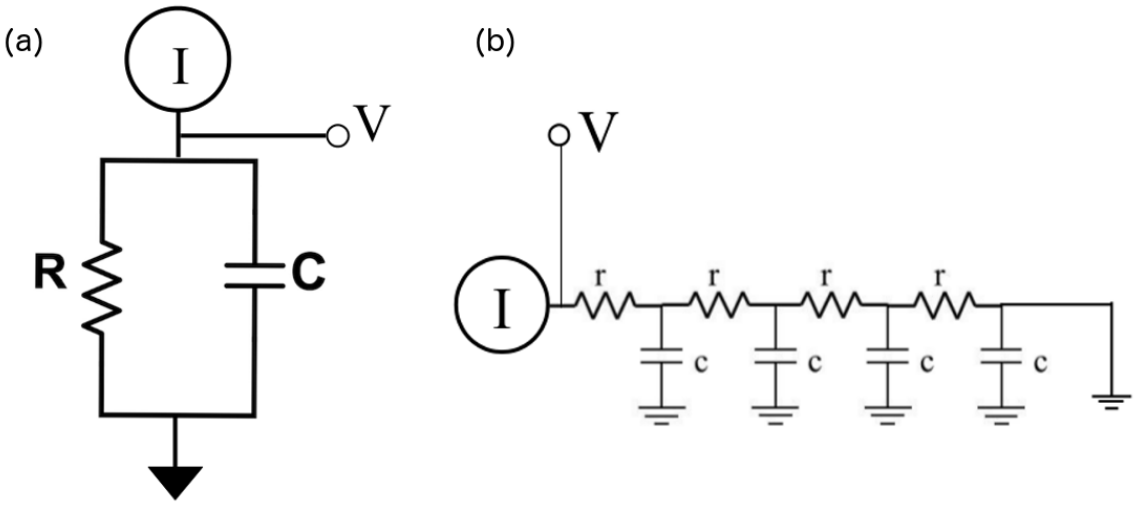

Figure 3.12. **a,** Circuit diagram for the simple model for the sample, described as a parallel combination of R and C, sourced with a constant ac current I. The voltage V is measured across the sample. **b,** Circuit diagram for the distributed model with a resistance per unit length of the sample r and a capacitance per unit length between the 2DCG and back-gate of c.

The simplest model describing this behavior is a parallel combination of resistance R and capacitance C, as shown in Fig. 3.12(a), for which the in-phase part of the sample impedance Z is given by $Z_r = R/(1 + R^2\omega^2C^2)$, and the out-of-phase part is given by $Z_i = -R^2\omega C/(1+R^2\omega^2C^2)$, where $f = \omega/2\pi$. For data obtained at a particular frequency, these equations can be inverted to obtain R and C as a function of V_g. The blue curves in Fig. 3.13(a) and (b) show R and C obtained from this simple model. The system can also be described by a distributed RC network, as shown in Fig. 3.12(b). This model describes a system with a resistance per unit length r, which is capacitively coupled to the back gate electrode by a capacitance per unit length c. For this model, the in-phase and out-of-phase components of Z are given as follows:

$$Z_{r,i} = \sqrt{\frac{R}{2\omega C}} \times \frac{\sinh\sqrt{2\omega RC} \pm \sin\sqrt{2\omega RC}}{\cosh\sqrt{2\omega RC} + \cos\sqrt{2\omega RC}}. \tag{3.1}$$

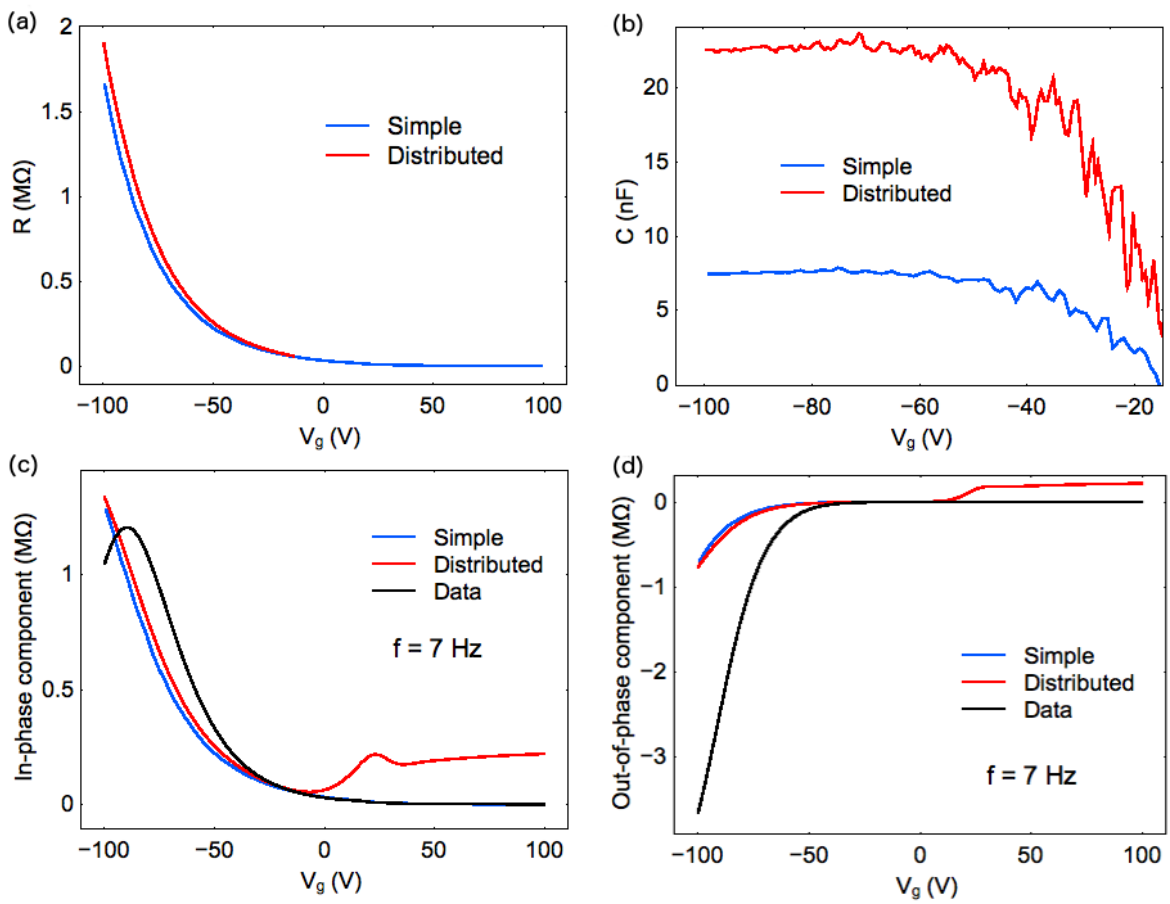

Figure 3.13. **a**, Resistance and **b,** capacitance predicted for the Hall bar S1 from the 3 Hz data shown in Fig. 3.11, using the simple parallel RC model (blue curves) and the distributed RC model (red curves) as described in the text. **c,** In-phase and **d,** out-of-phase components for the data measured with an ac tickling frequency of 7 Hz (black curves), along with predictions from the simple model (blue curves) and the distributed model (red curves).

The values of the equivalent resistance R and equivalent capacitance C can be numerically extracted from the above equations[28], and are shown by the red curves in Fig. 3.13(a) and (b). Both models are only valid for V_g less than $\sim$ -15 V, where the out-of phase components are negative, and give quite similar results. For both these models, assuming these values of R and C are independent of frequency, they can be used to predict Z_r and Z_i for data at a different frequency[29]. Figures 3.13(c) and (d) show simulated values of the in-phase and out-of-phase components of Z as a function of V_g for $f = 7$ Hz, obtained by using the 3 Hz data as described above. We see that both models correctly predict the decrease in the magnitude of the in-phase component, at higher frequencies. This means that at lower frequencies, the in-phase component is a closer approximation to the sample resistance, as compared to the in-phase component at higher frequencies. The downturn in the in-phase component is however not captured by either model. Both models also underestimate the magnitude of the out-of-phase component to a similar extent. I must note that the results of these simulations are very sensitive to initial conditions, i.e., initial guesses for the R and C values used in the MATLAB code.

The cause of this problem remains to be pinned down. In my experiments, I used f $\sim$ 3 Hz, and restricted the range of V_g to be greater than -40 V, in order to mitigate any errors introduced by the development of the out-of-phase component.

3.2.2. Drift in sample resistance

The resistance of LSAT/STO samples drifts with time after any change in V_g. This drift seems to be endemic to STO-based 2DCGs and has been widely observed. At positive

[28]The MATLAB code used for this is on Mesodisk, in the file GateVoltageCapacitanceFitting_Varada.m
[29]See footnote 28

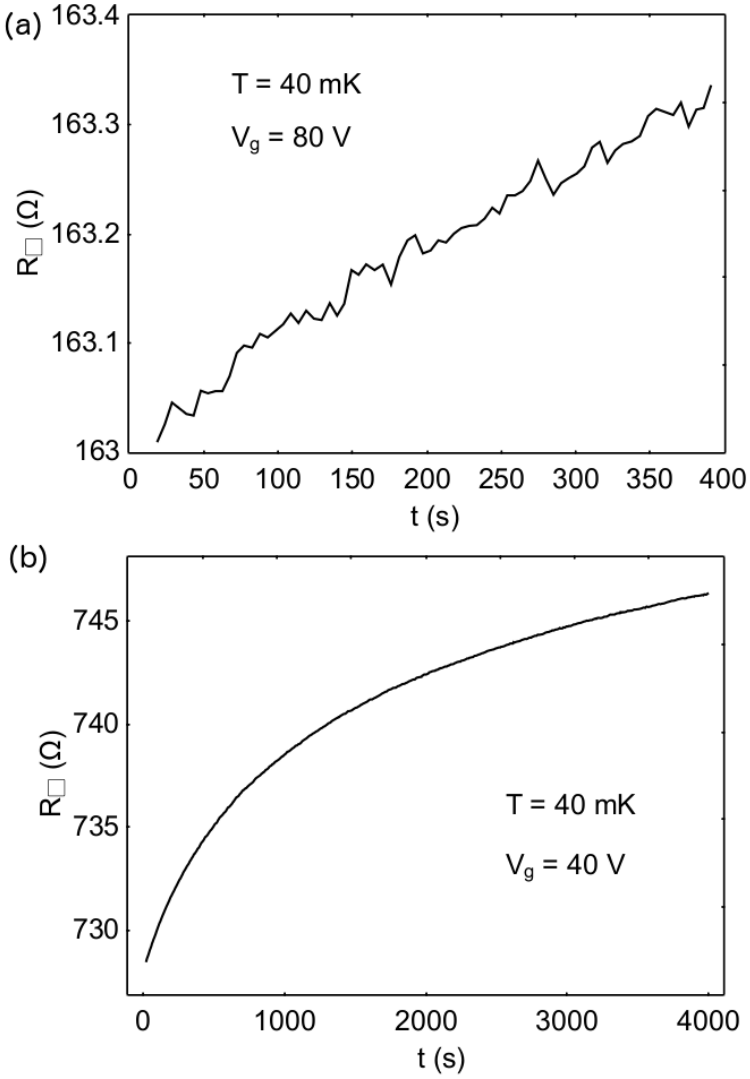

Figure 3.14. R_s vs. time at $T = 40$ mK, after changing V_g at a rate of 400 V/hr from 100 V to 80 V: **(a)**, and from 60 V to 40 V: **(b)**

values of V_g, according to the model of Biscaras *et al.*[**80**] discussed earlier in section 2.3, this can be a result of a time-dependent escape of charge carriers over the interfacial potential well confining the 2DCG. However, their model does not explain the drift at negative values of V_g for which according to their model there is no escape of carriers

over the interfacial potential well. One reason which might explain the drift observed at negative voltages is the slow diffusion of defects in the crystal which can locally modify the polarization of STO, as discussed in section 2.2 and 2.3. At the lower carrier densities characteristic of the low V_g regime, Coulomb interactions between charged defects may become more important and compete with the tendency of certain kinds of defects like oxygen vacancies to cluster, creating a more glassy environment for the 2DCG and slowing the approach of the defect positions to equilibrium. This might be one of the reasons that the drift is more pronounced at lower T and lower values of V_g where the sample is more resistive. A detailed time dependence study of the drift as a function of V_g, T, as well as different defect concentrations can help provide more insight into this behavior.

The drift poses a measurement challenge, since it makes data-taking very time consuming, aside from increasing liquid He requirements considerably. Figure 3.14 shows sheet resistance of a Hall bar on the (111) LSAT/STO sample discussed in this thesis, oriented along $[\bar{1}\bar{1}2]$ direction, as a function of time, at $T = 40$ mK, and at two different values of V_g, after changing V_g at a rate of 400 V/hr, starting 20 V above the particular value of V_g. In order to make reliable measurements in reasonable time, I waited until the drift in resistance reduced to within 1% of the absolute resistance over a period of time, which ranged from $\sim$ 30 minutes at large positive values of V_g, to $\sim$ 2 hours for the most negative values of V_g, in order to take data. A consistent protocol was followed while changing V_g as well, always going from higher to lower values at a constant rate.

In the next chapter, I discuss the results of my experiments on (111) LSAT/STO based on the background presented in Chapter 2 and the techniques described in Chapter 3.

CHAPTER 4

Results

In this chapter I will describe the results of my measurements of the dependence of sample transport properties on V_g, T, B, and a magnetic field applied in the plane of the 2DCG, along the current direction, $B_{||}$. All the measurements reported were performed on four Hall bars, which I will refer to as S1, S2, S3, and S4, fabricated on a single chip of (111) LSAT/STO. The Hall bars S1 and S3 were oriented along the $[\bar{1}\bar{1}2]$ crystal direction whereas the Hall bars S2 and S4 were oriented along the $[1\bar{1}0]$ crystal direction, as shown earlier in Fig. 3.3. The measurement configuration was as shown in Fig. 4.1. Data were collected from four different cool-downs on two different dilution refrigerators. For STO-based 2DCGs, thermal cycling between room temperature (RT) and cryogenic temperatures is known to cause variations in the sheet resistance R_s of the sample. For the sample described in this thesis, I observed a variation in R_s of up to 25% between cool-downs on any given Hall bar, although the overall behavior was reproducible for all transport properties.

This chapter is organized in the following sections: (i) Temperature dependence and gate voltage dependence data which highlight the relatively clean nature of the sample, the nature of the potential well in which the 2DCG resides, and the lack of systematic anisotropy in transport properties related to the crystal axes, (ii) Transverse and longitudinal MR measurements in perpendicular fields up to 10 T at 4.2 K and 40 mK, which

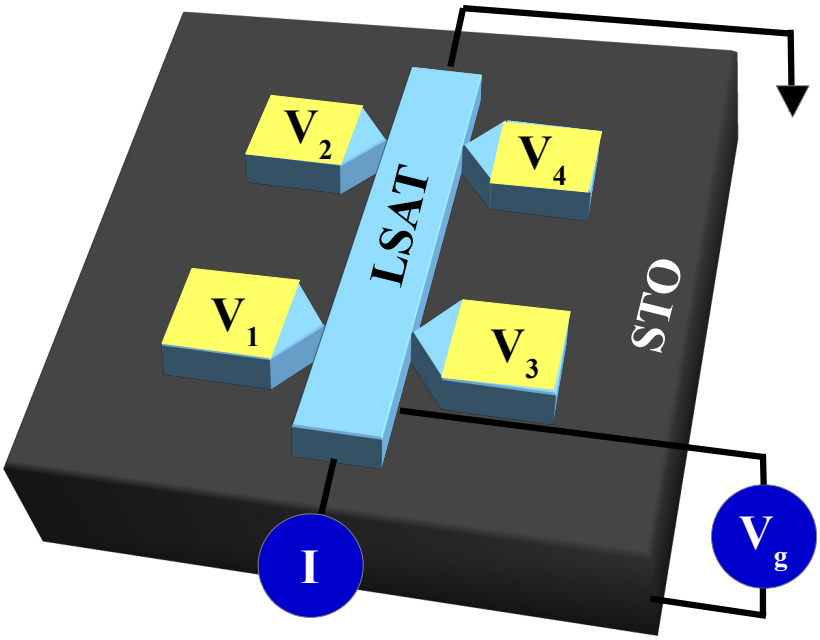

Figure 4.1. Schematic of the measurement setup. The Hall bar is current biased with an ac tickling current I. Back gate voltage V_g is applied between the back of the STO substrate and the 2DCG. Longitudinal voltage drops are measured between voltage probes $\mathbf{V}_1$ - $\mathbf{V}_2$ or $\mathbf{V}_3$ - $\mathbf{V}_4$, while Hall voltages are measured between $\mathbf{V}_1$ - $\mathbf{V}_3$ or $\mathbf{V}_2$ - $\mathbf{V}_4$.

point to the multiband nature of transport, and the presence of hole-like carriers coexisting with electron-like carriers. (iii) Longitudinal MR measurements in perpendicular fields at $T = 4.2$ K, showing the evolution of a strong SOI as electron concentration is decreased. (iv) Longitudinal MR data at millikelvin temperatures and more positive values of V_g, which show evidence of weak localization/antilocalization. I show that given the variety of coexisting and competing phenomena that can affect magnetotransport in the system, care must be taken in interpreting the results. I analyze the data in terms of weak localization/antilocalization, magnetic scattering, electron-electron interaction contributions, and classical MR. (v) Longitudinal MR measurements in perpendicular and

parallel fields at millikelvin temperatures, which show that as V_g and hence the electron concentration is decreased, concomitant with an increase in SOI, an ordered ferromagnetic state emerges, characterized by a hysteretic MR.

4.1. Temperature and gate voltage dependence of resistance

We know from the discussion in Chapter 2 that STO-based 2DCGs show hysteresis as a function of V_g, likely due to a combination of carriers escaping over the interfacial potential well which hosts the 2DCG, and a slow drift of defects in STO. In order to characterize sample properties at different values of V_g it is important to understand how the sheet resistance R_s and this hysteresis vary as a function of temperature and the history of changes in V_g.

Figure 4.2(a) shows R_s as a function of V_g at room temperature (RT) for the Hall bar S1 oriented along the $[\bar{1}\bar{1}2]$ crystal direction. The data were collected during the initial sweep of V_g at the rate of 400 V/hour. The trace marked '1' shows the first sweep from $V_g = 0$ V to $V_g = 100$ V, and the subsequent sweeps for decreasing and increasing values of V_g are marked by arrows. We see an overall change in R_s of ~ 1.3 % between V_g = -100 V and +100 V, a noticeable hysteresis in R_s as a function of V_g, and a small tendency for R_s to drift to higher values, demonstrated by the fact that the value of R_s after V_g is swept back to 0 V is slightly higher. Figure 4.2(b) shows data obtained from a similar measurement after cooling to $T = 77$ K at $V_g = 0$ V. We find that the behavior of R_s as a function of V_g at $T = 77$ K is markedly different from that at RT. After the initial sweep from $V_g = 0$ V to $V_g = 100$ V, and back to 0 V, we observe an irreversible increase in R_s of $\sim 12.5\%$ over its initial value at $V_g = 0$ V and $T = 77$ K before the gate sweep. After this,

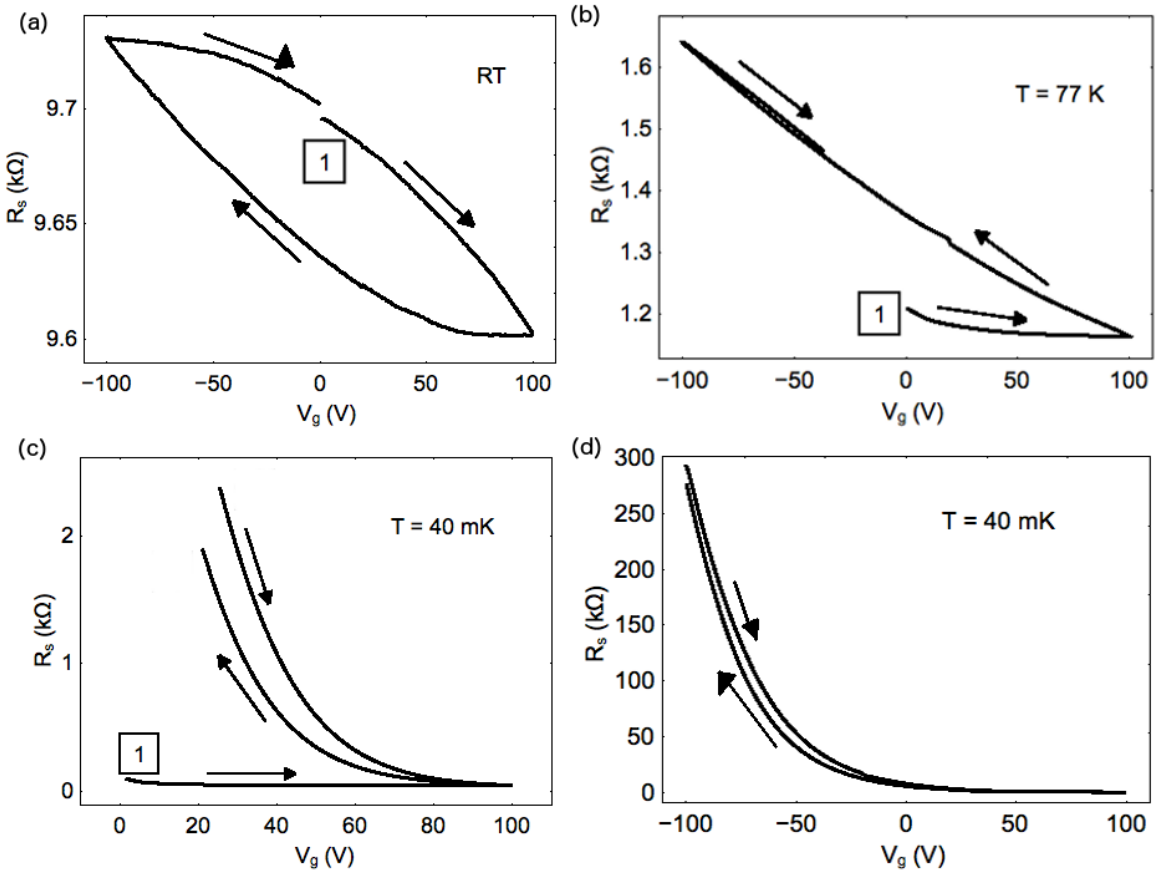

Figure 4.2. Initial R_s vs. V_g sweeps performed on the Hall bar S1, **a**, at RT, **b,** at $T = 77$ K after cooling the sample to 77 K at $V_g = 0$ V, and **c**, at $T = 40$ mK after cooling the sample to 40 mK at $V_g = 0$ V. **d,** R_s vs. V_g at $T = 40$ mK, after the stabilization of the hysteresis loop.

the original value of R_s can be recovered only after warming to RT. The overall change in R_s over the whole range of V_g at $T = 77$ K is also larger, ~ 40 %. This behavior is even more striking at $T = 40$ mK, as can be seen from Fig. 4.2(c), which shows an irreversible increase in R_s at $V_g = 0$ V by more than a factor of 20 after cooling to $T = 40$ mK at $V_g = 0$ V, and after the initial sweep of V_g from 0 V to 100 V. The data in Fig. 4.2(c) is cut off as the lock-in amplifier overloaded. After fixing the sensitivity of the lock-in amplifier,

the R_s was seen to change by a factor of ~ 300 over the full range of V_g as shown by Fig. 4.2(d). Note that one must sweep V_g over the whole range at least about ten to twenty times in order to get the R_s vs. V_g hysteresis loop to retrace over itself.

These data lend credence to the theory of Biscaras *et al.* [**80**] discussed in section 2.3, which states that the Fermi level of the 2DCG lies intrinsically close to the top of the interfacial potential well which hosts the 2DCG, and for positive values of V_g, the change in the shape of the potential well causes electrons to spill irreversibly out of the potential well, giving rise to an irreversible increase in R_s, and setting a limit to the electrostatic doping of the 2DCG with electrons. The electrons which spill out of the well get trapped at defects which in the bulk of STO, have activation energies of up to a few meV, or activation temperatures of tens of Kelvins, as discussed earlier in Chapter 2. Hence the irreversible loss of charges over the potential well is much more pronounced at lower temperatures. However, the large change in R_s over the full range of V_g is not explained by a variation in carrier density n alone, as n is only estimated to vary by a factor of less than 5 by earlier experiments on (001) as well as (111) oriented LAO/STO,[**26, 74, 86, 91**] and also by estimates of n from my own data, as we shall discuss later. It is more likely that changes in carrier mobilities and scattering times, rather than changes in n, that lead to the observed drastic changes in R_s as a function of V_g.

From Fig. 4.2(a), (b), and (c), we can also see that R_s at $V_g = 0$ V, before sweeping V_g, decreases by a factor of ~ 10 between RT and 77 K, and by a factor of ~ 100 between RT and 40 mK. This high residual resistance ratio (RRR) points to the relative cleanliness and quality of the interface hosting the 2DCG. However, the RRR irreversibly decreases substantially after sweeping V_g to high positive values. Figure 4.3(a) shows R_s vs. T

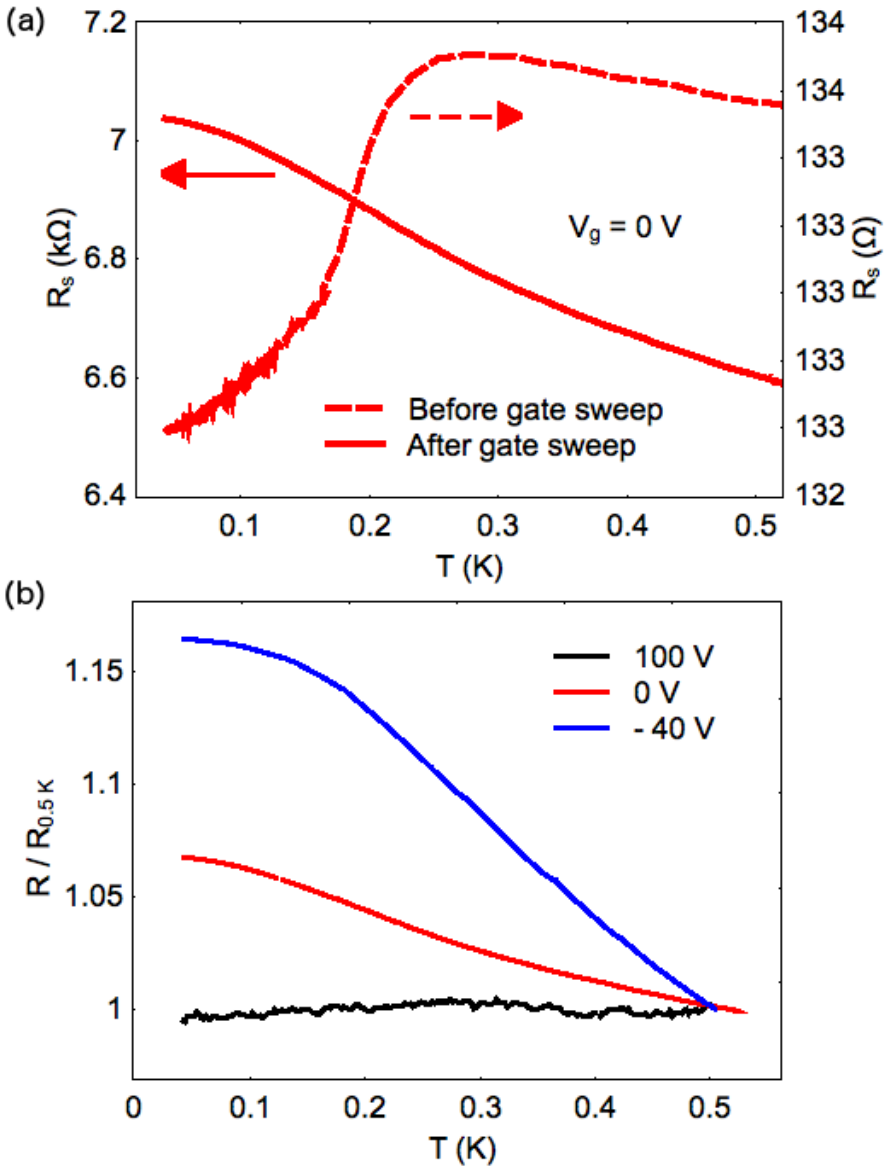

Figure 4.3. **a**, R_s vs. T at $V_g = 0$ V for the Hall bar S1, before sweeping V_g between 100 V and -40 V a few times (dashed curve), and after (solid curve). **b**, R_s, normalized to its value at $T = 0.5$ K, vs. T, at $V_g = 100$ V, 0 V, and -40 V, for the same Hall bar as above, after stabilization of the R_s vs. V_g hysteresis loop.

data for the Hall bar S1 at $V_g = 0$ V, before and after sweeping V_g from 0 V to 100 V, and then between 100 V and -40 V a few times until the R_s vs. V_g hysteresis loop stabilizes, and finally decreasing V_g back to 0 V from 100 V. It is evident that the change in the RRR caused by the gate sweep also changes the low temperature variation of R_s with T. Instead of a small decrease in R_s below $T \sim 250$ mK for data taken before the gate sweep, we see an increase in R_s with decreasing T, followed by a tendency towards saturation in R_s below $T \sim 100$ mK, for data taken after the gate sweep. Figure 4.3(b) shows the normalized R_s vs. T data for $V_g = 100$ V, 0 V, and -40 V, obtained after stabilization of the R_s vs. V_g hysteresis loop. The trace for $V_g = 100$ V shows a slight decrease in R_s below about 250 mK, whereas the traces for $V_g = 0$ V and - 40 V show a tendency to increase and then saturate at the lowest temperatures. In STO-based 2DCGs, many different mechanisms can contribute towards these variations in R_s vs. T at low temperatures, as discussed in Chapter 2. Hence we will eschew attempting to fit the R_s vs. T data to particular theories, and proceed with analyzing the MR data which can reveal more information about the system.

From this point forward the range of V_g was restricted to be greater than -40 V, as discussed in section 3.2. It was demonstrated by Davis *et al.* [**86**] that if V_g is swept extremely slowly over a period of days, the forward and reverse traces of R_s as a function of V_g converge towards the average value of R_s for the forward and reverse traces. Figure 4.4 shows the averaged R_s vs. V_g at $T = 40$ mK for all four Hall bars on my sample, two aligned along the $[\bar{1}\bar{1}2]$ crystal direction, and the other two along the $[1\bar{1}0]$ crystal direction. We see that the resistances of the Hall bars at any given value of V_g can differ by up to 50 %, as expected due to the inherently inhomogenous nature of STO-based 2DCGs.

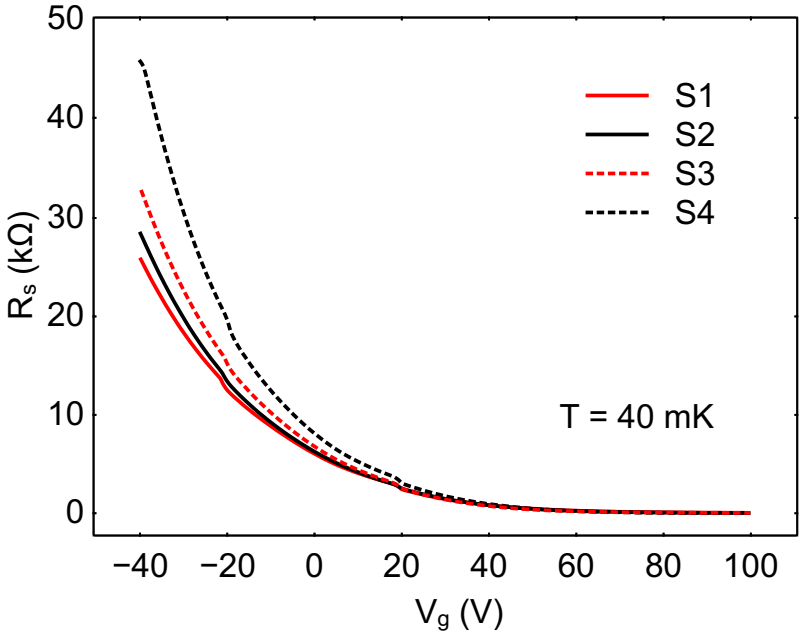

Figure 4.4. R_s (averaged over up and down gate voltage sweeps) vs. V_g of all four Hall bars after sweeping V_g between -40 V and 100 V, at 40 mK, showing absence of systematic anisotropy between crystal axes. The dashed and continuous traces in red are data for two Hall bars oriented along the $[\bar{1}\bar{1}2]$ crystal axis, whereas the dashed and continuous traces in black are data for the two Hall bars oriented along the $[1\bar{1}0]$ crystal axis, as shown in Fig. 3.3.

However, no systematic anisotropy based on crystalline direction is observed. This lack of systematic anisotropy is in contrast to the behavior observed in (111) LAO/STO, where the resistance measured along the $[1\bar{1}0]$ direction is always greater than the resistance measured along the $[\bar{1}\bar{1}2]$ direction, by as much as a factor of 5 at the lowest values of V_g.[**31**]. As noted earlier, one of the significant differences between the LAO/STO and LSAT/STO systems is the greater strain at the LAO/STO interface, suggesting that this strain may be responsible for the observed lack of systematic anisotropy in (111) LSAT/STO. However, it is also possible that similar to what is observed in (111)

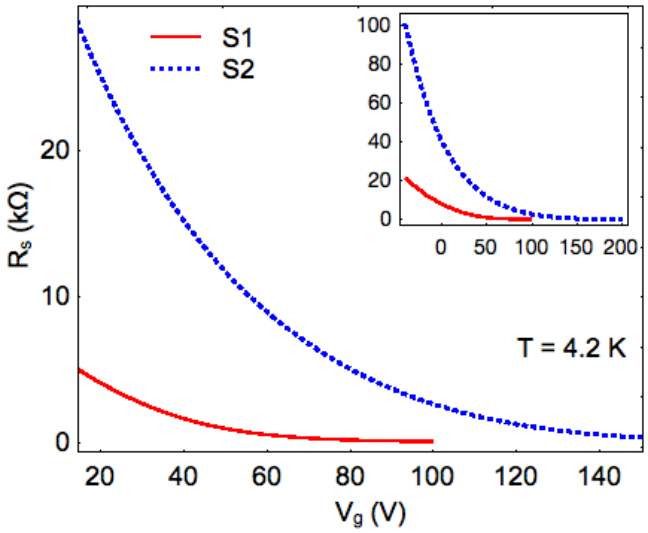

Figure 4.5. R_s, averaged over up and down-sweeps of V_g for the Hall bar S1 and the Hall bar S2 as a function of V_g, at $T = 4.2$ K. The main figure shows the R_s vs. V_g traces over a smaller range of V_g, whereas the inset shows the traces over the full range of V_g.

LAO/STO, systematic anisotropy might become evident in the (111) LSAT/STO sample if it is tuned to higher values of R_s by for example, annealing in an oxidizing environment to reduce oxygen vacancies.[**21**]

On the basis of this observed lack of systematic anisotropy in my sample, in the rest of this chapter I will present MR data mainly on Hall bar S1, oriented along the $[\bar{1}\bar{1}2]$ crystal direction, obtained from various different cooldowns, and from a single cooldown on Hall bar S2, oriented along the $[1\bar{1}0]$ crystal direction. The measurements reported here on S1 were made in the gate voltage range of 100 V to -40 V, while the measurements reported on S2 were made in the gate voltage range of 200 V to -40 V, unless specified otherwise. Figure 4.5 shows R_s vs. V_g data for two representative measurements on S1 and S2 over the different ranges of V_g, at $T = 4.2$ K. Note that higher is the most positive

value of V_g used, larger is the sample resistance at any given value of V_g, as shown in Fig. 4.5. Measurements on other Hall bars and other cooldowns yielded qualitatively similar results, consistent with the inhomogeneous nature of the sample.

4.2. High field magnetoresistance

In this section, we will focus on the Hall data and the contributions to the MR of the Hall bar resulting from the classical orbital effects, $\Delta R_{cl}(T, B)$, as well as the SdH effect, $\Delta R_{SdH}(T, B)$, on the basis of the discussion in Section 2.4.

The first clues to the band structure, carrier densities and carrier mobilities come from analyzing the transverse Hall resistances of the Hall bar at different values of V_g. Similar to earlier experiments on STO-based 2DCGs,[**30, 31**] I found that the raw R_{xy} vs. B traces were offset al.ong the R_{xy} axis. The magnitude of the offset increased with decreasing V_g or equivalently, increasing R_s, as shown in Fig 4.6. Although a small offset in the position of the Hall probes can lead to a contribution of the longitudinal MR to the Hall signal, and thus give an offset in the Hall signal increasing in magnitude with R_s, such an effect would lead to a Hall offset varying linearly with R_s. This is not the case in my sample, or in other LAO/STO samples, to the best of my knowledge. The presence of a non-zero Hall voltage even at 0 field has been reported earlier and ascribed to an anomalous Hall effect due to magnetic scattering,[**145**] or the presence of nematic order in some cuprate superconductors.[**146**] However, the origin of these offsets in STO-based 2DCGs is unclear at this time. I antisymmetrized my Hall data to remove these offsets in order to enable data analysis in terms of the two-band model discussed in Chapter 2, as is widely done in the case of STO-based 2DCGs.

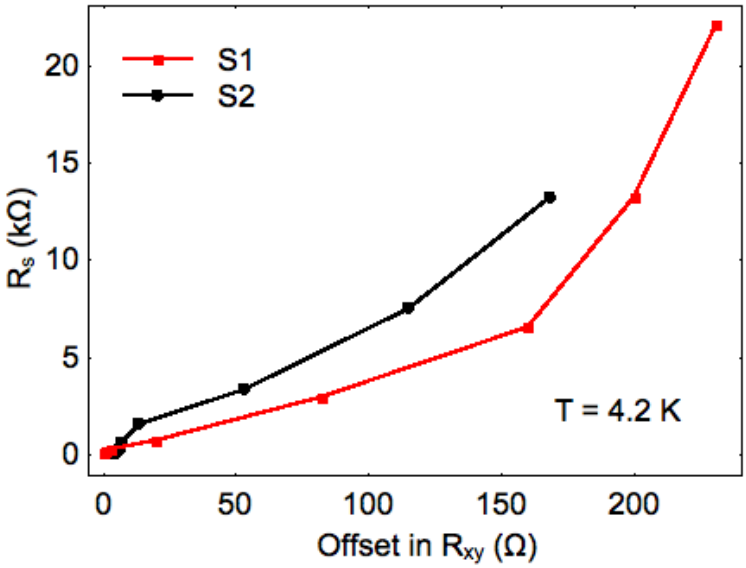

Figure 4.6. R_s for the Hall bar S1 (red squares) and the Hall bar S2 (black circles), plotted as a function of the offset in R_{xy} at $B = 0$, for various values of V_g from 100 V to -40 V, at $T = 40$ mK. V_g was varied from 100 V to -40 V for both sets of data.

Figures 4.7(a) and (b) show the antisymmetrized transverse Hall resistance R_{xy} at T = 4.2 K for various values of V_g for the Hall bar S1 and S2 respectively, offset al.ong the vertical axis for clarity. The data are from two different cooldowns, with two different ranges of the variation of V_g: for S1, V_g was varied between 100 V and -40 V, while for S2, V_g was varied between 200 V and -40 V. The slope of the R_{xy} vs. B traces was positive for all values of V_g. Knowing the direction of the applied B field as well as the polarity of the voltage probes used to measure R_{xy} is crucial in determining whether this corresponds to electron-like or hole-like carriers. The field direction was determined by using a Hall probe underneath the Oxford Kelvinox 300 dilution refrigerator when the magnet was running, and indicated the predominance of electron-like carriers at all values of V_g studied. At higher values of V_g, nonlinearities appear in the R_{xy} vs. B traces: for

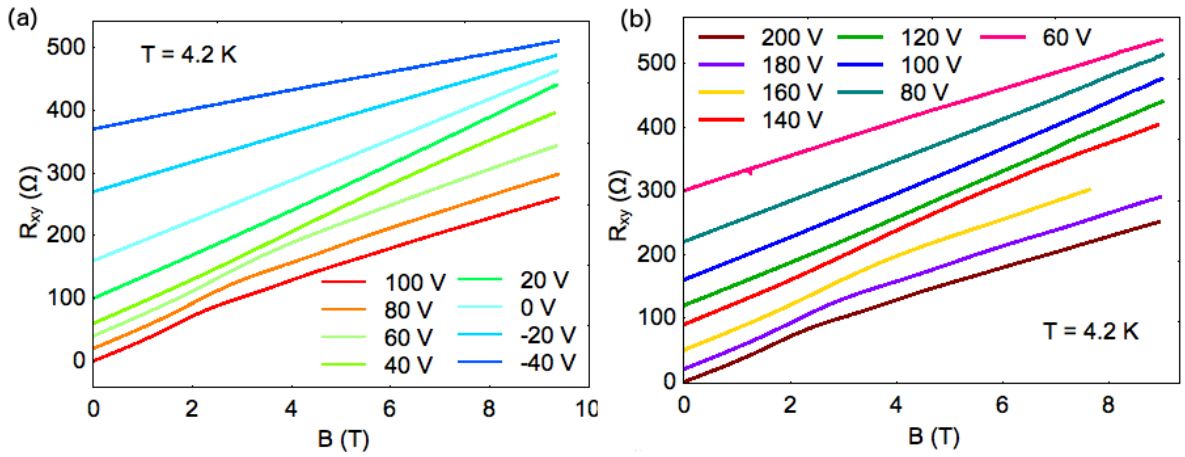

Figure 4.7. Hall resistance for various values of V_g at $T = 4.2$ K **a,** for the Hall bar S1, and **b,** for the Hall bar S2. Data have been antisymmetrized to remove small offsets in R_{xy} at $B = 0$. Data are also displaced along the vertical axis for clarity.

example, in Fig. 4.7(a), we observe a change in slope of the Hall response of the Hall bar S1 at $B \sim 2.5$ T for $V_g = 100$ V. The field at which this change in slope occurs becomes larger as V_g is decreased, and for $V_g \leq 20$ V, the Hall response appears to be nearly linear within the field range used. Nonlinearities are observed in the Hall response of the Hall bar S2 for $V_g \geq 120$ V, as can be seen in Fig. 4.7(b), while a linear Hall response emerges at smaller values of V_g. Note that the sheet resistance for S1 was ~ 4.3 kΩ at $V_g = 20$ V, whereas the sheet resistance for S2 was ~ 1.1 kΩ at $V_g = 120$ V, i.e., both Hall bars had R_s of about the same order at the value of V_g where the transition from nonlinear to linear behavior occurred.

The transition from nonlinear to linear Hall effect is similar to what is observed in the case of (001) STO based systems.[**74, 133**] As discussed in Chapter 2, this behavior has been interpreted as a Lifshitz transition, from multi-carrier transport involving the $d_{yz,zx}$ bands in addition to the low energy d_{xy} bands, to single carrier transport when

electrons are depleted from the higher energy bands and only carriers from the low-energy d_{xy} bands participate in transport. The nonlinear Hall effect observed in the (111) LSAT/STO sample at large positive values of V_g can also be similarly interpreted as being due to multiband transport, as will be demonstrated later.

However, in the case of the (111) LSAT/STO sample under study, we can infer the presence of multiple kinds of carriers even at the lowest values of V_g, similar to what has been observed for (111) LAO/STO samples. A model with only electron-like carriers cannot be the complete picture, especially for low values of V_g, as we shall see from studying the variation in the high field Hall coefficient R_H as a function of V_g, presented in Fig. 4.8(a) and (b). In the simple two-carrier model typically used for analyzing these data, as described in Section 2.4 of Chapter 2, at low magnetic fields, R_H is a function of the mobilities and the densities of both types of carriers, but in the limit of $B \to \infty$, it is determined only by the total carrier density, $R_H = -1/e(n_1 + n_2)$. Hence the variation of the high field R_H with V_g allows us to get a qualitative understanding of the dependence of the charge density on V_g.

Figure 4.8(a) shows the values of $R_H = -dR_{xy}/dB$ at zero-field and high field ($B \sim 9$ T) as a function of V_g, for the Hall bar S1. The values of R_H are obtained from the derivatives of R_{xy} with respect to B, as shown in Fig. 4.9. The transition from a nonlinear to linear Hall effect as V_g is decreased is clearly visible from the derivatives. For $V_g = 100$ V and 80 V, the derivatives also show evidence of oscillatory behavior, which we will later relate to SdH oscillations. For $V_g \geq 20$ V, the magnitude of the high-field R_H for the Hall bar S1 decreases with increasing V_g as can be seen from Fig. 4.8(a). This behavior is expected for a system in which the density of electrons increases with

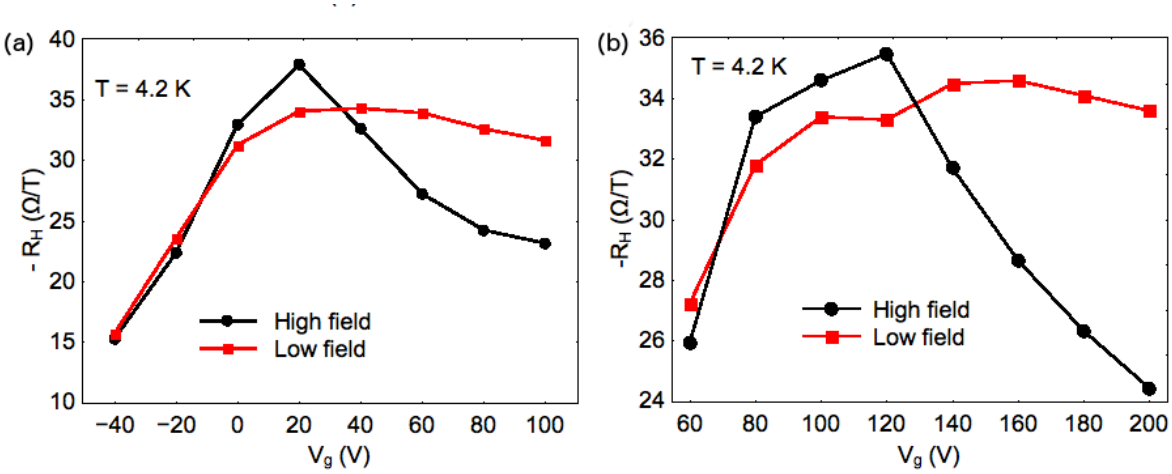

Figure 4.8. **a,** Low field (red squares) and high field (black dots) Hall coefficients for data shown in Fig. 4.7(a), taken at 4.2 K on Hall bar S1. The low field and high field values correspond to values of the derivative of the Hall resistance (shown in Fig. 4.9) with respect to B, at $B = 0$ and 9 T, respectively. **b,** Low field and high field Hall coefficients for the Hall data shown in Fig. 4.7(b), for the Hall bar S2.

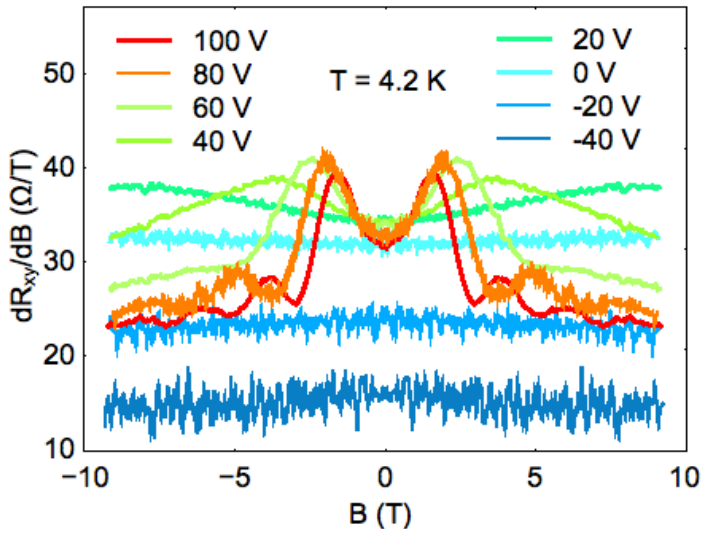

Figure 4.9. For the data shown in Fig. 4.7(a), derivatives of R_{xy} with respect to B for different values of V_g at $T = 4.2$ K.

increasing V_g. In contrast, for $V_g \leq 20$ V the magnitude of the high-field R_H *decreases* as V_g is reduced, inconsistent with the presence of only electron-like carriers in the 2DCG. As shown by Davis *et al.*,[**86**] in their (111) LAO/STO samples, such a trend in R_H can be explained by the simultaneous presence of holes and electrons participating in transport, especially at low values of V_g. It is likely that this explanation holds for the present (111) LSAT/STO sample as well. Below $V_g \sim 20$ V, the zero-field and high-field values of R_H begin to coincide, reflecting the fact that R_{xy} is linear over the entire range of field studied. Although this linearity has been interpreted as an indication of single-band transport in (001) LAO/STO systems, it is clearly not the case in the (111) LSAT/STO sample studied, as in other (111) STO-based 2DCGs. Electrons dominate transport over the entire range of V_g, however, holes also begin to play a role in transport at low values of V_g.

Figure 4.8(b) shows similar data for the Hall bar S2, corresponding to the R_{xy} vs. B traces in Fig. 4.7(b). Again, the transition from nonlinear to linear Hall effect is seen to occur below $V_g \sim 120$ V, accompanied by the telltale signs of the presence of hole-like carriers, as suggested by the variation of R_H with V_g.

I fit the R_{xy} vs. B data shown in Fig. 4.7(a) in different regimes of V_g to demonstrate the feasibility of the scenario described above. Based on the expected band structure from tight-binding approximations ignoring SOI effects on (111) oriented STO-based interfaces and surfaces, as discussed in Chapter 2, one expects the Ti t_{2g} manifold at the interface to be split into an a_{1g} band and doubly degenerate e'_g bands. Within resolution limits, ARPES studies show the presence of three degenerate bands, two with one effective mass,

and the third with a different effective mass, as discussed in section 2.3 earlier. Consequently, as a first approximation at higher values of V_g where hole-like carriers seem to have negligible effect as discussed above, it is reasonable to describe the Hall data in terms of a two-electron band model with two different densities n_1 and n_2, and two different mobilities μ_1 and μ_2. Figure 4.10 shows fits to a two-electron model according to Eqn. 2.3, for the R_{xy} vs. B data from Fig. 4.7(a), at V_g = 100, 80, 60, and 40 V. Table 4.1 shows the fit parameters obtained.

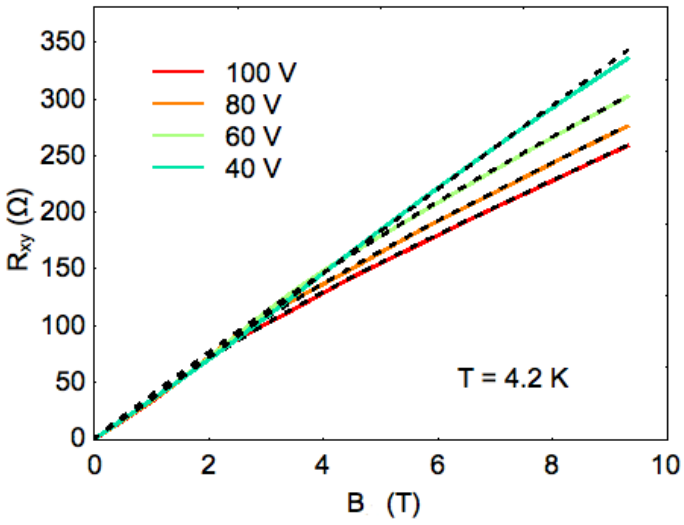

Figure 4.10. Hall data for the Hall bar S1 at 4.2 K, for four different values of V_g where we expect mainly electron-like carriers. The dotted lines are fits to Eqn. 2.3. Table 4.1 gives the values of fit parameters.

Figure 4.11 shows the R_{xy} vs. B data from Fig. 4.7(a), at V_g = 20 V, fit to Eqn. 2.3, assuming one electron-like and one hole-like carrier, while the inset shows a linear fit to the data, assuming a single electron-like carrier. The fit parameters are specified in Table 1. We see that the data fits well to both models within the range of B explored in this measurement. The non-linearity of the two-band fit is only significant at larger

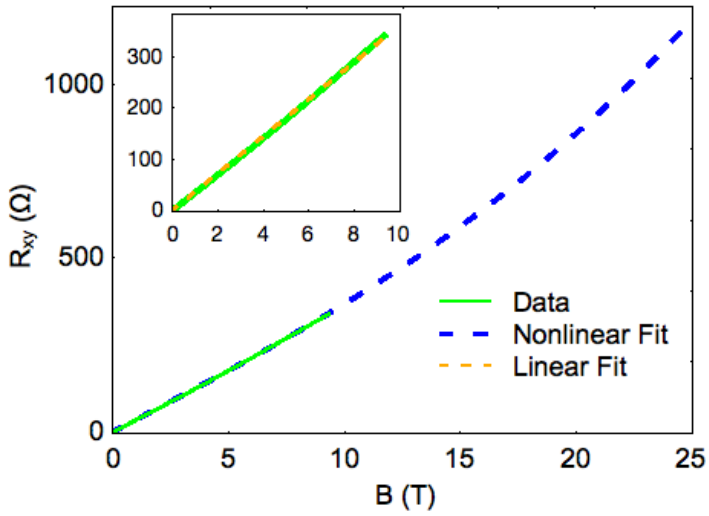

Figure 4.11. Hall data for the Hall bar S1 at $T = 4.2$ K, for $V_g = 20$ V, fit to a two-band model with electron as well as hole carriers present, and in the Inset, fit to a single electron band model.

V_g (V)	n_1 (10^{13}/cm^2)	μ_1 (cm^2/V.s)	n_2 (10^{13}/cm^2)	μ_2 (cm^2/V.s)
100	1.84	4520	0.64	1495
80	1.76	2740	0.56	1443
60	1.7	1162	0.5	1250
40	1.6	120	0.4	950
20 (two-band)	0.1	680	(holes) 0.017	270
20 (single-band)	1.7	170	NA	NA

Table 4.1. Table showing values of carrier densities and mobilities extracted from two-band fits to the R_{xy} vs. B data at $T = 4.2$ K for the Hall bar S1, at $V_g = 100$ V, 80 V, 60 V, and 40 V, assuming two electron-like carriers, and for $V_g = 20$ V, assuming an electron-like and a hole-like carrier, as well as a single electron-like carrier.

field values. This illustrates that it is indeed possible to interpret the Hall data at low values of V_g in terms of a two-band model with both electrons and holes present. It is important to note that these fit parameters from Table 4.1 are not unique, given that they are obtained from fits to two equations in four variables, namely, $R_{xy} = F_1(n_1, n_2, \mu_1, \mu_2)$ and $R_s = F_2(n_1, n_2, \mu_1, \mu_2)$.

Irrespective of the exact values of the fit parameters, the Hall data, especially the variation of R_H with V_g, demonstrate that multiple electron-like carriers dominate transport at higher values of V_g, whereas hole-like carriers start becoming important in the range of low values of V_g, although overall transport is still predominantly due to electrons.

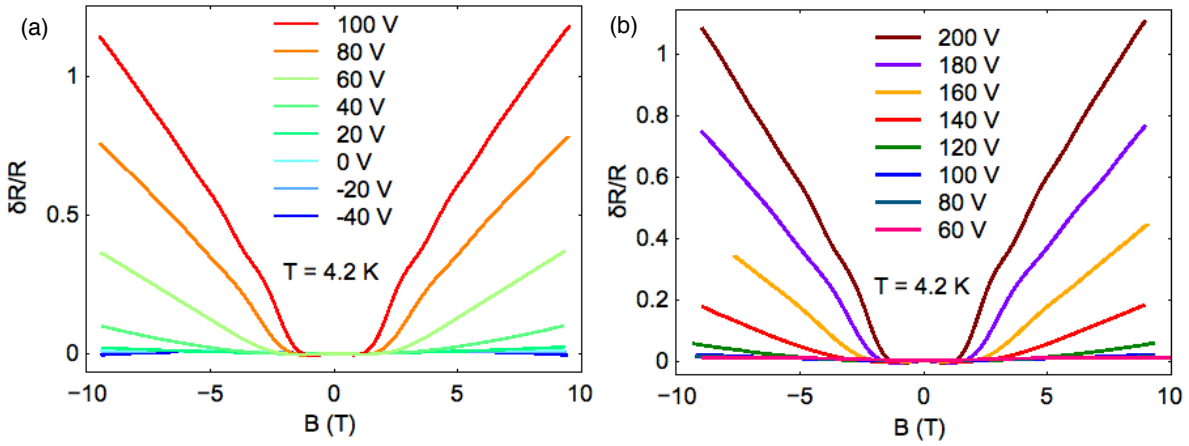

Figure 4.12. Differential MR for various values of V_g at $T = 4.2$ K **a,** for the Hall bar S1, and **b,** for the Hall bar S2.

Further evidence for multiband transport can be seen in the longitudinal MR data shown in Fig. 4.12(a), which was obtained simultaneously with the Hall data shown in Fig. 4.7(a). At 4.2 K for $V_g = 80$ and 100 V, the MR for the Hall bar S1 is large ($\sim$ 220 % for $V_g = 100$ V) and positive, and shows evidence of SdH oscillations. As discussed in Chapter 2, SdH oscillations start to become discernible when $\omega_c\tau = \mu B >$

1, and $\hbar\omega_c \geq k_B T$, i.e., when the Landau level spacings are not completely smeared out by temperature. Here $\omega_c = eB/m^*$, τ is the transport scattering time, and μ is the carrier mobility. The relatively large size of the positive MR, which is $\propto (\mu B)^2$, and the fact that SdH oscillations are seen starting at relatively low fields, indicates that the mobility of the carriers for large positive values of V_g is large. In particular, for $V_g = 100$ V, SdH oscillations appear to start at $B \sim 1.5$ T, implying that the carrier mobility is greater than ~ 6500 cm^2/V·s, an estimate which is not too far from the one obtained from the two-electron fits to the Hall data, as shown in Table 4.1. The high field MR does not appear to saturate up to ~ 10 T, but instead shows a quasilinear increase. As discussed in Chapter 2, a non-saturating MR can indicate the presence of open orbits, or the simultaneous presence of electron and hole like carriers, i.e., compensation, or a large spread in carrier mobilities, as discussed earlier. A strong SOI has also been indicated as a possible reason for the presence of a large, positive, non-saturating MR in certain topological materials.[**92**] In this sample, as in other STO-based 2DCGs, open orbits are not expected. Hence the non-saturating behavior can be caused either by some degree of compensation, as suggested by the Hall data, or the presence of sample inhomogeneities, which are characteristic of these complex oxide samples, and may give rise to a spread in carrier mobilities.[**90**] The sample also shows evidence of SOI, as we shall see in the next section, although it is unclear if the observed SOI is strong enough at the higher values of V_g to lead to the kind of effects seen, for example, in WTe_2.[**92**]

As V_g is reduced, carrier mobilities decrease rapidly. This can be inferred from the fact that a decrease in V_g causes a decrease in the magnitude of the MR, which is $\propto (\mu B)^2$, and the disappearance of SdH oscillations, which occur when $\mu B > 1$, as shown

in Fig. 4.12(a) for the Hall bar S1. Thus the rapid decrease in the magnitude of the MR of the Hall bar S1 below $V_g \sim 20$ V can be associated with the depletion of high mobility carriers from bands that were occupied at higher values of V_g, so that at lower values of V_g, transport is due to low mobility electrons which populate the lower energy bands, and holes. In view of our understanding of the band structure of (111) STO-based 2DCGs, in which the slight compressive strain determines that the a_{1g} band lies higher in energy than the e'_g doublet, these observations may indicate the depopulation of higher energy a_{1g} bands with the reduction of V_g below $\sim$ 20 V in the Hall bar S1, when the range of variation of V_g was between 100 V and -40 V.

Figure 4.12(b) shows the longitudinal MR data for the Hall bar S2, obtained at T = 4.2 K, simultaneously with the Hall data shown in Fig. 4.7(b), when the range of variation of V_g was between 200 V and -40 V. A rapid reduction in the magnitude of the positive high field MR is seen to occur below $V_g \sim 120$ V, the same value of V_g below which the Hall data are linear, and hole-like carriers start to dominate, as seen from Fig. 4.7(b) and 4.8(b). We can follow the same logic described in the previous paragraph to conclude that when V_g is varied between 200 V and -40 V, the high energy a_{1g} band is depopulated below $V_g \sim 120$ V, for the Hall bar S2. Note again that the R_s values of S1 at $V_g = 20$ V, and S2 at $V_g = 120$ V, in the two different sets of measurements described, are comparable, around 1-4 kΩ.

In principle, it is possible to simultaneously fit the longitudinal MR and the Hall data at a particular value of V_g within the two-band model discussed earlier, to obtain values of the carrier densities and mobilities at that value of V_g. One would use Eqns. 2.3 and 2.4, which are written as follows:

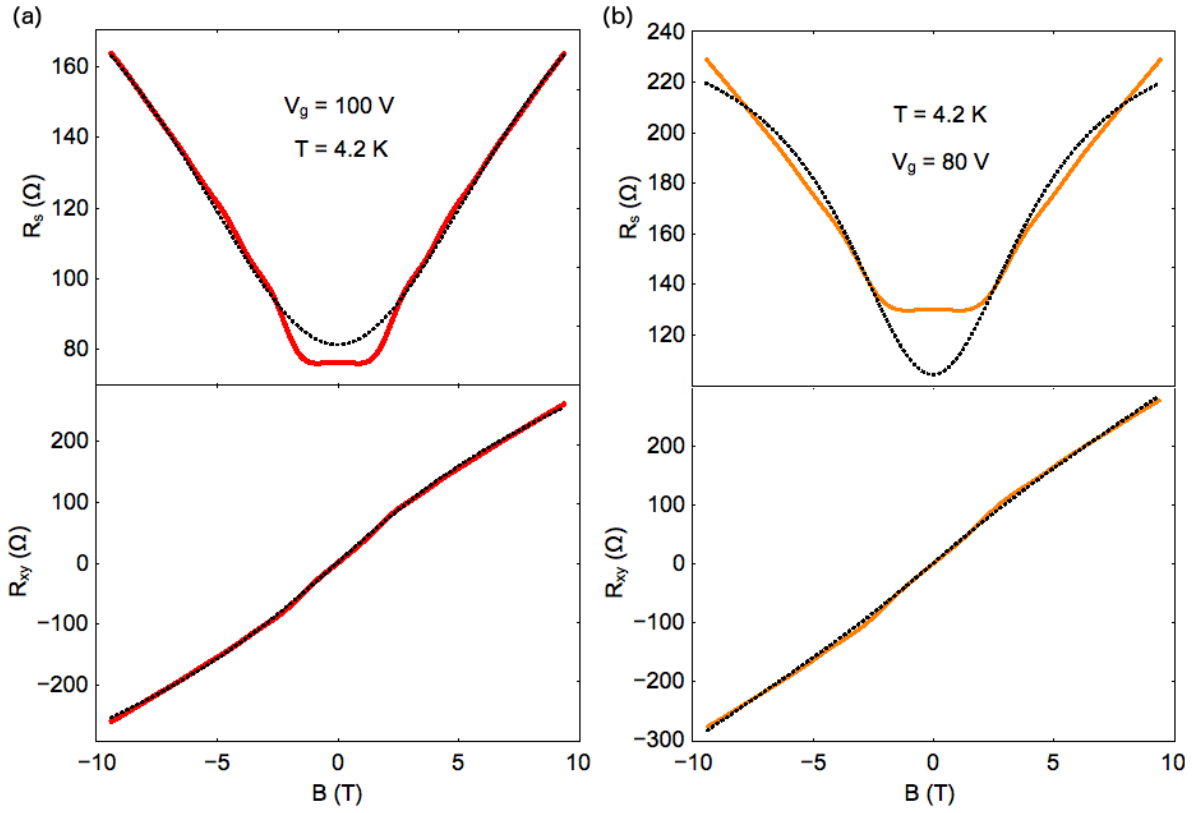

Figure 4.13. R_s and R_{xy} vs. B of the Hall bar S1 at **a,** $V_g = 100$ V and **b,** $V_g = 80$ V, at $T = 4.2$ K, fitted simultaneously to the two-band model described by equations 2.3 and 2.4.

$$R_H = \frac{R_1\rho_2^2 + R_2\rho_1^2 + R_1R_2(R_1+R_2)B^2}{(\rho_1+\rho_2)^2 + (R_1+R_2)^2B^2}$$

$$R_{cl}(B) = \frac{\rho_1\rho_2(\rho_1+\rho_2) + (\rho_1R_2^2 + \rho_2R_1^2)B^2}{(\rho_1+\rho_2)^2 + (R_1+R_2)^2B^2}$$

Here $R_{1,2} = -1/n_{1,2}e$ are the Hall coefficients, while $\rho_{1,2} = 1/n_{1,2}e\mu_{1,2}$ are the resistivities for carriers with densities n_1 and n_2 and mobilities μ_1 and μ_2. Figure 4.13(a) shows the result of such a fit for the Hall and the longitudinal MR data obtained at $T = 4.2$ K and

$V_g = 100$ V for the Hall bar S1, where a two-electron model is well-motivated, as discussed earlier. We obtain $n_1 = 1.88 \times 10^{13}$ /cm^2, $\mu_1 = 540$ cm^2/V·s, $n_2 = 1.28 \times 10^{13}$ /cm^2, and $\mu_2 = 5190$ cm^2/V·s. We see that the values obtained are different from those obtained by fitting the Hall data alone, as shown in Table 4.1. Although the obtained values seem plausible, and the Hall data as well as the high field MR data are fit reasonably well, the low field MR deviates substantially from the fit to this simple two-electron model, which indicates that there are other factors at play. We see also that for lower values of V_g, simultaneous fits to Hall and longitudinal MR data are very poor, as shown in Fig. 4.13(b) for $V_g = 80$ V for the Hall bar S1. Hence it is not possible to obtain reliable estimates of the carrier concentrations and mobilities in this manner.

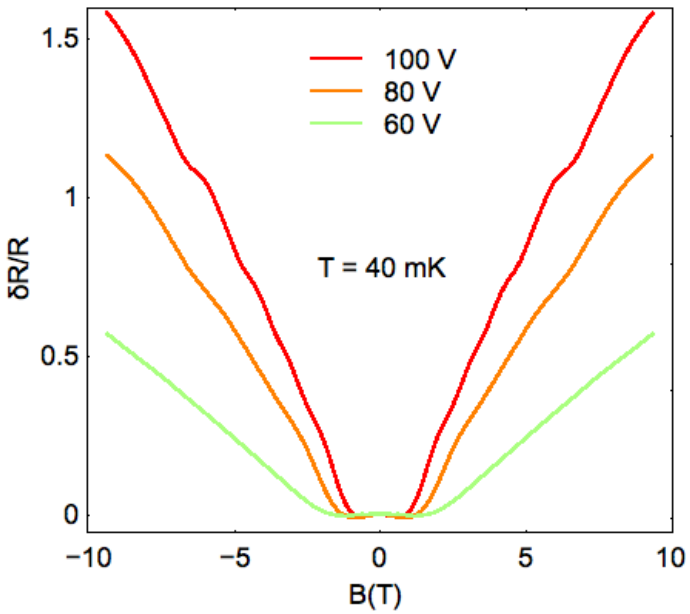

Figure 4.14. Differential MR for $V_g = 100$, 80, and 60 V, at $T = 40$ mK, for the Hall bar S1.

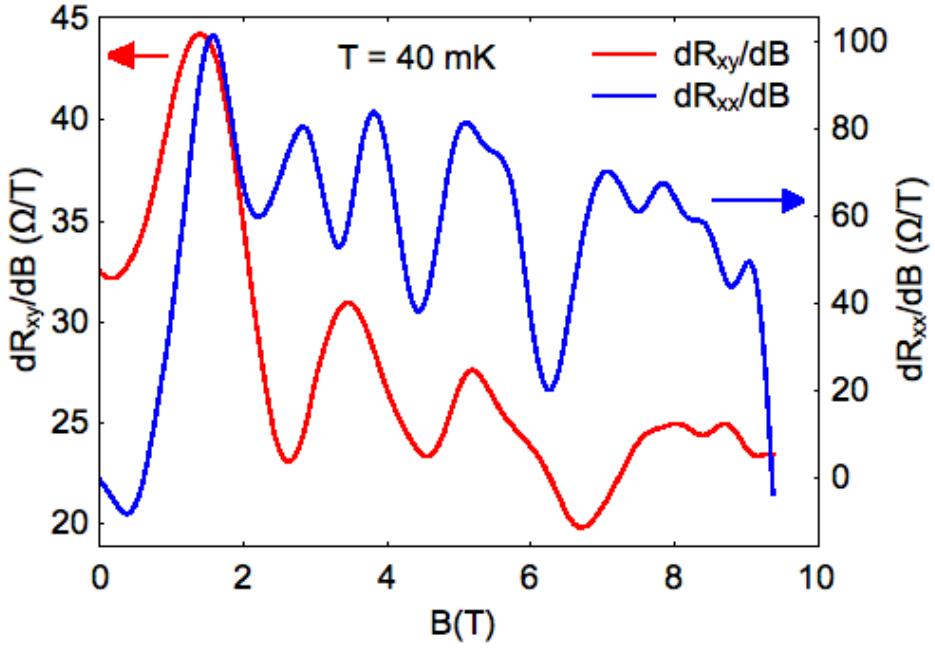

Figure 4.15. Derivatives of the MR and Hall resistance at $T = 40$ mK for $V_g = 100$ V for the Hall bar S1.

Figure 4.14 shows the MR data for the Hall bar S1 at $V_g = 100$, 80 and 60 V, at $T = 40$ mK. As expected, the size of the MR is larger at $T = 40$ mK as compared to the data at $T = 4.2$ K, and the SdH oscillations are also more prominent, particularly at $V_g = 100$ V and 80 V. Figure 4.15 shows the derivatives of the longitudinal MR and Hall data with respect to B, measured simultaneously, for the Hall bar S1 at $V_g = 100$ V and $T = 40$ mK. We can see that both derivatives show oscillatory behavior. A detailed analysis of the SdH oscillations according to the Lifshitz-Kosevich formula in Eqn. 2.5, and quoted here for clarity, would require measurements at multiple temperatures and over a higher

field range, which may yield a greater number of oscillations, and hence yield reliable estimates of parameters such as carrier effective mass m^* and the Dingle temperature T_D.

$$\Delta R_{SdH}(T,B) = 4R_0 \times \exp\Big(-\frac{2\pi^2 k_B m^* T_D}{\hbar e B}\Big)\frac{\frac{2\pi^2 k_B m^* T}{\hbar e B}}{\sinh(\frac{2\pi^2 k_B m^* T}{\hbar e B})}\sin\Big[2\pi\Big(\frac{F}{B}-\frac{1}{2}\Big)+\phi\Big]$$

However, one can still get some information about the number of high mobility carriers participating in transport by performing a Fourier analysis of the oscillations as a function of $1/B$. Figure 4.16(a) shows longitudinal MR data for the hall bar S1 at $T = 40$ mK for $V_g = 100$ V and 80 V, and $B > 1.5$ T, along with smooth fourth order polynomial backgrounds. The lowest order polynomials which reproduced the overall trend in the data well, without fitting the oscillations, were chosen as the backgrounds. After subtracting the backgrounds, nearly periodic oscillations as a function of $1/B$ are clearly discernible, as shown in Fig. 4.16(b). Fourier analysis of these oscillations for $V_g = 100$ V gives two prominent frequencies at which the spectral density peaks: a sharp peak around 15 T, and a small, broad peak around 40 T, indicated by arrows in Fig. 4.16(c). The oscillation frequency is given as $F = hn/N_s e$ according to the Onsager formula as discussed in Chapter 2, where n is the carrier density and N_s is the spin degeneracy, assumed here to be 2. This indicates that at $V_g = 100$ V there are two kinds of carriers, one with a density of the order of 10^{11} /cm^2, corresponding to the peak in the spectral density at ~ 15 T, and another with a density of the order of 10^{12} /cm^2, corresponding to the peak at ~ 40 T. According to the Lifshitz-Kosevich equation, the amplitude of SdH oscillations is larger for carriers with smaller effective masses and large scattering times τ. Hence a sharp, large peak in the spectral density indicates a larger mobility of the carriers giving rise to the

peak at that frequency. This tells us that the carriers with a higher concentration have a smaller mobility, whereas the carriers with a lower concentration have a higher mobility, in contrast to the results from the Hall fits discussed earlier. The carrier densities obtained

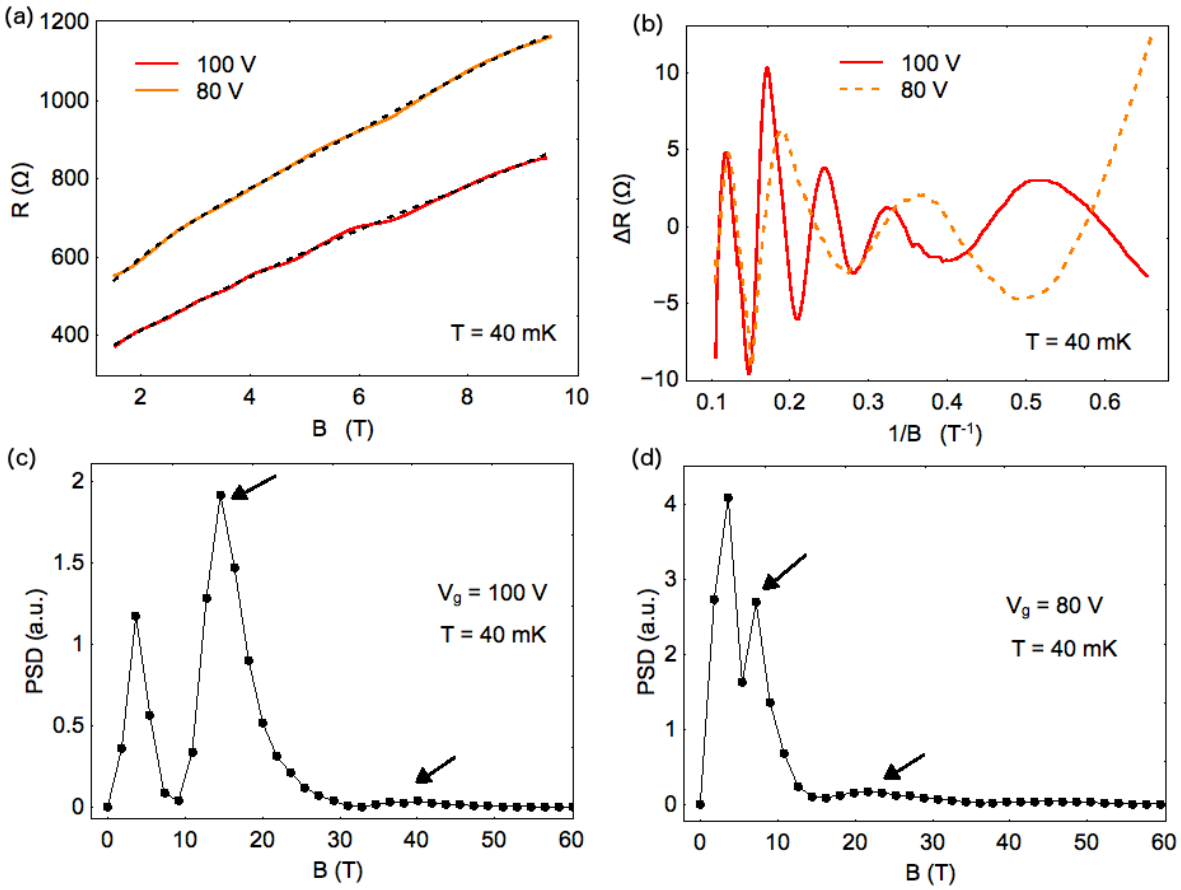

Figure 4.16. **a,** Solid lines are longitudinal MR data at $T = 40$ mK for $V_g = 100$ V and 80 V, above $B = 1.5$ T, for the Hall bar S1. The dotted lines are fourth order polynomial backgrounds. **b,** Amplitude of oscillations for data shown in Fig. 4.16(a), after subtracting the fourth order polynomial background. **c,** PSD for data at $V_g = 100$ V. Arrows show the position of peaks corresponding to two different carrier types. The peak at 5 T is associated with the remanent slowly varying background. **d,** PSD for data at $V_g = 80$ V, showing that the frequency peaks move to lower values of field.

from analysis of the SdH oscillations also yield carrier densities much smaller than those obtained from fits to the Hall data, as is commonly observed in STO based 2DCGs, and is discussed in Chapter 2. However, both types of carriers have high enough mobility (long scattering time and/or small mass) to show SdH oscillations at quite low fields.

At $V_g = 80$ V, the period of SdH oscillations increases, as seen from the dashed line in Fig. 4.16(b). We see from Fig. 4.16(d) that the two peaks in the power spectral density occur at lower frequencies, ~ 9 T and ~ 23 T, as compared to the power spectral density of the SdH oscillations at $V_g = 100$ V. This suggests that carrier density reduces and the Fermi surface becomes smaller as V_g is reduced.

Note that a peak in the power spectral density at ~ 5 T exists at both $V_g = 100$ V and 80 V. This is related to the very slowly changing background which exists in ΔR_{SdH} even after background subtraction, as is evident from the data shown in Fig. 4.16(b).

The data discussed in this section show us that as V_g is decreased, high mobility carriers are depleted, and lower mobility carriers occupying lower energy bands, along with holes, start to dominate transport. We will next look at what the longitudinal MR data at smaller B fields tells us about the evolution of SOI in the sample as the high mobility carriers are depleted.

4.3. Weak localization analysis at $T = 4.2$ K

We now focus on the low field regime of the MR measured on the Hall bars S1 and S2. Many experiments have demonstrated that the low field MR in STO-based 2DCGs, shows features characteristic of coherent back-scattering, i.e., weak localization /antilocalization

effects (WL/WAL). In most experiments so far on (001) LAO/STO, WAL behavior characterized by positive MR is seen to occur at high electron densities, i.e., at large positive values of V_g, whereas WL occurs at more negative values of V_g, indicating that SOI is stronger at more positive values of V_g, as discussed in Chapter 2.[**18, 88, 121**] We will now see that the trend is reversed in my (111) LSAT/STO sample.

Before I present my data on (111) LSAT/STO which shows evidence of WL/WAL behavior, I will briefly discuss the substantial difficulties in quantitatively analyzing low field MR data to get estimates of the relevant scattering times, namely, the phase coherence time τ_ϕ, the spin-orbit scattering time τ_{so}, and the magnetic scattering time τ_s.

The most commonly used theory for analyzing the low field MR is the one due to Hikami, *et al.*, which gives corrections to the MR of the form in Eqn. 2.7. This equation directly involves the transport scattering time τ, which as we discussed earlier, is very difficult to estimate accurately in STO-based 2DCGs. We have also discussed that a variety of B-dependent scattering processes can occur in STO-based 2DCGs, and can hence lead to a background MR which must be accounted for before analysis in terms of WL/WAL corrections. Typically, only the background contribution due to $\Delta R_{cl}(T, B)$ is considered in most analyses, although contributions due to EEI and magnetic scattering can be important in these systems. Also, the studies published so far exclude τ_s from their analyses completely. Many studies analyze the MR at only a single temperature for many values of V_g to first extract a trend for the characteristic fields B_ϕ and B_{so}, and from these find values of τ_{so} and τ_ϕ as a function of V_g. However, this can be problematic, given that it requires using values of the diffusion constant D, ($\tau_\alpha = \hbar/4eDB_\alpha$) which are difficult to estimate in these systems. Even if one restricts oneself to finding the characteristic fields

B_{so} and B_ϕ, or equivalently, characteristic lengths, l_{so} and l_ϕ ($l_\alpha^2 = \hbar/4eB_\alpha$), analysis at a single temperature may not give the correct estimates of these quantities. We can see this by using Eqns 2.9 and 2.10 which do not contain τ, instead of 2.7, and ignoring B_s, so that Eqn. 2.9 can be written as follows:

$$\frac{\delta R_{loc}}{R} = -\frac{3}{2} f[B, B_\phi + (4/3)B_{so}] + \frac{1}{2} f[B, B_\phi].$$

When B_{so} is negligible in comparison with B_ϕ, we can see from the above equation that $\delta R_{loc}/R$ is negative, and only dependent on B_ϕ. This situation corresponds to WL. In the opposite limit, when B_{so} is very large compared to B_ϕ, the first term in the above equation is much smaller than the second term. Here one observes that $\delta R_{loc}/R$ is positive, and the fits again depend only on B_ϕ and are insensitive to B_{so}. This situation corresponds to WAL. In the intermediate regime, when $B_{so} \sim B_\phi$, the MR is positive near zero field but becomes negative at higher field, and the fits depend on both B_ϕ and B_{so}. Hence one must fit the low field MR in a regime where B_ϕ and B_{so} are comparable, using both B_{so} and B_ϕ as fitting parameters, in order to obtain reliable estimates of the characteristic fields, and consequently of the characteristic length scales. Subsequently fitting the MR at other temperatures with only B_ϕ as a fitting parameter, keeping B_{so} constant to obtain B_ϕ as a function of T, can increase the confidence on the extracted fitting parameters.[**113**] This would work in most cases where SOI is not expected to depend on T. This is the procedure I employ. However, for my data it is possible to draw specific conclusions regarding the variation of SOI with V_g, even without performing numerical analysis, as we shall now discuss.

Figure 4.17(a) shows the MR at low fields for the Hall bar S1 described in the preceding section. We see that the MR is negative for $V_g > 20$ V, and positive below this value. We

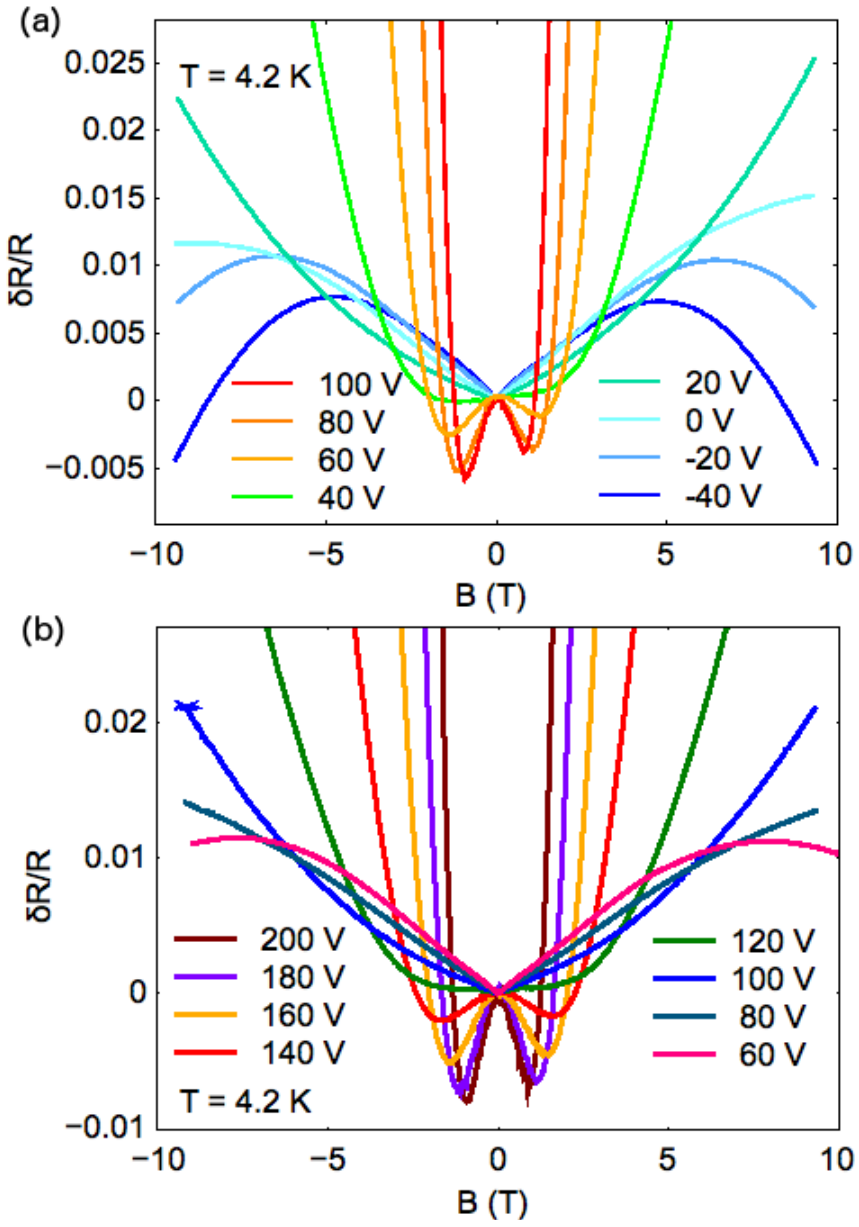

Figure 4.17. Differential MR at $T = 4.2$ K for various value of V_g **a,** for the Hall bar S1, and **b,** for the Hall bar S2.

first note that l_ϕ, which is proportional to R_s,[**123**] is expected to decrease in magnitude as R_s increases when V_g is decreased. Thus at $V_g \sim 100$ V, l_ϕ is comparatively large, or B_ϕ is small. However, the low field MR is negative, i.e., it exhibits weak localization. From our discussion above this indicates that B_{so} is smaller still, or l_{so} is even larger than l_ϕ. As V_g is reduced, l_ϕ decreases, which can be inferred from the increase in the characteristic field scale, as discussed in Section 2.4. As l_ϕ decreases, we also observe a transition to from WL to WAL, which indicates that l_{so} decreases even more rapidly than l_ϕ with V_g. The transition between negative to positive MR near zero field occurs for $V_g \leq 20$ V, the same value of V_g at which we see a decline in the magnitude of the large field MR (Fig. 4.12(a)). This is the also the same V_g below which $|R_H|$ increases with increasing V_g, and above which $|R_H|$ decreases with increasing V_g (Fig. 4.8(a)), and the same V_g which we associated earlier with the depopulation of an electron band.

This general trend of a decrease in the high field MR as V_g is reduced, a negative low field MR at high positive values of V_g, changing to a positive low field MR as V_g is decreased, concurrent with a change in the dependence of R_H with V_g, is reproduced irrespective of the range of V_g over which measurements are performed. Figure 4.17(b) shows data obtained at $T = 4.2$ K from the Hall bar S2. We see that for $V_g \geq 120$ V, the low field MR is negative, indicating weak localization, and for $V_g < 120$ V, the low field MR is positive, indicating weak antilocalization, and hence the development of a strong SOI. This is the same value of V_g which we associated earlier with the depopulation of the higher energy electron band for the Hall bar S2. This suggests that the increase in SOI is related to the depopulation of high mobility electron bands as a function of V_g, but that

the exact value of V_g at which this occurs depends on the overall range over which V_g is varied.

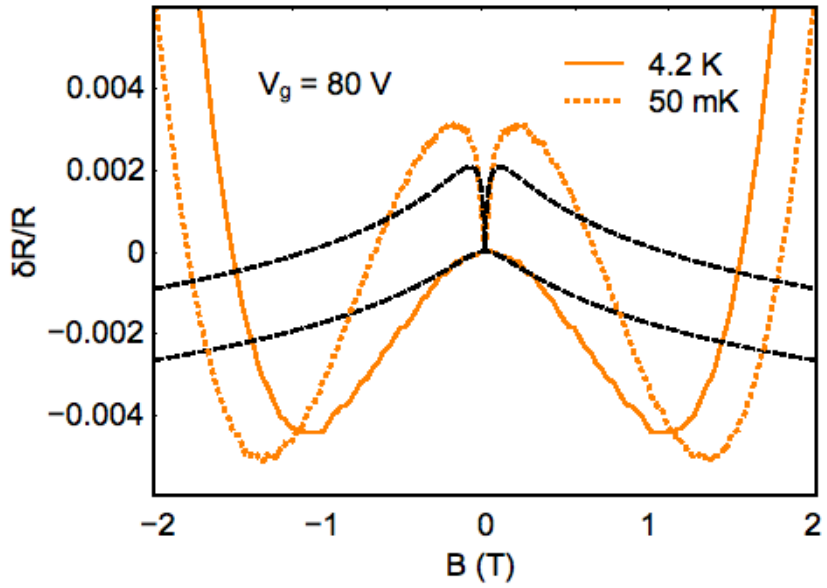

Figure 4.18. Differential MR at $V_g = 80$ V and $T = 4.2$ K (solid orange line) and $T = 50$ mK (dotted orange line), along with fits to Eqn. 2.9 (black dotted lines). Data were symmetrized to eliminate the effect of a small amount of drift.

Obtaining quantitative estimates for l_{so} and l_ϕ in our sample requires using the fitting procedure described earlier, wherein data obtained at several different temperatures must be analyzed together. It also necessitates taking into consideration contributions to the MR from other mechanisms, as described in Section 2.4. The importance of this can be seen from the following: Figure 4.18 shows fits using Eqn. 2.9 to the MR data at $T =$ 4.2 K and 50 mK for $V_g = 80$ V, for the Hall bar S1. If we choose l_ϕ to fit the curvature of the MR data at zero field, we find that the magnitude of the negative/ positive MR is impossible to fit. If we try to fit the amplitude of the positive/negative MR, one obtains a very poor fit near zero field.

In particular, for all values of V_g, there seems to be an excess negative MR, greater than what is allowed by the fits near zero field. This extra negative MR cannot be explained by the classical quadratic background alone since that gives a positive contribution. One factor which may give rise to negative MR is EEI, which can be important in a complex oxide heterostructure such as LSAT/STO. Negative MR, which depends quadratically on field, has been observed before in STO based carrier gases, and attributed to scattering of conduction electrons off localized magnetic moments, as discussed in Section 2.4. This may be a likely scenario in our sample as well, given that ferromagnetic order develops in the sample at lower temperatures, as we shall discuss later.

4.4. Weak localization analysis at sub-Kelvin temperatures

I will now focus on the quantitative analysis of the MR data obtained at sub-Kelvin temperatures on the Hall bar S1, in terms of WL/WAL contributions. As I will show later, for temperatures less than about 750 mK, the MR is hysteretic for $V_g \leq 40$ V, due to an emergent magnetic order in the system. In order to ensure that the hysteresis in the MR does not complicate the analysis of the data in terms of WL/WAL, I restricted the range of $V_g \geq 60$ V. By analyzing the MR data over a range of temperatures where weak localization effects are comparable to antilocalization effects, as evidenced by the presence of positive MR near zero field and negative MR at slightly larger fields, one can expect to arrive at reliable estimates of l_ϕ and l_{so}, as discussed earlier.

At millikelvin temperatures, the phonon contribution to the resistance, $\Delta R_{ph}(T)$, and the contribution due to scattering off ionic impurities, $\Delta R_{ion}(T)$, discussed in Section 2.4

freeze out, hence they can be ignored in our analysis. Contributions due to superconducting fluctuations, $\Delta R_{SC}(T,B)$, are also ignored since we do not see superconductivity in our sample (see Fig. 4.3), leaving us with the following equation for $R_s(T,B)$:

$$R_s(T,B) = R_0 + \Delta R_{cl}(T,B) + \Delta R_{mag}(T,B) + \Delta R_{EEI}(T,B) + \Delta R_{loc}(T,B) \tag{4.1}$$

Here R_0 is the Drude resistance, $\Delta R_{cl}(T,B)$ is the classical contribution, $\Delta R_{mag}(T,B)$ is the contribution due to scattering off magnetic moments, and $\Delta R_{EEI}(T,B)$ is the contribution due to EEI. For $V_g \geq 60$ V, we can approximate R_s as R_0, since for these values of V_g, the sample resistance changes by less than 5 % over the temperature range of interest. Hence we can write the differential MR as:

$$\frac{\delta R(T,B)}{R_s} = \frac{R(T,B) - R(T,B=0)}{R_s}, \tag{4.2}$$

This can be expressed as follows:

$$\frac{\delta R(T,B)}{R_s} = \frac{\delta R_{loc}(T,B)}{R_s} + \frac{\delta R_{BG}(T,B)}{R_s}, \tag{4.3}$$

where the first term is given by Eqn. 2.9 and the second term is a background contribution due to classical orbital effects, EEI, and magnetic scattering. I have determined that the background term can be written as follows:

$$\frac{\delta R_{BG}(T,B)}{R} = AB^2 - \frac{CB^2}{D + EB^2}. \tag{4.4}$$

The positive $\Delta R_{cl}(T,B)$ in our high mobility (111) LSAT/STO sample at large positive values of V_g can be substantial even at small field values where WL/WAL effects are seen, and hence must be included in the background. I found that $\Delta R_{cl}(T,B)$ is well described by a $(\mu B)^2$ dependence, in the range of B where WL/WAL effects are seen, and is hence accounted for by the first term of Eqn. 4.4.

$\Delta R_{EEI}(T,B)$ can also be substantial, especially at low temperatures in a correlated oxide system such as LSAT/STO. As discussed in Chapter 2, $\Delta R_{EEI}(T,B)$ can be difficult to isolate from measurements of perpendicular MR alone, and even from measurements of the MR in $B_{||}$, due to the presence of other contributions to the MR. Hence $\Delta R_{EEI}(T,B)$ must also be included in the background. The important terms in conductivity corrections due to EEI can be written as follows:

$$\Delta\sigma_{EEI}(T,B) = \frac{e^2}{\hbar}\frac{1}{4\pi^2}\Big(2-\frac{3F}{2}\Big)\ln\Big(\frac{k_BT\tau}{\hbar}\Big) - \frac{e^2}{\hbar}\frac{1}{4\pi^2}Fg_2\Big(\frac{g\mu_BB}{k_BT}\Big)$$

Here the first term is the exchange and singlet Hartree contribution of the particle-hole channel, and leads to a negative contribution to the resistivity given as:

$$\Delta R^{ex}_{EEI}(T,B) = \frac{-m^*}{4\pi^2\hbar n\tau}\Big(2-\frac{3F}{2}\Big)[1-(\omega_c\tau)^2]\ln\Big(\frac{k_BT\tau}{\hbar}\Big)$$

This contribution is also proportional to $(\omega_c\tau)^2$ or equivalently, to $(\mu B)^2$. It can be positive or negative, and can also be accounted for by the first term of Eqn. 4.4.

Both the classical orbital and the exchange terms which are accounted for by the first term of Eqn. 4.4 can be T-dependent due to changes in τ, and the exchange and the singlet

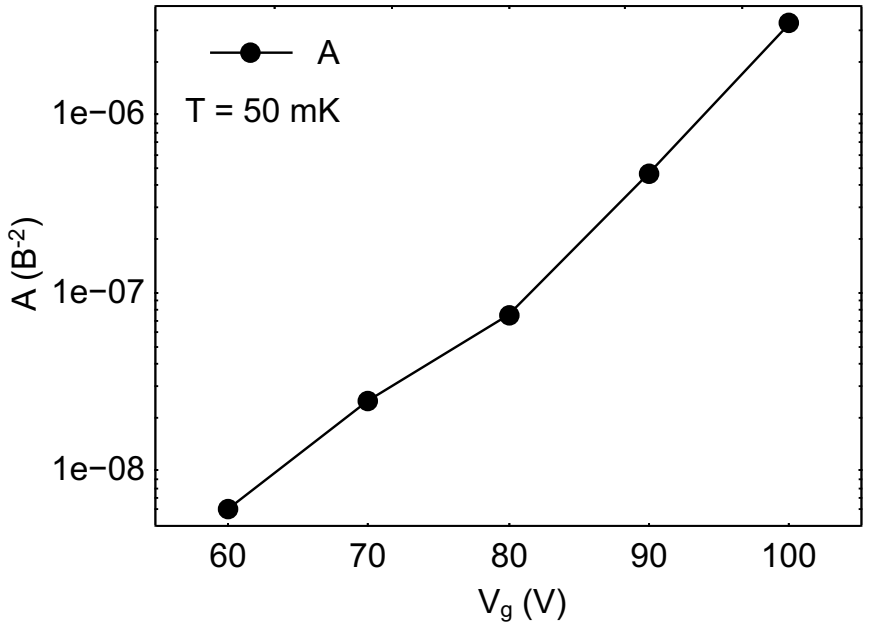

Figure 4.19. Variation of the parameter A with V_g at $T = 50$ mK.

Hartree contributions of EEI, vary logarithmically with T. However, I found experimentally that the background was well described by assuming a temperature independent parameter A. This leads us to conclude that the effective temperature dependence of τ and of this particular EEI contribution is likely to be small in this temperature range. I fixed the value of the coefficient A for all temperatures for a particular V_g. Also, for the same reason as above, we expect both contributions to be stronger for larger positive values of V_g for which carrier mobilities are larger. From Fig. 4.19, we see that the parameter A increases rapidly with V_g, which tells us that if the contribution due to ΔR^{ex}_{EEI} is negative, it is much smaller than the contribution due to ΔR_{cl}. We cannot make such a comparison if both these contributions are positive.

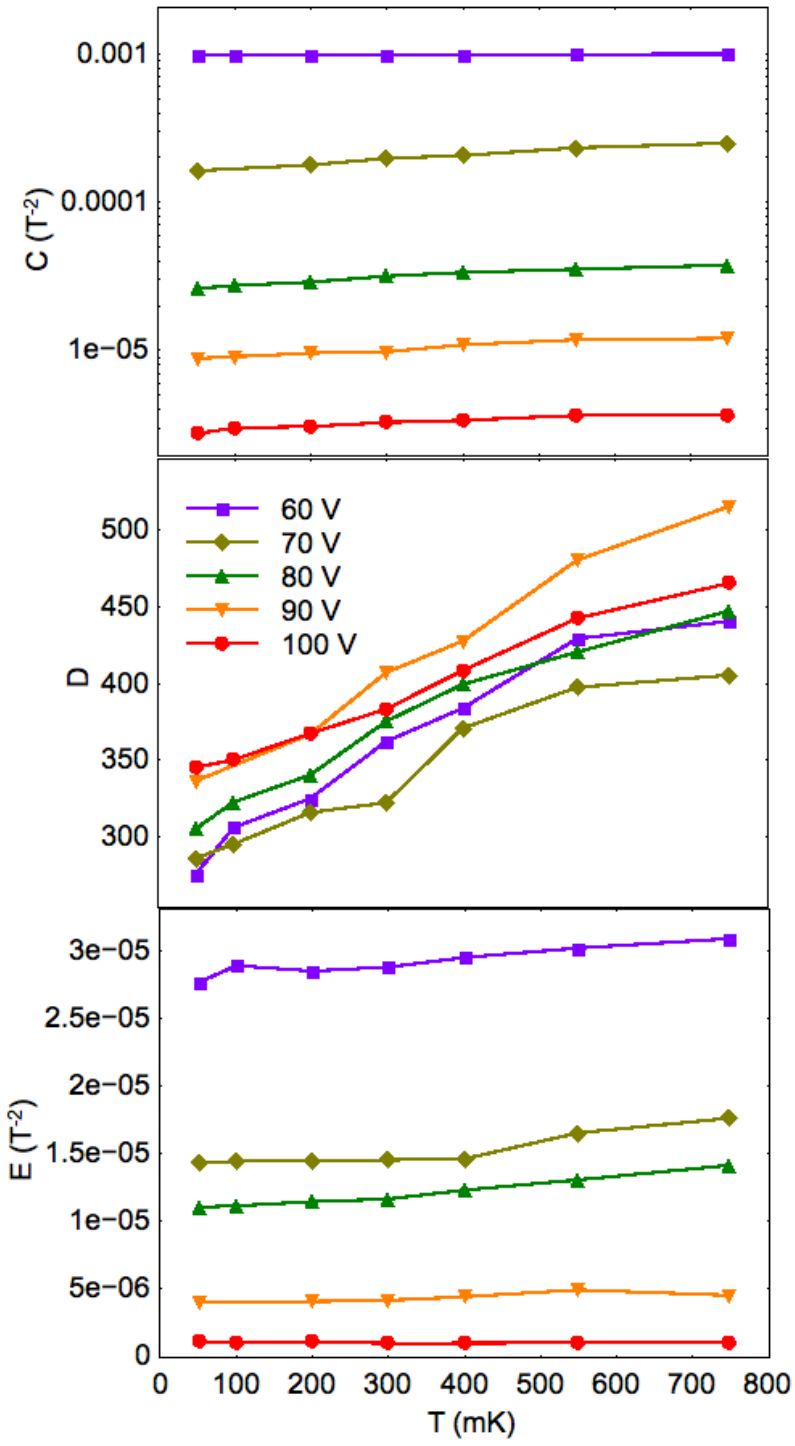

Figure 4.20. Variation of the parameters C, D, and E with T at different values of V_g, for the Hall bar S1.

The second term in the equation describing $\Delta\sigma_{EEI}$ is quadratic in B at small fields and logarithmic in B at higher fields greater than $k_BT/g\mu_B$. The contribution to ΔR_{EEI} due to this term can be positive or negative, and can be roughly approximated by the second term of Eqn. 4.4. The negative contribution to the background due to ΔR_{mag}, which is quadratic in B at smaller fields and saturates above fields required to saturate the magnetic moments, as discussed earlier in Chapter 2, is also accounted for by the second term of Eqn. 4.4. The coefficients C, D, and E were allowed to vary with T, since the contributions due to magnetic scattering and EEI can be dependent on temperature. Figure 4.20 shows the variation of these fit parameters with T and V_g, for the data obtained on Hall bar S1. Note that due to the form of the second term in Eqn. 4.4, the values of the parameters C, D, and E can vary by some multiplicative factor.

B_{so} was also held constant since it is expected to be independent of T, given that the factors contributing to SOI, namely, band structure effects and atomic SOI are expected to be constant in this temperature range. The only changes in B_{so} should be due to changes in V_g. Zeeman and magnetic scattering effects on weak localization were also ignored.

Figure 4.21 shows the MR data for the hall bar S1, at various values of T for $V_g = 60$ V, with fits to Eqn. 4.3, along with a background given by Eqn. 4.4. Similar fits were obtained for all values of V_g and T, by fixing the values of A and l_{so} for a particular value of V_g at $T = 50$ mK, and allowing B, C, and D to change for other values of T at that V_g. Figure 4.22 shows the variation of the $l_\phi^2 \sim \tau_\phi$ as a function of T, for various values of V_g. We see that τ_ϕ increases as T is decreased for all V_g, and the increase is the largest for $V_g = 100$ V for which the sheet resistance R_s is the smallest. This is expected since

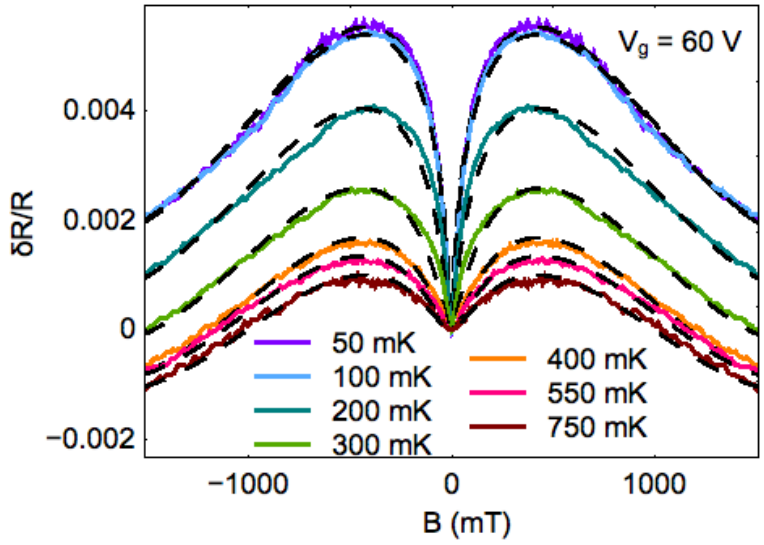

Figure 4.21. $\delta R/R$ vs B at $V_g = 60$ V and various T, for the Hall bar S1. The dashed lines are fits to Eqn. 4.3. with a background described by Eqn. 4.4. The data were symmetrized to remove the effect of a small drift in resistance with time.

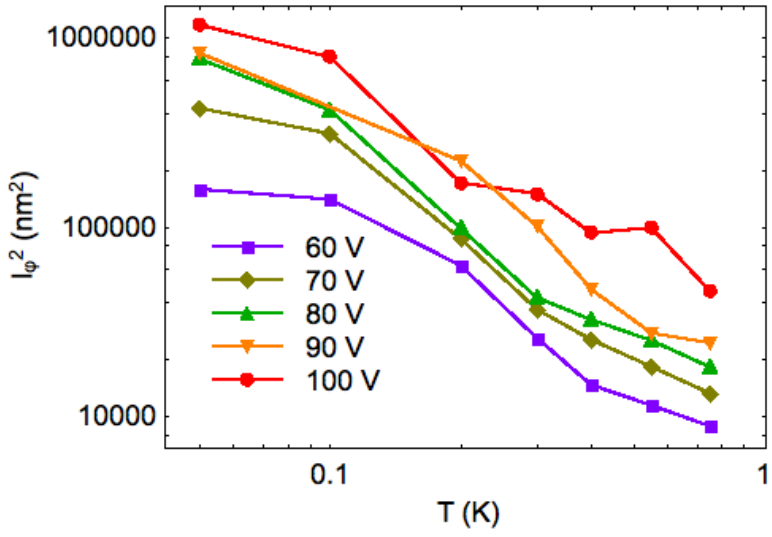

Figure 4.22. l_ϕ^2 ($\sim \tau_\phi$) as a function of T for various V_g for the Hall bar S1.

$l_\phi \propto 1/R_s$.[**151, 152**] $l_\phi^2 \sim \tau_\phi$ also seems to show a tendency to saturate at lower values of T, with the biggest effect for $V_g = 60$ V, which has the largest R_s.

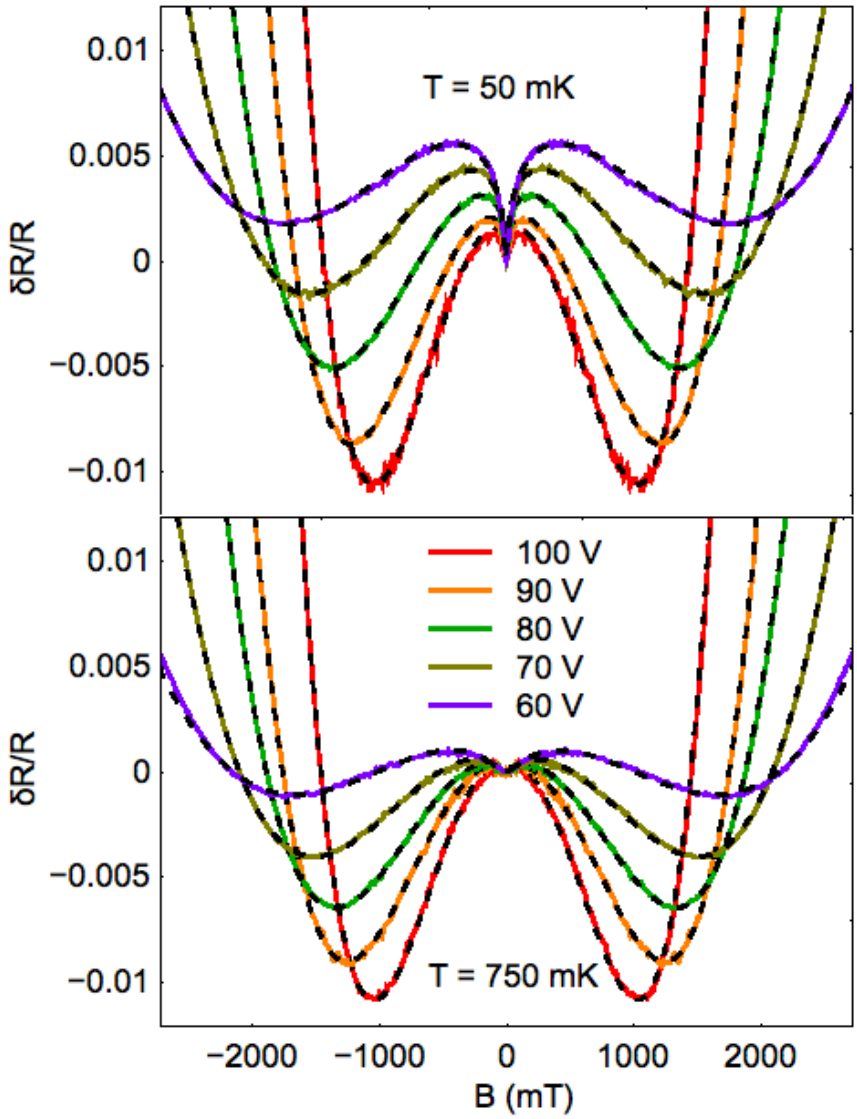

Figure 4.23. Symmetrized $\delta R/R$ vs. B at **a,** $T = 50$ mK and **b,** $T = 750$ mK, for various values of V_g for the Hall bar S1. The dashed line is a fit to Eqn. 4.3. with a background described by Eqn. 4.4.

Figure 4.23 shows the MR of the Hall bar S1 for various values of V_g, measured at T = 50 mK and 750 mK. From these I obtained estimates for l_{so} and l_ϕ at $T = 50$ mK for values of V_g, which are plotted in Fig. 4.24. We see that l_ϕ, on the left axis, decreases as a function of V_g. This is as expected from the variation in R_s with V_g, shown in the inset of Fig. 4.24. However, l_{so} clearly also decreases with V_g, indicating that SOI becomes stronger as V_g is reduced. This quantitatively demonstrates what we discussed qualitatively in the previous section.

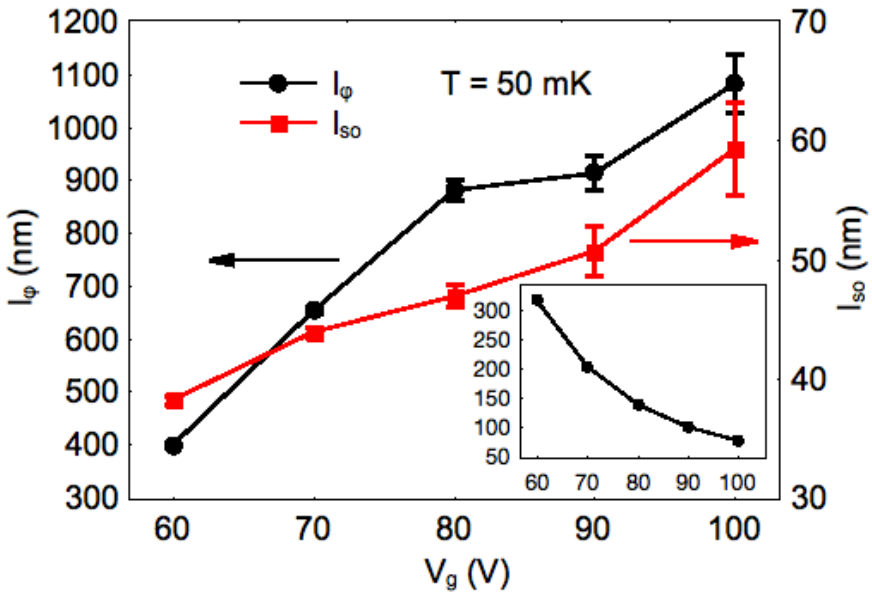

Figure 4.24. l_ϕ and l_{so} as a function of V_g for $T = 50$ mK, obtained from the data and fits shown in Fig. 4.23. Inset shows the variation of the R_s with V_g at $T = 50$ mK. The vertical axis in the inset is in Ohms.

At first glance, this variation in SOI may seem counter-intuitive if the SOI is Rashba type, with the Rashba Hamiltonian given as $H_R = \alpha(\hat{\mathbf{n}} \times \vec{\mathbf{k}}) \cdot \vec{\mathbf{S}}$. Here $\vec{\mathbf{S}}$ are the Pauli matrices, $\vec{\mathbf{k}}$ is the electron wave vector, and $\hat{\mathbf{n}}$ is the unit vector perpendicular to the 2DCG plane. The Rashba SOI coupling constant α is dependent on the magnitude of the

electric field seen by the carriers in the 2DCG, which in part increases with the magnitude of V_g. Hence one would expect SOI to increase with the magnitude of V_g.[**18**] However, as discussed in Chapter 2, α also depends on the shape of the interfacial potential well, and the energy splitting for carriers near the Fermi level is proportional to k_F, both of which also change with V_g. Band filling also depends on V_g. As per the discussion in the previous section, the high field MR data suggests that in this (111) LSAT/STO sample, as V_g is reduced, higher energy, higher mobility bands get depleted, and transport is begins to be dominated by lower mobility carriers.

One may explain the observed trend in SOI by noting the different effect of ASO on different bands that dominate transport at different values of V_g. DFT calculations have demonstrated that in the presence of the trigonal crystal field experienced by the Ti ions near the interface of (111) oriented STO-based systems, the three $3d$ t_{2g} orbitals split into an e'_g doublet and an a_{1g} singlet.[**23, 24**] The ordering of these orbitals is determined by strain, and for systems with a compressive strain such as LSAT/STO, the e'_g doublet is lower in energy. It is also known that the atomic SOI can lead to the mixing and splitting of degenerate orbitals.[**38**] This might explain the observed increase of SOI at lower values of V_g and carrier concentrations, when the low energy bands are preferentially filled. Although for $V_g \geq 60$ V, one may argue that the high field MR data show that the higher energy band is not fully depleted, note that the parameters obtained from the WL analysis above are averages over all types of carriers participating in transport.[**153**] Hence as the population of the higher energy bands becomes comparatively smaller, the lower energy bands which experience a high ASO can start to have a larger effect on the experimental values of SOI, thus explaining the trend of SOI for $V_g \geq 60$ V.

The magnitude of RSO also depends on ASO. The relative strength of ASO and RSO and their respective variations with V_g can be distinguished by the dependence of the spin-orbit scattering time τ_{so} on the transport scattering time τ.[**118, 154**] I did not extract τ_{so} and τ_ϕ since they depend on the diffusion constant D, which is difficult to estimate. However, a general trend of a decreasing τ_{so} with V_g can be discerned on the basis of my analysis, as can be seen from Fig. 4.22 and Fig. 4.24. Although τ is difficult to estimate exactly in the system, it is clear that it also decreases with V_g. Hence we conclude that $\tau_{so} \sim \tau$ in this system, which suggests that ASO effects dominate over RSO.[**118, 154**]

For the Hall bar S1, below $V_g \sim 60$ V, high mobility carriers continue to get depleted, hole carriers start to play a role in transport, and SOI continues to get stronger. At subkelvin temperatures, a striking change in the behavior of the MR occurs as we enter this regime of strong SOI.

4.5. Magnetic ordering

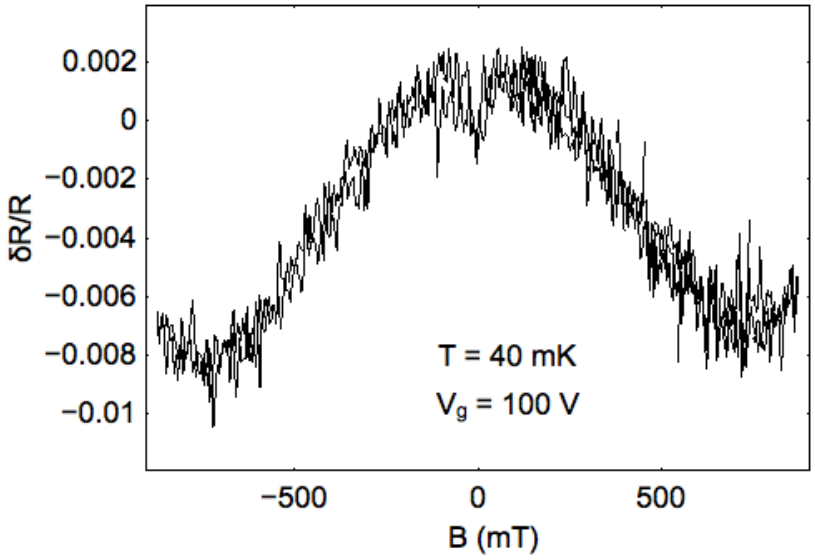

Figure 4.25. Differential MR for the Hall bar S1 at $T = 40$ mK and $V_g = 100$ V. Both forward and reverse traces are shown.

Figure 4.25 shows the fractional MR for the Hall bar S1 measured at $T = 40$ mK and $V_g = 100$ V. Both trace and retrace are plotted. A small dip in the MR near zero field is a consequence of weak antilocalization, which we discussed earlier. The important thing to notice is that within the limits of resolution, there is no hysteresis observed in the MR, similar to the data at $T = 4.2$ K for $V_g = 100$ V . Figure 4.26 shows the fractional MR at $T = 40$ mK for various values of V_g. For $V_g \geq 60$ V, the MR is non-hysteretic, similar to the data in Fig. 4.25; but for $V_g \leq 40$ V, the MR becomes progressively more hysteretic as V_g is decreased. We can distinguish two components to this hysteresis, both of which have been observed before in LAO/STO devices:[**11, 17, 147, 148**] a large background hysteresis, and two sharp mirror-symmetric dips at low fields.

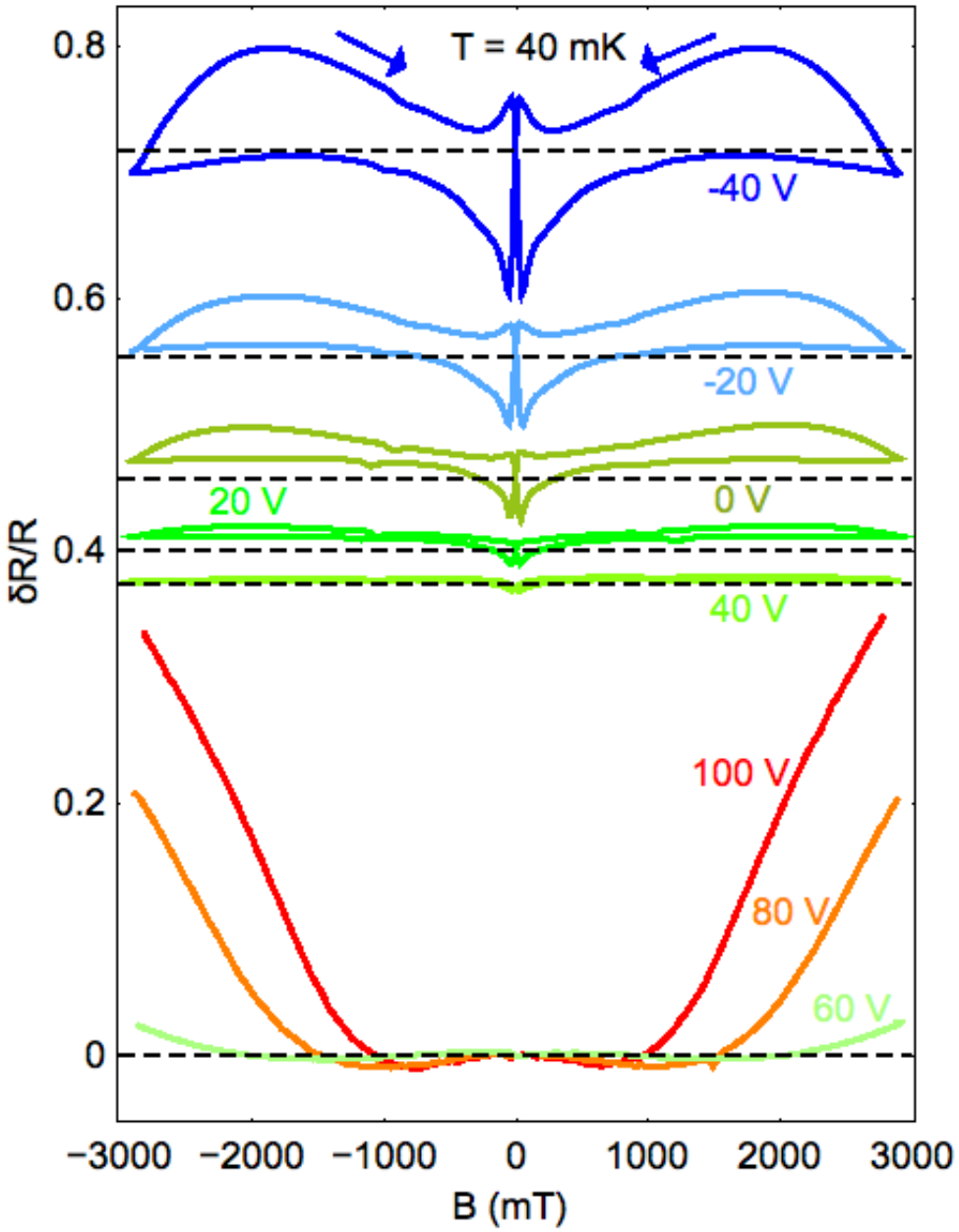

Figure 4.26. Differential MR for the Hall bar S1 at $T = 40$ mK for various values of V_g. For $V_g < 60$ V, the data are shifted along the vertical axis for clarity. The dashed black lines are an aid to the eye indicating the vertical shift of the origin for the various values of V_g.

By measuring resistance as a function of field perpendicular to the sample, B, while persisting a parallel magnetic field, $B_{||}$, at different values, one can see (Fig. 4.27) that the small field scale dips die out as the value of the persisted $B_{||}$ is increased. This is suggestive of ferromagnetic order in the system. It is known that hysteresis in the MR of a ferromagnetic material as a function of B can occur since the magnetization of the material is a hysteretic function of B. The dips disappear at large values of persisted $B_{||}$ because the larger values of $B_{||}$ suppress magnetization reversal and consequently, the hysteretic dips in the MR as a function of the perpendicular field B. The large field scale hysteresis is unaffected by the value of $B_{||}$ up to 600 mT, and hence it would appear that it

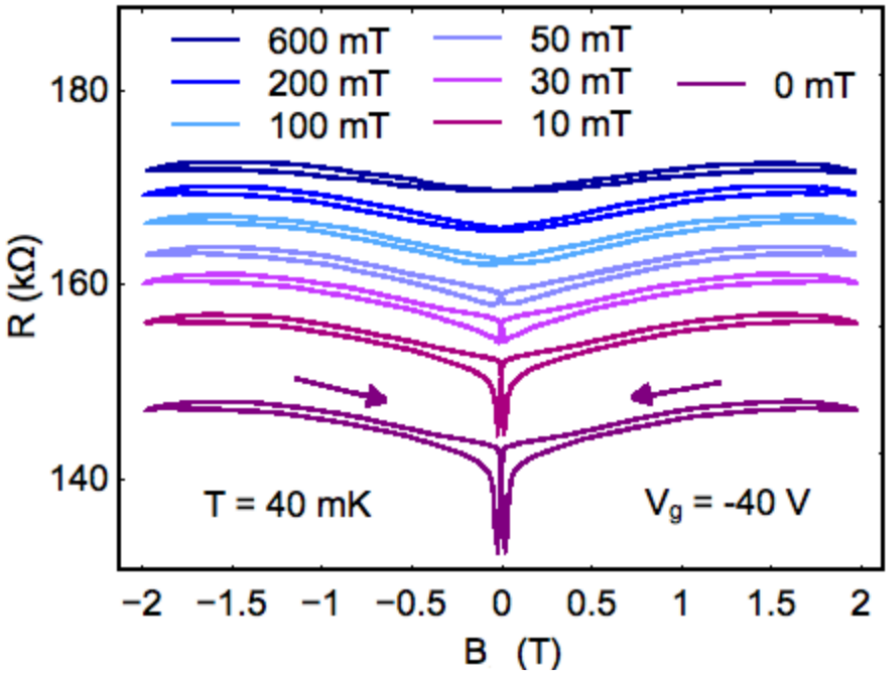

Figure 4.27. MR of the Hall bar S1 as a function of B swept at the rate of 1.2 mT/s, measured with various values of in-plane field $B_{||}$ held constant for V_g = -40 V, at T = 40 mK. The data have been offset vertically for clarity.

is unrelated to the magnetic order in the system. This large scale hysteresis has been seen in LAO/STO before[**11, 15**], and is associated with time dependent relaxation processes in glassy systems. As my LSAT/STO sample becomes more disordred and glassy with decreasing V_g, the increase in magnitude of the large field scale hysteresis in the MR at lower values of V_g is not surprising.

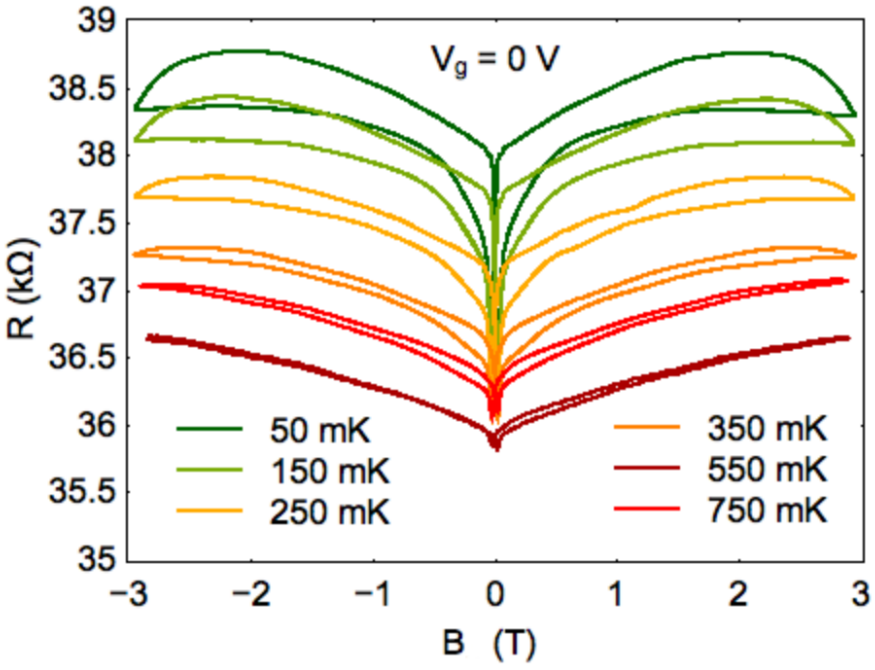

Figure 4.28. Resistance vs. B of the Hall bar S1, at $V_g = 0$ V, for various temperatures. The sweep rate of B is 1.2 mT/s.

Both hysteretic contributions decrease in magnitude with increasing temperature as seen for the Hall bar S1 in Fig. 4.28, for MR measured at different values of T for V_g = -40 V. Both hysteretic components almost disappear at $T \sim 750$ mK. The decrease in the large field scale hysteresis is expected as the glassy character of the system reduces with increasing temperature. It is not entirely clear that the ferromagnetism also disappears at $T \sim 750$ mK, since it might be that the hysteresis in the MR is below my measurement

resolution. One clue that this is not the case, and that the disappearance of the hysteresis is indeed related to the disappearance of the ferromagnetic order, comes from noting that the absolute value of R_s as well as the relative size of the MR over a given field range changes only by a small amount between $T = 50$ mK and $T = 750$ mK. This implies that there is negligible loss of measurement sensitivity within this temperature range, and hence if the hysteretic dips were as pronounced at 750 mK as they are at 50 mK, then they should have been detected with equal sensitivity. However, this is not the case, and we can reasonably claim that the hysteretic dips do in fact get much weaker at ~ 750 mK, indicating a weakening of the magnetic order in the 2DCG.

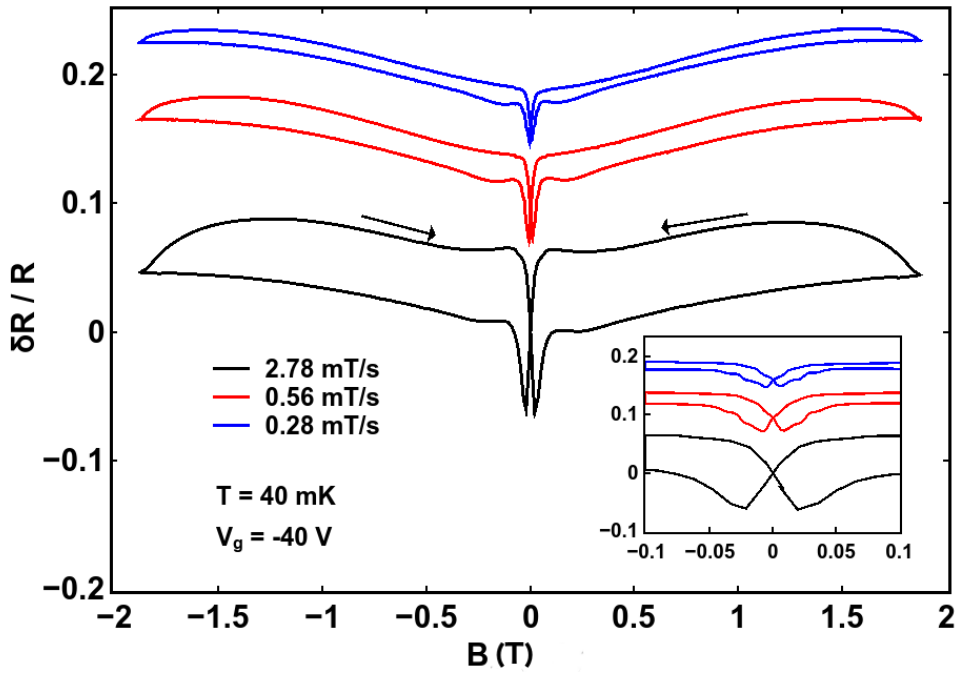

Figure 4.29. Differential resistance vs. B, at V_g = -40 V for $T = 40$ mK, measured at 3 different field sweep rates for the Hall bar S1. The data are offset vertically for clarity. Arrows show the direction of field sweep. The inset shows the data focusing on the low field hysteretic peaks.

As the field sweep rate changes, the hysteretic dips as well as the large scale "wings" change, as shown in Fig. 4.29. The sign, size, and field position of the dips would depend on the details of the details of the magnetization reversal process as well as on the nature of the material. In particular, the reduction in the size and field scale of the low field hysteretic dips can be explained by a temperature activated magnetization reversal process,[**149**] as well as a glassy nature of the magnetic material.[**150**] The size of the large field scale features also decreases with with decreasing sweep rate, which can also be explained by glassy behavior of the system.

The data discussed in this chapter show that in this system, low energy, low mobility carriers which experience a strong SOI, may participate in creating magnetic order in the system at reduced temperatures. It is known that the Hamiltonian for SOI is in general of the form $\mathbf{L} \cdot \mathbf{S}$, hence it does not break time reversal symmetry, and cannot lead to magnetism. Rashba and Dresselhaus SOI do create spin-polarized bands, but do not give a spin imbalance at the Fermi level. Although Stoner type magnetism has been predicted theoretically for STO-based 2DCGs, the origin of magnetism in (111) LSAT/STO is more likely to be local magnetic moments, given that local moments have been confirmed experimentally [**68**] as well as predicted theoretically [**54**] in STO-based 2DCGs. This means that the carriers from the low energy bands which experience a strong SOI mediate ferromagnetic exchange between the magnetic moments. Although SOI by itself cannot create magnetic order, it can modify the magnetic order in a system. As discussed earlier, although the strongest contribution to the SOI in my (111) LSAT/STO system appears to be of atomic SOI, the magnitude of the RSO depends on the atomic SOI, and hence RSO also likely becomes larger at larger negative values of

V_g. RSO is known to lead to magnetocrystalline anisotropy, and in (001) LAO/STO, has been suggested as the cause for the strong preference for in-plane orientation of the magnetization observed in experiments.[**13, 155**] Strong SOI can also lead to the canting of the spins of magnetic moments. This situation is ripe for the creation of spin textures, such as spiral arrangement of spins [**52**] and skyrmions,[**156**] in these system, through the Dzyaloshinskii-Moriya (DM) interaction. This scenario, in which the DM interaction gives rise to spiral orientation of moments in (001) LAO/STO, has been studied by Banerjee *et al.*,[**52**] who conjecture that inhomogenous magnetic patches in (001) LAO/STO seen in some experiments, [**14**] are caused when disorder breaks some of these spirals, causing local ferromagnetic order. A clear theoretical picture for magnetism in (111) system is yet to emerge, but will need to consider the strong SOI in this system.

CHAPTER 5

Conclusions and Future Directions

We have seen that STO-based 2DCGs display a remarkable variety of gate tunable, coexisting phenomena. Although substantial strides have been made in our understanding of the physical origins and mechanisms behind these phenomena, many challenges still remain. In particular, the mapping between tuning parameters such as strain, crystal orientation, oxygen vacancy concentration, etc., and sample properties, has not yet been unambiguously clarified. In the work described in this thesis, I have studied the electrical transport properties of (111) LSAT/STO, a heterostructure which has a different strain and crystal orientation as compared to the much more widely studied (001) LAO/STO heterostructure.

I found that the (111) LSAT/STO sample studied in this thesis, which was grown at 10^{-4} Torr oxygen partial pressure and not subjected to any post growth anneal treatment, was relatively clean and free of disorder. This was evidenced by its high RRR ratio, which was about 100, greater than the typical RRR of (111) LAO/STO [**26**] as well as (001) LAO/STO samples [**134**] grown in similar conditions, which is about 10 to 20. This can be attributed to the smaller strain in the LSAT/STO heterostructure, as compared to the LAO/STO heterostructures, similar to the observations on (001) LSAT/STO.[**29**]

On sweeping V_g to high positive values, however, I found that the initial low resistance state of $R_s \sim 100\,\Omega$ attained on cooling the sample down is lost, and an irreversible increase in sample resistance by about a factor of 70 at $T = 40$ mK, occurs. This "forming" of the

interfacial potential well hosting the 2DCG may be partly due to the loss of some charge carriers over the well into charge traps in the bulk of STO as suggested by Biscaras *et al.*.[**80**] However, the large magnitude of this irreversible increase is not commensurate with changes in carrier concentration alone, and indicates that a very large change in carrier mobilities also occurs during this process. It also appears that these changes start to become effective only as we start to sweep V_g back towards zero, as R_s changes only very little during the initial sweep from 0 V to some positive V_g, but begins to increase very rapidly during the reverse sweep back to lower values of V_g. How exactly this behavior occurs, what exactly causes the massive changes in carrier mobility on sweeping V_g, is not clear. In order to understand this better, it might be useful to perform detailed Hall and MR measurements, during the initial forward and reverse sweeps of V_g, looking for changes in WL/WAL effects at various stages of the gate sweep.

One of the startling observations on the (111) LAO/STO system was the anisotropic nature of transport along the in-plane mutually perpendicular crystal directions $[1\bar{1}0]$ and $[\bar{1}\bar{1}2]$. Anisotropies in transport properties were clearly observed by Davis *et al.* [**10, 21, 86**] in multiple (111) LAO/STO samples grown at an oxygen partial pressure of 10^{-3} Torr. Anisotropies were stronger at larger values of R_s, i.e., at more negative values of V_g and in oxygen post-annealed samples with fewer oxygen vacancies, and were attributed to a possible nematic phase which develops in the samples around 20 K. In my (111) LSAT/STO sample grown at 10^{-4} Torr and subjected to no post anneal treatment, I did not observe any anisotropies relating to crystal directions. Whether this is due to the lower strain in the LSAT/STO system as compared to the LAO/STO system, or whether anisotropic behavior will emerge in the (111) LSAT/STO sample when it is tuned

to higher R_s values, remains to be seen. By studying (111) LSAT/STO samples grown in the same conditions as (111) LAO/STO samples, we could get a clearer idea regarding the origins of the observed anisotropies in (111) LAO/STO. Tuning the system using post annealing treatments in oxidizing and reducing atmospheres, following Davis *et al.* [**21**], would further enhance our understanding.

I measured the Hall resistance and the MR of the (111) LSAT/STO sample in perpendicular fields up to 10 T. The Hall data showed nonlinear behavior for $V_g \geq 20$ V, and the longitudinal MR was large, about 220% for $V_g = 100$ V at $T = 4.2$ K, and positive. At $V_g = 100$ V and 80 V, the MR data showed indications of SdH oscillations , which became more prominent at millikelvin temperatures, and showed evidence of multiband transport. Below $V_g \sim 20$ V however, Hall data were linear within the field range measured, and the magnitude of the longitudinal MR dropped drastically. This indicates that high mobility carriers which play a prominent role in transport at more positive values of V_g, are depleted as V_g is lowered. In (111) STO-based 2DCGs under compressive strain, DFT studies have indicated that the conduction band manifold near the Γ point would have a low lying e'_g doublet and a higher energy a_{1g} band, although this is not seen with the available resolution in ARPES studies. Our results show that the splitting of bands may in fact exist, so that at lower values of V_g, carriers from the low lying e'_g bands, which also seem to have lower mobilities, dominate transport.

However, I also found that just as in the case of (111) LAO/STO,[**26, 86**] the variation of R_H with V_g cannot be explained by electron-like carriers alone, hence this picture remains incomplete unless we also consider contributions due to hole-like carriers at lower values of V_g. The origin of these hole-like carriers has not been clarified yet. Another

intriguing feature observed was the offset in R_{xy} at 0 field. This has been attributed to magnetic scattering as well as nematic ordering by different groups working on other material systems.[**145, 146**] A systematic study of the dependence of these offsets on the angle between the Hall bars and the in-plane crystal directions, especially in the regime where anisotropy in transport properties might emerge after oxygen-annealing the sample, can tell us more about the origin of the offsets.

Measurements at $T = 4.2$ K also showed that the low field MR was negative for higher positive values of $V_g \geq 20$ V, indicating WL behavior, and became positive for values of V_g smaller than ~ 20 V, indicating WAL behavior. Given the fact that R_s rapidly increases with decreasing V_g, we inferred that l_ϕ decreases with decreasing V_g. Hence the transition from WL to WAL behavior as V_g is decreased, led us to conclude that l_{so} decreases even more rapidly with V_g, indicating that SOI becomes very strong at lower values of V_g, where higher mobility carriers are depleted. This trend is opposite to what is typically observed in (001) LAO/STO. We can understand this by noting that in (111) LSAT/STO, as discussed before, the low energy bands are doubly degenerate, and hence more affected by ASO, whereas in (001) LAO/STO, the higher energy bands are doubly degenerate and more affected by ASO. RSO effects depend on a number of factors such as the strength of ASO, value of k_F, V_g, and the shape of the interfacial potential well. In my LSAT/STO sample, ASO certainly seems to be strong, hence we can expect a non-trivial Rashba contribution as well.

Making quantitative predictions of τ_ϕ and τ_{so} using low field MR analysis in my (111) LSAT/STO sample is complicated by the presence of a number of other scattering mechanisms which also give rise to T and B dependent contributions which can obfuscate the

WL/WAL analysis. In particular, I found that a ferromagnetic ordered state, characterized by a hysteretic MR, develops in the sample below $\sim$ 750 mK, at lower values of V_g where the high mobility carrier are depleted from the 2DCG. The ferromagnetism is likely to originate from the mediation of exchange between local moments, which are known to exist in STO-based 2DCGs, by itinerant charge carriers, and is hence dependent on free carrier density, or equivalently, on V_g. However, the local moments themselves would exist in the system independent of V_g, screened to various extents by the free carriers. Scattering of charge carriers off of the local moments can lead to a negative MR contribution. EEI effects which can also be substantial in STO-based 2DCGs can also give MR contributions at the field and temperature ranges under study.

Hence I analyzed the low field MR data at different sub-Kelvin temperatures, for $V_g \geq 60$ V, where no hysteresis in the MR is observed. I used the theory of Hikami *et al.*,[**120**] modified to remove the dependence on τ, along with a background to account for the substantial high field MR due to classical orbital contributions, and a negative contribution due to magnetic scattering. Any EEI effects can also be accounted for by the background. The analysis quantitatively confirmed the qualitative assessment that l_{so} and l_ϕ both become smaller as V_g is decreased, indicating that SOI becomes stronger as V_g is decreased. I did not extract τ_{so} and τ_ϕ since they also depend on the diffusion constant D, which is difficult to estimate. However, a general trend of a decreasing τ_{so} with V_g can be discerned on the basis of this analysis. Although τ is difficult to estimate exactly in the system, it is clear that it also decreases with V_g. Hence we conclude that $\tau_{so} \sim \tau$ in this system, which suggests that ASO effects dominate over RSO.[**118, 154**]

I did not find any superconductivity in my (111) LSAT/STO sample, and it would be interesting to try and induce superconductivity by annealing the sample in a reducing atmosphere, and see how the strong SOI in the system might affect superconducting properties.

A much more detailed understanding of the various contributions to the MR may be obtained by making measurements of the MR in parallel fields, as well as R_s vs. T measurements at different values of persisted magnetic fields. Although none of these measurements can be expected to give a clear and complete picture of the scattering processes involved, they would help in shedding some light on them.

The coexistence of a strong SOI in the system, along with magnetic order, can generate various spin-textures in the system called skyrmions, which are interesting from the theoretical point of view as well as for applications, and can be several nanometers in size.[**157**] If they exist in the (111) LSAT/STO system, they can be detected by a low temperature scanning probe microscope with a magnetic tip, such as the one that is under development in the Northwestern Mesoscopic Physics Group.

References

[1] M. Lorenz, *et al.*, The 2016 oxide electronic materials and oxide interfaces roadmap, *J. Phys. D:Appl. Phys.* **49**, 433001 (2016).

[2] H. Y. Hwang, Y. Iwasa, M. Kawasaki, B. Keimer, N. Nagaosa & Y. Tokura, Emergent phenomena at oxide interfaces, *Nat. Mater.* **11**, 103 (2012).

[3] K. Kalantar-zadeh, J. Z. Ou, T. Daeneke, A. Mitchell, T. Sasaki, & M. S. Fuhrer, Two dimensional and layered transition metal oxides, *Appl. Mater. Today* **5**, 73 (2016).

[4] A. Ohtomo & H. Y. Hwang, A high-mobility electron gas at the $LaAlO_3/SrTiO_3$ heterointerface, *Nature* **427**, 423 (2004).

[5] G. Herranz, F. Sánchez, N. Dix, M. Scigaj & J. Fontcuberta, High mobility conduction at (110) and (111) $LaAlO_3/SrTiO_3$ interfaces, *Sci. Rep.* **2**, 758 (2012).

[6] K. A. Müller & H. Burkard, $SrTiO_3$: An intrinsic quantum paraelectric below 4 K, *Phys. Rev. B* **19**, 3593 (1979).

[7] J. Hemberger, P. Lunkenheimer, R. Viana, R. Böhmer, & A. Loidl, Electric-field-dependent dielectric constant and nonlinear susceptibility in $SrTiO_3$, *Phys. Rev. B* **52**, 13159 (1995).

[8] S. Thiel, G. Hammerl, A. Schmehl, C. W. Schneider, & J. Mannhart, Tunable quasi-two-dimensional electron gases in oxide heterostructures, *Science* **313**, 1942-1945 (2006).

[9] N. Reyren, *et al.*, Superconducting interfaces between insulating oxides, *Science* **317**, 1196 (2007).

[10] S. K. Davis, *et al.*, Magnetoresistance in the superconducting state at the (111) $LaAlO_3/SrTiO_3$ interface, *Phys. Rev. B* **96** 134502 (2017).

[11] A. Brinkman, *et al.*, Magnetic effects at the interface between non-magnetic oxides, *Nat. Mater.* **6**, 493 (2007).

[12] F. Bi, M. Huang, S. Ryu, H. Lee, C. W. Bark, C. B. Eom, P. Irvin, and J. levy, Room temperature electronically controlled ferromagnetism at the $LaAlO_3/SrTiO_3$ interface, *Nat. Commun.* **5**, 5019 (2014).

[13] L. Li, C. Richter, J. Mannhart, and R. C. Ashoori, Coexistence of magnetic order and two-dimensional superconductivity at $LaAlO_3/SrTiO_3$ interfaces, *Nat. Phys.* **7**, 762 (2011).

[14] J. A. Bert, *et al.*, Direct imaging of the coexistence of ferromagnetism and superconductivity at the $LaAlO_3/SrTiO_3$ interface, *Nat. Phys.* **7**, 767 (2011).

[15] D. A. Dikin, M. Mehta, C. W. Bark, C. M. Folkman, C. B. Eom, and V. Chandrasekhar, Coexistence of superconductivity and ferromagnetism in two dimensions, *Phys. Rev. Lett* **107**, 056802 (2011).

[16] Ariando, X. Wang, G. Baskaran, Z. Q. Liu, J. Huijben, J. B. Yi, A. Annadi, A. Roy Barman, A. Rusydi, S. Dhar, Y. P. Feng, J. Ding, H. Hilgenkamp & T. Venkatesan, Electronic phase separation at the $LaAlO_3/SrTiO_3$ interface, *Nat. Commun.* **2** 188 (2011).

[17] M.M. Mehta, D.A. Dikin, C.W. Bark, S. Ryu, C.M. Folkman, C.B. Eom, and V. Chandrasekhar, Evidence for charge-vortex duality at the $LaAlO_3/SrTiO_3$ interface, *Nat. Commun.* **3**, 955 (2012).

[18] A. D. Caviglia, *et al.*, Tunable Rashba spin-orbit interaction at oxide interfaces. *Phys. Rev. Lett.* **105**, 236802 (2010).

[19] S. K. Davis, *et al.*, Signatures of Electronic Nematicity in (111) $LaAlO_3/SrTiO_3$ Interfaces, *Phys. Rev. B* **97**, 041408(R) (2018).

[20] Z. Q. Liu, C. J. Li, W. M. Lü, X. H. Huang, Z. Huang, S. W. Zeng, X. P. Qiu, L. S. Huang, A. Annadi, J. S. Chen, J. M. D. Coey, T. Venkatesan, and Ariando, *Phys. Rev. X* **3**, 021010 (2013).

[21] S. K. Davis, Z. Huang, K. Han, Ariando, T. Venkatesan, and Venkat Chandrasekhar, Electrical transport anisotropy controlled by oxygen vacancy concentration in (111) $LaAlO_3/SrTiO_3$ interface structures, *Adv. Mater. Interfaces* **4**, 1600830 (2017).

[22] C. W. Bark, *et al.*, Tailoring a two-dimensional electron gas at the $LaAlO_3/SrTiO_3$ (001) interface by epitaxial strain, *PNAS* **108**, 4720 (2011)

[23] D. Doennig, W. E. Pickett, and R. Pentcheva, Massive symmetry breaking in $LaAlO_3/SrTiO_3$ (111) quantum wells: A three orbital strongly correlated generalization of graphene, *Phys. Rev. Lett.* **111**, 126804 (2013).

[24] D. Xiao, W. Zhu, Y. Ran, N. Nagaosa, and S. Okamoto, Interface engineering of quantum Hall effects in digital transition metal oxide heterostructures, *Nat. Commun.* **2**, 596 (2011).

[25] T. C. Rödel, C. Bareille, F. Fortuna, C. Baumier, F. Bertran, P. Le Févre, M. Gabay, O. Hijano Cubelos, M. J. Rozenberg, T. Maroutian, P. Lecoeur, and A. F. Santander-Syro, Orientational tuning of the Fermi sea of confined electrons at the $SrTiO_3$ (110) and (111) surfaces, *Phys. Rev. Applied* **1**, 051002 (2014).

[26] P. K. Rout, I. Agireen, E. Maniv, M. Goldstein, and Y. Dagan, Six fold crystalline anisotropic magnetoresistance in the (111) $LaAlO_3/SrTiO_3$ oxide interface. *Phys. Rev. B* **95**, 241107(R) (2017).

[27] R. A. Cowley, Lattice Dynamics and Phase Transitions of Strontium Titanate, *Phys. Rev.* **134**, A981 (1964).

[28] C. Chakoumakos, D. G. Schlom, M. Urbanik, and J. Luine, Thermal expansion of $LaAlO_3$ and $(La,Sr)(Al,Ta)O_3$, substrate materials for superconducting thin-film device applications, *J. Appl. Phys.* **83**, 1979 (1998).

[29] Z. Huang, *et al.*, The effect of polar fluctuation and lattice mismatch on carrier mobility at oxide interfaces. *Nano Lett.* **16**, 2307 (2016).

[30] M. Mehta, PhD Thesis, Northwestern University (2015).

[31] S. K. Davis, PhD Thesis, Northwestern University (2017).

[32] A. H. Kahn and A. J. Leyendecker, Electronic Energy Bands in Strontium Titanate, *Phys. Rev.* **135**, A1321 (1964).

[33] Andrei V. Bandura, Robert A. Evarestov and Yuri F. Zhukovskii, Energetic stability and photocatalytic activity of $SrTiO_3$ nanowires: ab initio simulations, *RSC Adv.* **5**, 24115 (2015).

[34] A. Janotti, D. Steiauf, and C. G. Van de Walle, Strain effects on the electronic structure of $SrTiO_3$: Toward high electron mobilities, *Phys. Rev. B* **84**, 201304(R) (2011).

[35] L. F. Mattheiss, Energy Bands for $KNiF_3$, $SrTiO_3$, $KMoO_3$, and $KTaO_3$, *Phys. Rev. B* **6**, 4718 (1972).

[36] A.F. Santander-Syro, O. Copie, T. Kondo, F. Fortuna, S. Pailhes, R. Weht, X. G.Qiu, F. Bertran, A. Nicolaou, A. Taleb-Ibrahimi, P. Le Fevre, G. Herranz, M. Bibes, N. Reyren, Y. Apertet, P. Lecoeur, A. Barthelemy, and M. J. Rozenberg, Two-dimensional electron gas with universal subbands at the surface of $SrTiO_3$ *Nature (London)* **469**, 189 (2011).

[37] L. W. van Heeringen, A. McCollam, G. A. de Wijs, and A. Fasolino, Theoretical models of Rashba spin splitting in asymmetric SrTiO3-based heterostructures, *Phys. Rev. B* **95**, 155134 (2017).

[38] R. Winkler, Spin–Orbit Coupling Effects in Two-Dimensional Electron and Hole Systems, *Springer* (2003).

[39] O. Madelung, Introduction to Solid-State Theory, *Springer Series* (1978).

[40] A. Hachemi, H. Hachemi, A. Ferhat-Hamida and L. Louail, Elasticity of $SrTiO_3$ perovskite under high pressure in cubic, tetragonal and orthorhombic phases, *Phys. Scr.* **82**, 025602 (2010).

[41] M. Honig, J. A. Sulpizi, J. Drori, A. Joshua, E. Zeldov and S. Ilani, 'Local electrostatic imaging of striped domain order in $LaAlO_3/SrTiO_3$, *Nat. Mater.* **12**, 1112 (2013).

[42] P.I. Nabokin, D. Souptel, and A.M. Balbashov, Floating zone growth of high-quality $SrTiO_3$ single crystals, *Journ. of Cryst. Gr.* **250**, 397 (2003).

[43] Masashi Kawasaki, Kazuhiro Takahashi, Tatsuro Maeda, Ryuta Tsuchiya, Makoto Shinohara, Osamu Ishiyama, Takuzo Yonezawa, Mamoru Yoshimoto and Hideomi Koinuma, Atomic Control of the $SrTiO_3$ Crystal Surface, *Science* **2**, 66 (1994).

[44] J. G. Connell, B. J. Isaac, G. B. Ekanayake, D. R. Strachan, and S. S. A. Seo, Preparation of atomically flat $SrTiO_3$ surfaces using a deionized-water leaching and thermal annealing procedure, *Appl. Phys. Lett.* **101**, 251607 (2012).

[45] S. Ohta and T. Nomura, High-temperature carrier transport and thermoelectric properties of heavily La- or Nb-doped $SrTiO_3$ single crystals, *J. App. Phys.* **97**, 034106 (2005).

[46] H. P. R. Frederikse, W. R. Thurber, and W. R. Hosler, Electronic Transport in Strontium Titanate, *Phys. rev.* **134**, A442 (1964).

[47] J. F. Schooley, W. R. Hosler, E. Ambler, J. H. Becker, Marvin L. Cohen, and C. S. Koonce, Dependence of the Superconducting Transition Temperature on Carrier Concentration in Semiconducting $SrTiO_3$, *Phys. Rev. Lett.* **14**, 305 (1965).

[48] N. Bickel, G. Schmidt, K. Heinz, and K. Müller, Ferroelectric relaxation of the $SrTiO_3$ (100) surface, *Phys. Rev. Lett.* **62**, 2009 (1989).

[49] J. Mannhart, D.H.A. Blank, H.Y. Hwang, A.J. Millis, and J.-M. Triscone, Two dimensional electron gases at oxide interfaces, *MRS Bulletin* **33(11)**, 1027 (2008).

[50] F. Gunkel, Ph.D. Thesis, Forschungszentrum Jülich, (2013).

[51] N. Nakagawa, H. Y. Hwang, and D. A. Muller, Why some interfaces cannot be sharp, *Nat. Mater. 5*, 204 (2006).

[52] Sumilan Banerjee, Onur Erten and Mohit Randeria, Ferromagnetic exchange, spin-orbit coupling and spiral magnetism at the $LaAlO_3/SrTiO_3$ interface, *Nat. Phys.* **9**, 626 (2013).

[53] M. Reinle-Schmitt, *et al.*, Tunable conductivity threshold at polar oxide interfaces, *Nat. Commun.* **3**, 932 (2012).

[54] R. Pentcheva and W. E. Pickett, Charge localization or itineracy at $LaAlO_3/SrTiO_3$ interfaces: Hole polarons, oxygen vacancies, and mobile electrons, *Phys. Rev. B* **74**, 035112, (2006).

[55] D. W. Reagor and V. Y. Butko, Highly conductive nanolayers on strontium titanate producedby preferential ion-beam etching, *Nat. Mater.* **4**, 593 (2005).

[56] M. Shcultz and Lior Klein, Relaxation of transport properties in electron-doped $SrTiO_3$, *Appl. Phys. Lett.* **91**, 151104 (2007).

[57] H. Gross and s. Oh, Efficient resistive memory effect on $SrTiO_3$ by ionic-bombardment, *Appl. Phys. Lett.* **99**, 092105 (2011).

[58] S. McKeown Walker, *et al.*,, Control of a Two Dimensional Electron Gas on $SrTiO_3$ by Atomic Oxygen, *Phys. Rev. Lett.* **113**, 177601 (2014).

[59] G. Pacchioni, Oxygen Vacancy: The Invisible Agent on Oxide Surfaces, *ChemPhysChem* **4**, 1041 (2003).

[60] C. Mitra, C. Lin, J. Robertson, and Alexander A. Demkov, Electronic structure of oxygen vacancies in $SrTiO_3$ and $LaAlO_3$, *Phys. Rev. B* **86**, 155105 (2012).

[61] Z. Hou and K. Terakura, Defect States Induced by Oxygen Vacancies in Cubic $SrTiO_3$: First-Principles Calculations, *J. Phys. Soc. Jpn.* **79**, 114704 (2010).

[62] F. El-Mellouhi, *et al.*, Neutral defects in $SrTiO_3$ studied with screened hybrid density functional theory, *J. Phys.: Condens. Matter.* **25**, 135501 (2013).

[63] M. Sing, *et al.*, Influence of oxygen vacancies on two-dimensional electron systems at $SrTiO_3$-based interfaces and surfaces, *Eur. Phys. J. Special Topics* **226**, 2457 (2017).

[64] H. O. Jeschke, *et al.*, Localized versus itinerant states created by multiple oxygen vacancies in $SrTiO_3$, *New J. Phys.* **17**, 023034 (2015).

[65] J. Carrasco, F. Illas, N. Lopez, E. A. Kotomin, Yu. F. Zhukovskii, R. A. Evarestov, Yu. A. Mastrikov, S. Piskunov, and J. Maier, First-principles calculations of the atomic and electronic structure of F centers in the bulk and on the (001) surface of $SrTiO_3$, *Phys. Rev. B* **73**, 064106 (2006).

[66] Z. Q. Liu, *et al.*, Metal-Insulator Transition in $SrTiO_{3-x}$ Thin Films Induced by Frozen-Out Carriers, *Phys. Rev. Lett.* **107**, 146802 (2011).

[67] A. E. Paladino *et al.*., Oxygen ion diffusion in single crystal $SrTiO_3$, *J. Phys. Chem. Solids* **26**, 391 (1965).

[68] J.-S. Lee, Y.W. Xie, H. K. Sato, C. Bell, Y. Hikita, H. Y. Hwang and C.-C. Kao, Titanium d_{xy} ferromagnetism at the $LaAlO_3/SrTiO_3$ interface, *Nat. Mater.* **12**, 703 (2013).

[69] P.W. Lee, V.N. Singh, G.Y. Guo, H.-J. Liu, J.-C. Lin, Y.-H. Chu, C.H. Chen & M.-W. Chu, Hidden lattice instabilities as origin of the conductive interface between insulating $LaAlO_3$ and $SrTiO_3$, *Nat. Commun.* **7**, 12773 (2016).

[70] P. R. Wilmott, Structural Basis for the Conducting Interface between $LaAlO_3$ and $SrTiO_3$, *Phys. Rev. Lett.* **99**, 155502 (2007).

[71] Z. S. Popovic, S. Satpathy, and R. M. Martin, Origin of the Two-Dimensional Electron Gas Carrier Density at the $LaAlO_3$ on $SrTiO_3$ Interface, *Phys. Rev. Lett.* **101**, 256801 (2008).

[72] P. W. Anderson, Absence of diffusion in certain random lattices, *Phys. Rev. Lett.* **109**, 1492 (1958).

[73] Z. Zhong, A. Toth, K. Held, Theory of spin-orbit coupling at $LaAlO_3/SrTiO_3$ interfaces and $SrTiO_3$ surfaces, *Phys. Rev. B* **87**, 161102(R) (2013).

[74] Joshua, A., Pecker, S., Ruhman, J., Altman, E., and Ilani, S. A universal critical density underlying the physics of electrons at the $LaAlO_3/SrTiO_3$ interface. *Nat. Commun.* **3**, 1129 (2012).

[75] A. Joshua, J. Ruhman, S. Pecker, E. Altman, and S. Ilani, "Gate-tunable polarized phase of two-dimensional electrons at the $LaAlO_3/SrTiO_3$ interface," *PNAS* **110**, 9633 (2013).

[76] G. Khalsa, B. Lee, and A. H. MacDonald, Theory of t_{2g} electron-gas Rashba interactions, *Phys. Rev. B* **88**, 041302(R) (2013).

[77] S. M. Walker, *et al.*, Absence of giant spin splitting in the two-dimensional electron liquid at the surface of $SrTiO_3$ (001), *Phys. Rev. B* **93**, 245143 (2016).

[78] A. F. Santander-Syro, *et al.*, Giant spin splitting of the two dimensional electron gas at the surface of $SrTiO_3$, *Nat. Mater.* **13**, 1085 (2014)

[79] Boudjada, N., Wachtel, G., and Paramekanti, A., Magnetic and Nematic Orders of the Two-Dimensional Electron Gas at the Oxide (111) Surfaces and Interfaces, *Phys. Rev. Lett.* **120**, 086802 (2018).

[80] J. Biscaras, *et al.*, Limit of the electrostatic doping in two-dimensional electron gases of $LaXO_3$ $SrTiO_3$, *Sci. Rep.* **4**, 6788 (2014).

[81] Cheng G., Tomczyk M., Lu S., Veazey J., Huang M., Irvin P., Ryu S., Lee H., Eom CB., Hellberg CS., J. Levy, *et al.*, Electron pairing without superconductivity, *Nature* **521**, 196 (2015).

[82] H.-M. Christen, J. Mannhart, E. J. Williams, and Ch. Gerber, Dielectric properties of sputtered $SrTiO_3$ films, *Phys. Rev. B* **49**, 12095 (1994).

[83] P. Brinks, W. Siemons, J. E. Kleibeuker, G. Koster, G. Rijnders, & M. Huijben et al.., Anisotropic electrical transport properties of a two-dimensional electron gas at $SrTiO_3$-$LaAlO_3$ interfaces, *Appl. Phys. Lett.* **98**, 242904 (2011).

[84] Y. Frenkel, N. Haham, Y. Shperber, C. Bell, Y.Xie, Z. Chen, Y. Hikita, H. Y. Hwang, and B. Kalisky, *ACS Appl. Mater. Interfaces* **8**, 12514 (2016).

[85] Ma, *et al.*, Local Electrical Imaging of Tetragonal Domains and Field-Induced Ferroelectric Twin Walls in Conducting $SrTiO_3$, *Phys. Rev. Lett.* **116**, 257601 (2016).

[86] S. K. Davis, Z. Huang, K. Han, Ariando, T. Venkatesan, V. Chandrasekhar, "Anisotropic, multi-carrier transport at the (111) $LaAlO_3/SrTiO_3$ interface," *Phys. Rev. B* **95**, 035127 (2017).

[87] T. Schneider, A. D. Caviglia, S. Gariglio, N. Reyren, and J.-M. Triscone, 'Electrostatically-tuned superconductor-metal-insulator quantum transition at the $LaAlO_3/SrTiO_3$ interface, *Phys.Rev.B* **79**, 184502 (2009).

[88] S. Hurand, *et al.*, Field-effect control of superconductivity and Rashba spin-orbit coupling in top-gated $LaAlO_3/SrTiO_3$ devices, *Sci. Rep.* **5**, 12751 (2015).

[89] N.W. Ashcroft and N.D. Mermin, Solid State Physics, Fort Worth: Harcourt [1976].

[90] M. M. Parish and P. B. Littlewood, Non-saturating magnetoresistance in heavily disordered semiconductors. *Nature* **426**, 162 (2003).

[91] M. Ben Shalom, A. Ron, A. Palevski, and Y. Dagan, Shubnikov–De Haas Oscillations in $SrTiO_3/LaAlO_3$ Interface, *Phys. Rev. Lett.* **105**, 206401 (2010).

[92] J. Jiang, *et al.*, Signature of strong spin-orbital coupling in the large nonsaturating magnetoresistance material WTe_2, *Phys. Rev. Lett.* **115**, 166601 (2015).

[93] A. D. Caviglia, *et al.*, Two-Dimensional Quantum Oscillations of the Conductance at $LaAlO_3/SrTiO_3$ Interfaces, *Phys. Rev. Lett.* **105**, 236802 (2010).

[94] Lee, P. A. and Ramakrishnan, T. V., *Rev. Mod. Phys.* **57**, 287 (1985).

[95] P. Santhanam, PhD thesis, Yale University, 1985.

[96] A. Bergmann, M. Kaveh, and N. Wiser, Explanation of the anomalous T^4 behavior of the low-temperature electrical resistivity of silver, *J. Phys. F: Met. Phys.* **10**, (1980).

[97] D. Fuchs, A. Sleem, R. Schäfer, A. G. Zaitsev, M. Meffert, D. Gerthsen, R. Schneider, and H. v. Löhneysen, Incipient localization of charge carriers in the two-dimensional electron system in $LaAlO_3/SrTiO_3$ under hydrostatic pressure, *Phys. Rev. B* **92**, 155313 (2015).

[98] X. Lin, B. Fauqué, K. Behnia, Scalable T^2 resistivity in a small single-component Fermi surface, *Science*, **349**, 945 (2015).

[99] W. G. Baber, The contribution to the electrical resistance of metals from collisions between electrons, *Proc. R. Soc. Lond. A* **158**, 383 (1937).

[100] Barrett, J. H., Dielectric Constant in Perovskite Type Crystals *Phys. Rev.* **86**, 118 (1952).

[101] Menyoung Lee, J. R. Williams, Sipei Zhang, C. Daniel Frisbie, and D. Goldhaber-Gordon, Electrolyte Gate-Controlled Kondo Effect in $SrTiO_3$ *Phys. Rev. Lett.* **107**, 256601 (2011).

[102] I.M. Lifshitz, Anomalies of electron characteristics of a metal in the high pressure region, *Sov. Phys. JETP* **11**, 1130 (1960).

[103] D. Shoenberg, *Magnetic Oscillations in Metals, (Cambridge Monographs on Physics)* (1984).

[104] M. Yang, K. Han, O. Torresin, M. Pierre, S. Zeng, Z. Huang, T. Venkatesan, M. Goiran, J. M. D. Coey, Ariando, and W. Escoffier, High field magneto-transport in two-dimensional electron gas $LaAlO_3/SrTiO_3$, *Appl. Phys. Lett.* **109**, 122106 (2016)

[105] P. Petrovic, *et al.*, Emergent vortices at a ferromagnetic superconducting oxide interface. *New J. Phys.* **16**, 103012 (2014).

[106] M. Ben Shalom, C. W. Tai, Y. Lereah, M. Sachs, E. Levy, D. Rakhmilevitch, A. Palevski, Y. Dagan, 'Anisotropic magnetotransport at the $LaAlO_3/SrTiO_3$ interface,' *Phys. Rev. B* **80**, 140403 (2009).

[107] Fete, *et al.*, Rashba induced magnetoconductance oscillations in the $LaAlO_3$-$SrTiO_3$ heterostructure, *Phys. Rev. B* **86**, 201105(R) (2012).

[108] Y. Pai, A. Tyler, P. Irvin, and J. Levy, $LaAlO_3/SrTiO_3$: a tale of two magnetisms, *arXiv:1610.00789* (2016).

[109] N. Pavlenko, T. Kopp, E. Y. Tsymbal, G. A. Sawatzky, and J. Mannhart, Magnetic and superconducting phases at the $LaAlO_3/SrTiO_3$ interface: The role of interfacial Ti $3d$ electrons, *Phys. rev. B* **85**, 020407(R) (2012).

[110] A. K. Nigam and A. K. Majumdar, Magnetoresistance in canonical spin-glasses, *Phys. Rev. B* **27**, 495 (1983).

[111] Inaba, J., Katsufuji, T., Large Magnetoresistance in spin and carrier doped $SrTiO_3$, *Phys. Rev. B* **72**, 052408 (2005).

[112] J. Eom, PhD Thesis, Northwestern University (1998).

[113] G. Bergmann, Weak localization in thin films: A time-of-flight experiment with conduction electrons, *Phys. Rep.* **1**, 107 (1984).

[114] J. S. Langer and T. Neal, Breakdown of the concentration expansion for the impurity resistivity of metals, *Phys. Rev. Lett.* **16**, 984 (1966).

[115] Punnoose, A., Magnetoconductivity in the presence of Bychkov-Rashba spin-orbit interaction *Appl. Phys. Lett.* **88**, 252113 (2006).

[116] Kim, Y., Lutchyn, R. M., Nayak, B., Origin and transport signatures of spin-orbit interactions in one- and two-dimensional $SrTiO_3$-based heterostructures, *Phys. Rev. B* **87**, 245121 (2013).

[117] S. V. Iordanskii, Y. B. Lyanda-Geller, and G. E. Pikus, Weak localization in quantum wells with spin-orbit interactions, *JETP* **60**, 206 (1994).

[118] M. I. Dyakonov and V. I. Perel, Spin orientation of electrons associated with the interband absorption of light in semiconductors, *Sov. Phys. JETP* **33**, 1053 (1971).

[119] Maekawa, S. and Fukuyama, H., Magnetoresistance in two-dimensional disordered systems: Effects of Zeeman splitting and spin-orbit scattering, *J. Phys. Soc. Jpn.* **50**, 2516 (1981).

[120] Hikami, S., Larkin, A. Y., and Nagaoka, Y., Spin–orbit interaction and magnetoresistance in the two-dimensional random system, *Prog. Theor. Phys.* **63**, 707 (1980).

[121] Liang, *et al.*, Nonmonotonically tunable Rashba spin-orbit coupling by multiple-band filling control in $SrTiO_3$-based interfacial d-electron gases, *Phys. Rev. B* **92**, 075309 (2015).

[122] P.K. Rout, R. Maniv, and Y. Dagan, Link between the Superconducting Dome and Spin-Orbit Interaction in the (111) $LaAlO_3/SrTiO_3$ interface, *Phys. Rev. Lett.* **119**, 237002 (2017)

[123] Altshuler, B. L., Aronov, A. G., Larkin, A. I., and Khmelnitskii, D. E., Anomalous magnetoresistance of semiconductors, *Zh. Eksp. Teor. Fiz.* **81**, 768 (1981).

[124] Houghton, A., Senna, J. R., and S. C. Ying, Diffusion of electrons in two dimensions in arbitrarily strong magnetic fields, *Phys. Rev. B.* **25**, 2196 (1982).

[125] A. M. R. V. L. Monteiro, D. J. Groenendijk, I. Groen, J. de Bruijckere, R. Gaudenzi, H. S. J. van der Zant, and A. D. Caviglia, Two-dimensional superconductivity at the (111) $LaAlO_3/SrTiO_3$ interface, *Phys. Rev. B* **96**, 020504 (2017).

[126] V. F. Gantmakher and V. T. Dolgopolov, Superconductor-insulator quantum phase transition, *Physics-Uspekhi* **53**, 3 (2010).

[127] M. M. Mehta; D. A. Dikin; C. W. Bark; S. Ryu; C. M. Folkman; C. B. Eom; V. Chandrasekhar, Magnetic field tuned superconductor-to-insulator transition at the $LaAlO_3/SrTiO_3$ interface Journal *Phys. Rev. B* **90**, 10 (2014).

[128] E. Maniv, *et al.*, Strong correlations elucidate the electronic structure and phase diagram of $LaAlO_3/SrTiO_3$ interface, *Nat. Commun.* **6**, 8239 (2015).

[129] Michaeli, K., Potter, A. C., and Lee, P. A. *Phys. Rev. Lett.* **108**, 117003 (2012).

[130] L. G. Aslamazov & A. I. Larkin, The influence of fluctuation pairing of electrons on the conductivity of normal metal, *Phys. Lett. A* **26**, 238 (1968).

[131] K. Maki, Critical fluctuation of the order parameter in a superconductor. I, *Prog. Theor. Phys.* **39**, 897 (1968).

[132] W. J. Skocpol and M. Tinkham, Fluctuations near superconducting phase transitions, *Rep. Prog. Phys.* **38**, 1049 (1975).

[133] Han Electrical properties and subband occupancy at the $(La,Sr)(Al,Ta)O_3/SrTiO_3$ interface, *Phys. Rev. Mater.* **1**, 011601(R) (2017).

[134] Z. Huang, *et al.*, Controlling Kondo-like Scattering at the $SrTiO_3$-based Interfaces, *Sci. Rep.* **6**, 25455 (2016).

[135] H. M. Christen and G. Eres, Recent advances in pulsed-laser deposition of complex oxides, *J. Phys.: Condens. Matter* **20**, 264005 (2008).

[136] Fontcuberta, *et al.*, Tailored surfaces of perovskite oxide substrates for conducted growth of thin films, *Chemical Society Reviews* **43**, 2272 (2014)

[137] Ingrid Hallsteinsen, Magnus Nord, Torstein Bolstad, Per-Erik Vullum, Jos E. Boschker, Paulo Longo, Ryota Takahashi, Randi Holmestad, Mikk Lippmaa, and Thomas Tybell, Effect of Polar (111)-Oriented $SrTiO_3$ on Initial Perovskite Growth, *Cryst. Growth Des.* **16**, 2357 (2016).

[138] P.R. Puckett, S. L. Michel, and W. E. Hughes, Ion Beam Etching, *Thin Film Processes II, Academic Press Inc.* (1991).

[139] Kaufman and Robinson, *private communication.*

[140] Chen-jung Chien, Ph.D. Thesis, Northwestern University (1998).

[141] Jose Aumentado, Ph.D. Thesis, Northwestern University (2000).

[142] Zhigang Jiang, Ph.D. Thesis, Northwestern University (2005).

[143] Zhengfan Zhang, Ph.D. Thesis, Northwestern University (2006).

[144] Paul Cadden-Zimansky, Ph.D. Thesis, Northwestern University (2008).

[145] N. Nagaosa, J. Sinova, S. Onoda, A. H. MacDonald, and N. P. Ong, Anomalous Hall effect, *Rev. Mod. Phys.* **82**, 1539 (2010).

[146] J. Wu, A. T. Bollinger, X. He, and I. Bozović, Spontaneous breaking of rotational symmetry in copper oxide superconductors, *Nature* **547**, 432 (2017).

[147] A. Ron, E. Maniv, D. Graf, J.-H. Park, and Y. Dagan, Anomalous magnetic ground state in an $LaAlO_3/SrTiO_3$ interface probed by transport through nanowires, *Phys. Rev. Lett.* **113**, 216801 (2014).

[148] A. Kalaboukohv, *et al.*, Homogeneous superconductivity at the $LaAlO_3/SrTiO_3$ interface probed by nanoscale transport, *Phys. Rev. B* **96**, 184525 (2017).

[149] Sun, J. Z., Chen, L., Suzuki, Y., Parkin, S. S. P., and Koch, R. H., Thermally activated sweep-rate dependence of magnetic switching field in nanostructured current-perpendicular spin-valves. *Journ. Magn. Magn. Mater.* **247**, 237 (2002).

[150] S. Wolgast, *et al.*, Magnetotransport measurements of the surface states of samarium hexaboride using Corbino structures, *Phys. Rev. B* **92**, 115110 (2015).

[151] B. L. Altshuler and A. G. Aronov, *Sol. State. Comms.* **46**, 429, (1983).

[152] P. Abrahams, P. W. Anderson, P. A. Lee, and P. V. Ramakrishnan, *Phys. Rev. B* **24**, 6783 (1981).

[153] D. Rainer and G. Bergmann, Multiband effects in weak localization, *Phys. Rev. B* **32**, 3522 (1985).

[154] R. J. Elliot, Theory of the Effect of Spin-Orbit Coupling on Magnetic Resonance in Some Semiconductors, *Phys. Rev.* **96**, 266 (1954).

[155] M. H. Fischer, S. Raghu, and E. A. Kim, Spin–orbit coupling in $LaAlO_3/SrTiO_3$ interfaces: magnetism and orbital ordering, *New Journ. Phys,* **15**, 023022 (2013).

[156] A. Fert, N. Reyren, and V. Cros, Magnetic skyrmions: advances in physics and potential applications, *Nat. Rev. Mater.* **2**, 17031 (2017).

[157] W. Legrand *et al.*, Room temperature current-Induced generation and motion of sub-100 nm skyrmions, *Nano Lett.* **4**, 2703 (2017).